INVESTIGATION OF INTERFACIAL ORGANIZATION OF NANOSCOPIC SPECIES AT FLOWING LIQUID CRYSTAL-WATER INTERFACES

A THESIS SUBMITTED TO
THE GRADUATE SCHOOL OF NATURAL AND APPLIED SCIENCES
OF
MIDDLE EAST TECHNICAL UNIVERSITY

BY
CANSU DEDEOĞLU

IN PARTIAL FULFILLMENT OF THE REQUIREMENTS
FOR
THE DEGREE OF MASTER OF SCIENCE
IN
CHEMICAL ENGINEERING

SEPTEMBER 2025

Approval of the thesis:

INVESTIGATION OF INTERFACIAL ORGANIZATION OF NANOSCOPIC SPECIES AT FLOWING LIQUID CRYSTAL-WATER INTERFACES

Submitted by **Cansu Dedeoğlu** in partial fulfillment of the requirements for the degree of **Master of Science** i**n Chemical Engineering, Middle East Technical University** by,

Prof. Dr. Naci Emre Altun
Dean, **Graduate School of Natural and Applied Sciences** _____

Prof. Dr. Yusuf Uludağ
Head of the Department, **Chemical Engineering** _____

Assoc. Prof. Emre Büküşoglu
Supervisor, **Chemical Engineering, METU** _____

Examining Committee Members:

Prof. Dr. Yusuf Uludağ
Chemical Engineering, METU _____

Assoc. Prof. Emre Büküşoglu
Supervisor, Chemical Engineering, METU _____

Prof. Dr. Nihal Aydoğan
Chemical Engineering, Hacettepe University _____

Prof. Dr. Zeynep Çulfaz Emecen
Chemical Engineering, METU. _____

Prof. Dr. Göknur Bayram
Chemical Engineering, METU _____

Date: 01.09.2025

I hereby declare that all information in this document has been obtained and presented in accordance with academic rules and ethical conduct. I also declare that, as required by these rules and conduct, I have fully cited and referenced all material and results that are not original to this work.

Name Last name: Cansu Dedeoğlu

Signature:

ABSTRACT

INVESTIGATION OF INTERFACIAL ORGANIZATION OF NANOSCOPIC SPECIES AT FLOWING LIQUID CRYSTAL-WATER INTERFACES

Dedeoğlu, Cansu
Master of Science, Chemical Engineering
Supervisor: Assoc. Prof. Dr. Emre Büküşoğlu

September 2025, 103 pages

Cell membranes are composed primarily of phospholipid bilayers that are critical for maintaining cellular activities, and alterations contribute to diseases, such as Alzheimer's and neurodegenerative disorders. While previous studies have shown that phospholipids at static nematic liquid crystal (LC)-water interfaces induce interface-driven orientational transitions, precise quantification of vesicle fusion kinetics, influenced by the mechanical properties, remains limited. In this study, we introduce a novel microfluidic platform forming a flowing soft interface of nematic LC-aqueous phases, enabling continuous and rapid quantification due to the high responsiveness of LC interfaces. We investigated phospholipids with varying mechanical properties: 1,2-dilauroyl-sn-glycero-3-phosphocholine (DLPC, T_m= -2°C), 1,2-dioleoyl-sn-glycero-3-phosphocholine (DOPC, T_m= -17 °C), (liquid-like) 1,2-dipalmitoyl-sn-glycero-3-phosphocholine (DPPC, T_m= 41°C), sphingomyelin (Egg SM, T_m=38°C), (solid-like). Using fluorescence and polarized light microscopy, we found that lipid-rich domains accumulated at the end of the channel due to advection-dominated flow, determined by fusion kinetics. We revealed that DLPC and DOPC showed similar fusion kinetics, while Egg SM vesicles failed to fuse into the interface due to their rigid nature, unlike DPPC, which underwent shear-

induced fusion of vesicles to the interface. Moreover, we showed the effect of softening (via DTAB) and stiffening (via C16-ceramide) on vesicles. DTAB-lipid mixed micelles showed high coverage at the interface, including for rigid Egg SM. In contrast, C16-ceramide-doped DLPC vesicles did not fuse, indicating enhanced rigidity. Cholesterol exhibited lipid-specific effects: it increased the rigidity of DLPC and DOPC vesicles up to ~50 mol%, gradually stiffened DPPC, and softened Egg SM at 75% cholesterol, enabling shear-induced fusion of vesicles to the interface. These findings provide new insights into changing membrane mechanics with changing compositions of guest molecules and propose a platform for early diagnosis of membrane mechanics-associated diseases.

Keywords: Microfluidics, Liquid Crystals, Aqueous Interfaces, Lipid Vesicles, Adsorption

ÖZ

AKAN SIVI KRİSTAL-SU ARAYÜZLERİNDE NANOSKOPİK TÜRLERİN ARAYÜZ ORGANİZASYONUNUN ARAŞTIRILMASI

Dedeoğlu, Cansu
Yüksek Lisans, Kimya Mühendisliği
Tez Yöneticisi: Doç. Dr. Emre Büküşoğlu

Eylül 2025, 103 sayfa

Hücre zarları, hücresel aktivitelerin sürdürülmesi için kritik öneme sahip olan fosfolipit çift katmanlarından oluşur ve bu katmanlardaki değişiklikler Alzheimer ve nörodejeneratif bozukluklar gibi hastalıklara katkıda bulunur. Önceki çalışmalar, statik nematik sıvı kristal (LC)-su arayüzlerindeki fosfolipitlerin arayüz kaynaklı yönelimsel geçişlere neden olduğunu göstermiş olsa da mekanik özelliklerden etkilenen vezikül füzyon kinetiğinin hassas ölçümü sınırlı kalmaktadır. Bu çalışmada, LC arayüzlerinin yüksek duyarlılığı sayesinde sürekli ve hızlı ölçüm sağlayan, nematik LC-sulu faz arayüzü oluşturan yeni bir mikroakışkan platform sunuyoruz. Bu çalışmada değişen mekanik özelliklere sahip fosfolipitleri inceledik: 1,2-dilauroyl-sn-glisero-3-fosfokolin (DLPC, T_{erime}= -2°C), 1,2-dioleoil-sn-glisero-3-fosfokolin (DOPC, T_{erime}= -17 °C), (sıvı benzeri) 1,2-dipalmitoil-sn-glisero-3-fosfokolin (DPPC, T_{erime}= 41°C), sfingomyelin (Egg SM, T_{erime}= 38°C), (katı benzeri). Floresans ve polarize ışık mikroskopisi kullanarak, füzyon kinetiği sayesinde lipitlerin adveksiyon baskın akış nedeniyle kanalın sonunda biriktiğini bulduk. DLPC ve DOPC'nin benzer füzyon kinetiği gösterdiğini, Egg SM veziküllerinin ise DPPC'nin aksine, sert yapıları nedeniyle arayüze füzyonun gerçekleşmediğini ortaya koyduk; DPPC ise kayma kaynaklı füzyona uğramıştır.

Ayrıca, yumuşamanın (DTAB yoluyla) ve sertleşmenin (C16-seramid yoluyla) veziküller üzerindeki etkisini gösterdik. DTAB-lipit karışık miseller, sert Egg SM de dahil olmak üzere arayüzde yüksek füzyon gösterdi. Buna karşılık, C16-seramid katkılı DLPC vezikülleri arayüze füzyonu gerçekleştiremedi ve bu da artan sertliği gösterdi. Ayrıca, kolesterolün lipide özgü etkiler gösterdiğini bulduk: kolesterol DLPC ve DOPC veziküllerinin sertliğini ~%50 mole kadar artırdı, DPPC'yi kademeli olarak sertleştirdi ve Egg SM'yi %75 kolesterolde yumuşatarak kayma kaynaklı füzyona olanak sağladı. Bu bulgular, konuk moleküllerin değişen kompozisyonlarıyla değişen zar mekaniğine dair yeni bakış açıları sağlıyor ve zar mekaniğiyle ilişkili hastalıkların erken teşhisi için bir platform öneriyor.

Anahtar Kelimeler: Mikroakışkanlar, Sıvı Kristaller, Sulu Arayüzler, Lipid Veziküller, Adsorpsiyon

To my loved ones

ACKNOWLEDGMENTS

Firstly, I would like to sincerely thank my advisor, Assoc. Prof. Emre Büküşoğlu for the opportunities he provided. His insightful guidance, patience, and dedication have greatly influenced the scientific quality of this study as well as my development as a researcher. It has been an honor to study under his supervision.

I am deeply grateful to my mother, Hülya Dedeoğlu, for her influence on my hard-working personality and my father, Levent Dedeoğlu, for his unconditional support. Their encouragement, endless patience, and support have been my greatest source of strength and motivation. I also want to express my heartfelt gratitude to Görkem for believing in me even the times that I doubted myself. He always encouraged me to keep going and never let me give up. He shared both my happiness and my sadness, making my burdens his own and always looking for solutions. His support has been an invaluable driving force. I would also like to thank my cat, Duman Serpilcan, whose heart-melting charm and tiny presence brought joy and comfort during my graduate years.

I am truly thankful to my friends Useyma, Aleyna, Mert, and Uğur, who have always brought joy to my life. They provided a welcome escape during my stressful times and offered their support whenever I needed it. They became like a family to me in Ankara. I am grateful to my friends, Nermin, Buket, Ecem, Selcan, and Selime, who, despite being miles away, have always felt their presence and never withheld their support since our childhood years.

Last but not least, I would like to express my appreciation to the members of the Soft and Functional Materials Laboratory. I thank Deniz, Cansu, and İrem for their companionship. I also express my gratitude to Nurcan and Gülce for their continuous support and for sharing their knowledge. It was a great chance to meet and work with them. I thank Pouriya, Akrema, and Yiğit for their contributions.

Finally, I thank to Aslı Karausta, Özge Batır and Ali Akman. Although I did not have much time with them, their support for me and this study is valuable.

This work was funded by the European Union (ERC, LCFlow, 101039294).

TABLE OF CONTENTS

LIST OF TABLES

TABLES

LIST OF FIGURES

FIGURES

LIST OF ABBREVIATIONS

5CB	4-Cyano-4'-pentylbiphenyl
BODIPY-DHPE	N-(4,4-Difluoro-5,7-Dimethyl-4-Bora-3a,4a-Diaza-s Indacene-3-Propionyl)-1,2-Dihexadecanoyl-sn-Glycero-3-Phosphoethanolamine, Triethylammonium Salt
BOE	Buffered Oxide Etchant
C-16 Ceramide	N-palmitoyl-D-erythro-sphingosine
DLPC	1,2-dilauroyl-sn-glycero-3-phosphocholine
DLS	Dynamic Light Scattering
DMOAP	Dimethyloctadecyl[3-(trimethoxysilyl) propyl] ammonium chloride
DMPC	1,2-dimyristoyl-sn-glycero-3-phosphocholine
DOPC	1,2-dioleoyl-sn-glycero-3-phosphocholine
DPPC	1,2-dipalmitoyl-sn-glycero-3-phosphocholin
DTAB	Dodecyltrimethylammonium bromide
Egg SM	Sphingomyelin
ER	Relative Young's Modulus
EV	Extracellular Vesicles
FCPM	Fluorescence Confocal Polarized Microscopy
GSIS	Glucose-stimulated insulin secretion
LC	Liquid Crystal

O1	Alkyl-triazole oligomers
OTS	2-propanol, trichloro(octadecyl)silane
PBS	Phosphate Buffered Saline
PDMS	Polydimethylsiloxane
POPC	1-palmitoyl-2-oleoyl-sn-glycero-3-phosphocholine
PTFE	Polytetrafluoroethylene
SDS	Sodium dodecyl sulfate
SOPC	1-stearoyl-2-oleoyl-sn-glycero-3-phosphocholine
TEM	Transmission Electron Microscopy

CHAPTER 1

INTRODUCTION

The plasma membranes of mammalian cells enable selective transport with their environments while supporting communication, compartmentalization, interactions between cells, and energy transduction.[1] Since the membrane is highly sensitive to changes in the extracellular and intracellular environments, for cells, it is important to maintain membrane integrity. If the membrane is disrupted (**Figure 1.1**), it can result in calcium toxicity, the initiation of proteolysis, osmotic stress, oxidative damage, and even cell death.[2] Membrane integrity is strongly dependent on its mechanical properties.[3] Past studies showed that changes in the mechanical properties of the membrane may result in critical diseases, for example, the toxic accumulation of psychosine is related to localized rigid areas of membranes and therefore Krabbe's disease.[4,5] Moreover, membrane elasticity can be correlated with cell elasticity in some contexts. Studies showed that cancer cells exhibit higher elasticity or softness when compared with normal and healthy cells, highlighting the importance of early diagnosis of cancers since cancer cells change and optimize their elasticity for migration during metastasis.[6–8] There are common guest molecules in the cell membrane that regulate the mechanical properties of the membranes, such as surfactants, cholesterol, and ceramides.[9–11] The cell membrane naturally consists of these common guest molecules, and changes in their composition alter the mechanical characteristics of cell membranes. Cholesterol is the most common molecule that controls the mechanical characteristics of the cell membrane.[12,13] However, excess cholesterol can alter the roles of membrane proteins, reduce, or enhance membrane fluidity, and lead to cell malfunction and death. Excess cholesterol has recently been linked to common illnesses, including non-alcoholic fatty liver disease, Alzheimer's disease, and chronic kidney disease.[14–17] Therefore, it is important to monitor and sense cholesterol levels in the cell membranes to

prevent such diseases. To study the effect of cholesterol and other guest molecules, synthetic bio-relevant and biologically-driven phospholipids and their vesicles are used as mimic systems for cell membranes since phospholipids are the major components of the cell membranes. Most of the surfactants shift the melting transition temperature of lipid vesicles to lower values, indicating a softening effect.[18] In contrast, ceramides strongly change the mechanical properties of the cell membrane and make the membrane more ordered.[19] These molecules are known to impose a monotonous effect on the mechanical properties of lipid vesicles. However, cholesterol is observed to result in a non-monotonous and non-universal effect on the mechanical properties of the membranes, which depends on the chemical structure of the phospholipids, chain saturation, and phase behavior of the lipid.[13,20–23]

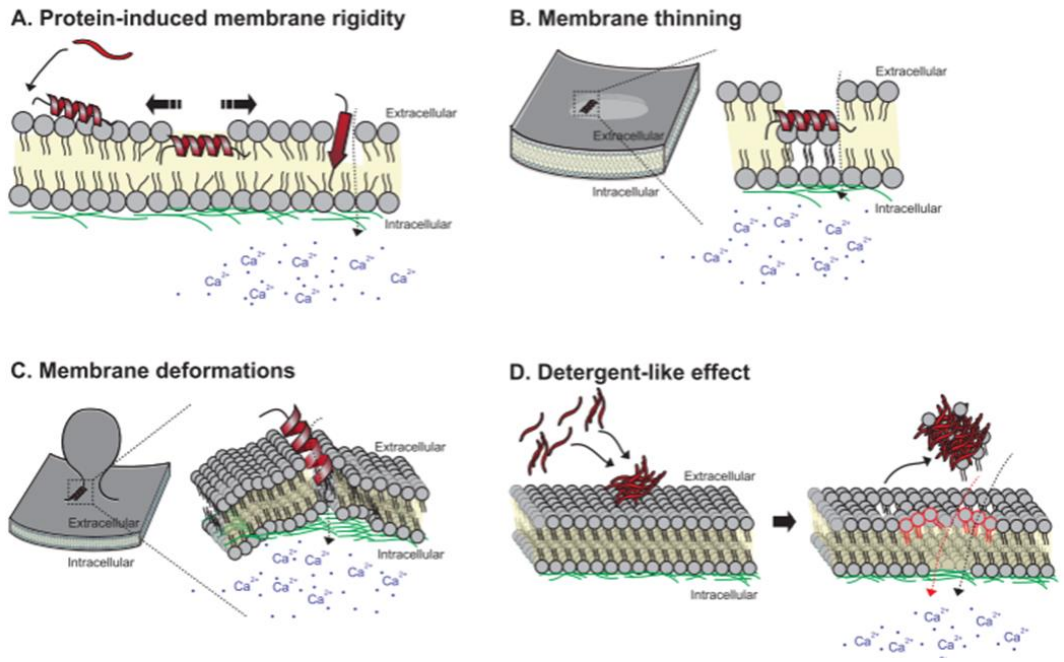

Figure 1.1. Schematic illustration of the disruption of membrane integrity. (a) Protein-induced membrane rigidity, (b) Membrane thinning, (c) Membrane deformations, (d) Detergent-like effect. Copyright © 2021, Catarina Dias & Jesper Nylandsted.

To study the change in the mechanical properties of the cell membrane, the LC-water interface can be used as a tool since the physicochemical properties of liquid crystal (LC)-aqueous interfaces resemble properties of cellular membranes, which makes them excellent mimic systems for studying the interactions and assemblies of biologically relevant species at interfaces. The long-range orientational ordering, fluidity, and optical birefringence of liquid crystals (LC) are unique properties of LC. Among these, 4-cyano-4'-pentylbiphenyl (5CB) is a thermotropic liquid crystal that has been commonly studied (**Figure 1.2a, b**). Moreover, 5CB possesses a nematic phase at room temperature. In this phase, the constituent anisotropic molecules of 5CB, called mesogens, adopt a preferential orientation along a common direction, referred to as the director.[24] Intermolecular interactions between LC and the confining medium result in surface-induced ordering of LC mesogens, called surface anchoring. The director of LC, denoted as n in **Figure 1.2c**, prefers to align along the easy axis, n_e, with the lowest free energy if there is no external field applied. Birefringence, a distinct feature of the optical characteristics of LC, can be described as the difference between are extraordinary (n_e) refractive index and the ordinary (n_o) refractive index: $\Delta n = n_e - n_o$ (**Figure 1.2C**).[25] Birefringence, based on optical retardance, enables the use of polarized light to investigate the ordering of mesogens.

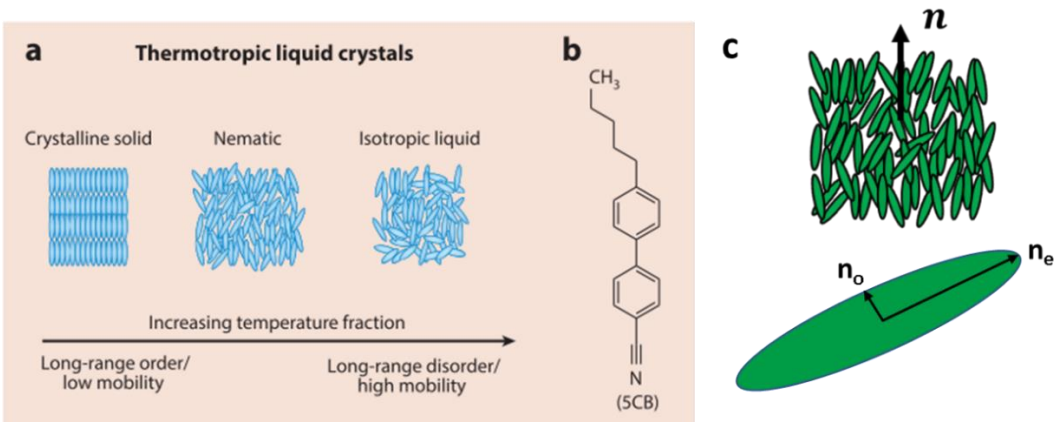

Figure 1.2. Phases of Thermotropic liquid crystals. (a) The illustration of the thermotropic LCs with increasing temperature. (b) Chemical structure of 4-cyano-4’-pentylbiphenyl (5CB). (c) Illustration of the ordering of nematic LCs with

refractive indices. Reprinted with permission from Bukusoglu, E.; Pantoja, M. B.; Mushenheim, P. C.; Wang, X.; Abbott, N. L. Design of Responsive and Active (Soft) Materials Using Liquid Crystals. Annu Rev Chem Biomol Eng 2016, 7(1), 163–196. Permission conveyed through Copyright Clearance Center.

The LC-aqueous interface is soft and deformable; molecules dissolved in the aqueous phase can interact, migrate, and transport to the interface, where they cause changes in the interfacial anchoring of the 5CB mesogens by adsorbing to the interface. In this way, the interface is highly responsive and, most importantly, enables the observation of changes in real time due to the optical birefringence of LC.[25] In the literature, stagnant LC-water interfaces, which possess drawbacks for continuous applications, were commonly used. According to recent research, a stable LC-aqueous interface was achieved in the microfluidic platform while maintaining the responsiveness of the interface to pressure variations.[26,27] This continuous platform enables to investigation of the presence of interfacial species, emphasizing the potential for high-throughput analytical platforms, tracking sophisticated release platforms, and early disease diagnosis.

In this thesis, we investigated the fusion characteristics of biologically relevant and biologically-driven phospholipid vesicles and their complexes with common molecules such as cholesterol, surfactants, and ceramides at the 5CB-aqueous interfaces. Using the unique properties of 5CB in microfluidic systems by creating a soft flowing interface, we aim to provide a platform for understanding the role of rigidity on the phospholipids. We tracked the spatiotemporal changes at the LC-aqueous interfaces caused by the fusion of the vesicles under continuous conditions. We also tracked the temporal changes in the stagnant systems and configuration of 5CB droplets in water emulsions. This designed platform can provide a detailed analysis of the effect of cholesterol on phospholipids, highlighting a non-universal behavior, contributing to the discussions on the effect of cholesterol on the mechanical properties of the phospholipid bilayers in the literature. The findings of our study offer insights into continuously sensing physicochemical

changes in the cell membranes, which are important for understanding diseases related to membrane rigidity.

CHAPTER 2

LITERATURE REVIEW

2.1 Relation between Diseases and Mechanical Properties of Membranes

Diseases such as cancer and sickle cell anemia typically progress with changes in the morphological and structural characteristics of some cells in addition to biological and functional changes.[28] These changes in properties of the cells, and thus of cell membranes, may finally result in the end of cell functions. Therefore, in-depth knowledge and analysis of the mechanical properties of cells provide insights into the underlying mechanisms of diseases and their progression in biological systems.[29] Understanding the mechanism may give insights into detection and early diagnosis, as shown in **Figure 2.1**.

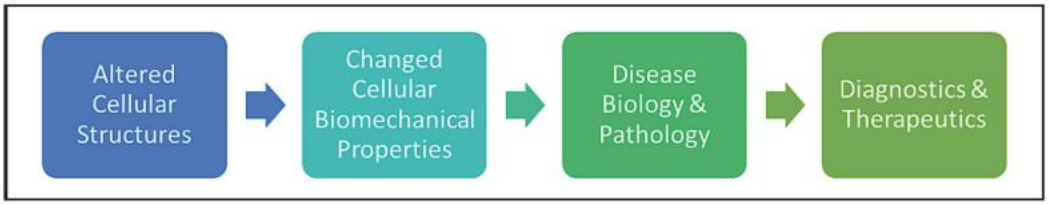

Figure 2.1.Schematic of biomechanical changes. Reprinted with permission of Nematbakhsh, Y.; Lim, C. T. Cell Biomechanics and Its Applications in Human Disease Diagnosis. Acta Mechanica Sinica/Lixue Xuebao 2015, *31* (2), 268–273. Permission conveyed through Copyright Clearance Center.

Examples of mechanical properties of the cells that can be tracked for diagnosis, mentioned above, can be given as elasticity and stiffness. Elasticity of cells can be defined as the resistance of cell membranes to deformation caused by stress, while stiffness is the rigidity of the cell membranes.[30] One of the widely studied diseases associated with a change in the mechanical properties of cells is

cancer. The mechanical properties of single cells are enough to correlate with some cell functions, such as migration, differentiation, and adhesion, which help to understand the cancer mechanism since cancer cells optimize their functions during metastasis. Therefore, single cancer cells can be used as biomarkers for cancer diagnosis. In a study that measured the Young's Modulus of single normal cells and cancer cells, cancer cells have been shown that they can be easily distinguished from their healthy counterparts.[31] To compare them, the relative Young's Modulus (E_R), which is the ratio of the Young's modulus of a cancer cell to that of a healthy normal cell, was used. As seen in **Figure 2.2**, all cancer cells studied possess lower E_R than their healthy counterparts, indicating softening of the cells with cancer progression. Moreover, cancer cells can be divided into different groups according to their values to be able to comment on the results. The bladder cancer shows the lowest E_R values, which indicates significant reductions in Young's modulus with cancer development in the cells. Cancer cells in the ovaries, the prostate, and lung tumors show moderate E_R values. The E_R of esophageal cancer cells is substantial, ranging from 0.55 to 0.65. Thyroid, breast, and kidney cancer cells exhibit E_R levels that fall within wide ranges between 0.25 and 0.8.

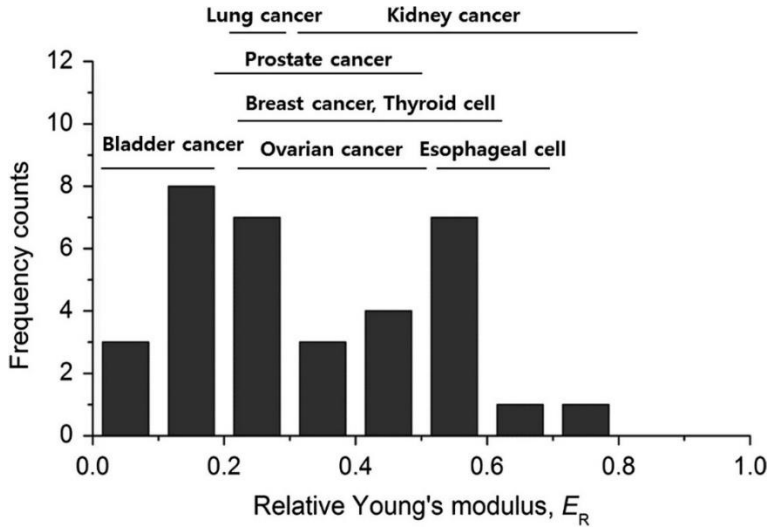

Figure 2.2. Relative Young‘s modulus (ER) in various cancer cells. Reprinted with permission from Quan, F. S.; Kim, K. S. Medical Applications of the Intrinsic Mechanical Properties of Single Cells. Acta Biochimica et Biophysica Sinica.

Oxford University Press, 2016, pp 865–871. Permission conveyed through Copyright Clearance Center.

Another study from the literature showed that all types of cancer cells exhibit a lower Young's modulus value than their normal cells, similar to the previous study. As seen in **Table 1**, breast cancer cells exhibit a Young's modulus trend that was 30–40% lower than their healthy counterparts.[6] Cervical cancer cells show a greater difference in cellular elasticity compared to normal cells, as observed in **Table 1**. These findings suggest that cancer cells definitely exhibit reduced stiffness; however, the amount of the reduction may change according to the origin of the cell.

Table 1.**The average Young's modulus of normal and cancer cells**. Reprinted from Ref. 6. Copyright Ivyspring International Publisher (2020).

Group	Cell line	Young's modulus (kPa)	Relative value
Breast cancer	MCF-10A	13.69 ± 1.9	1.00
	MCF7	9.24 ± 1.39	0.68
	T47D	8.39 ± 1.24	0.61
	MDA-MB-231	9.57 ± 1.38	0.70
Cervical cancer	Ect1/E6E7	48.77 ± 3.33	1.00
	HeLa	25.25 ± 1.89	0.52
	SiHa	21.09 ± 2.42	0.43
	Caski	26.73 ± 3.23	0.55
Lung cancer	WI-38	47.52 ± 2.50	1.00
	A549	15.50 ± 1.74	0.33
	H460	33.54 ± 1.10	0.71
	H1299	39.04 ± 4.45	0.82

Another study using the atomic force microscopy (AFM) technique to measure the elasticity of the cells, which was taken from the region of the cell, showed that melanin granules significantly alter the elasticity of the cells, which is an indicator of the metastatic ability of melanoma cells.[32] They demonstrated that melanin granules provide a protection mechanism for melanoma cells from migrating in a way that was susceptible to many granules. Furthermore, they showed that melanosomes are able to act as an inhibitor. This study concluded that the

spreading of melanoma cells *in vivo* depends on cell flexibility, and this result provides insights into how malignant melanoma spreads.

2.2 Liquid Crystal-Aqueous Interface

Liquid crystals (LC) are a distinct phase of matter that display properties of both isotropic liquids and crystalline solids. They exhibit fluidity like isotropic liquids, while they also maintain a molecular order like crystals. LCs can be classified into two groups as lyotropic and thermotropic. Phases of thermotropic LCs are determined by temperature, while phases of lyotropic LCs depend on the concentration of amphiphilic molecules in the solution.[25] A key feature of the LCs is the long-range ordering of their molecules. In the nematic phase of LC, constituent rod-like molecules, called mesogens, exhibit a preferential orientation along a common direction, called the director.[25] This feature gives rise to optical birefringence, which is generally associated with crystalline solids. 4-cyano-4′-pentylbiphenyl (5CB) is one of the widely studied nematic LCs due to its availability and will mostly be mentioned in this study.

Owing to the anisotropy of mesogens, LC molecules adopt a mean orientation in a confining medium, which is defined as surface anchoring of nematic LC.[33] In the absence of an external field, such as electrical or magnetic, the orientation relative to the surface that minimizes the free energy of the system, and this orientation is known as the easy axis of LC. When external fields are applied, they can induce deviations of the director from the easy axis.[24] Another result of the long-range ordering of molecules is the elasticity of LC. This elasticity causes the three different orientational deformations of LC, which are splay, twist, and bend. The equilibrium configuration of the director is achieved by minimizing the elastic free energy related to the strain of LC.[24] Finally, local orientational order cannot maintain the surface-induced alignment in a confined geometry. As a result, topological defects are established to accommodate boundary conditions. Defects are formed in the strained regions where the LC melts.[24]

LC is immiscible with water and, therefore, creates a stable interface when used with an aqueous phase. The LC-aqueous interface stands out among other interfaces, such as LC-air and isotropic liquid-LC. Some unique characteristics of this interface distinguish it from others, such that it is soft and deformable. Also, adsorbates dissolved in the aqueous phase can be delivered to the interface, and molecular species adsorbed to this interface exhibit high mobility compared to those in the solid interfaces.[25] Combining these properties of the LC-aqueous phase interface with anisotropic properties and optical birefringence of the LC makes it possible to observe the changes at the interface under the microscope in real time.

Past studies showed that properties of the LC-aqueous interface mentioned above provide a platform to understand the coupling between the anisotropic ordering of LC and the organization of the monolayer adsorbed into the interface.[34–36] In the study shown in **Figure 2.3**, 0.1 mM L-DLPC (at 25 ºC, L-DLPC is liquid-like), containing 1% TR-DPPE, and 5CB was used with grids supported on OTS-treated glasses. Each square determines an interface between 5CB and the aqueous phase. The optical texture of the 5CB and the lateral organization of the adsorbed lipids were tracked using microscopy methods. As seen in **Figure 2.3a**, upon introducing the lipid dispersion, initially, the LC-aqueous interface appears bright with brush textures under crossed polarizers. This indicates the planar orientation at the interface, which means that mesogens are aligned parallel to the interface. Lipids are not present at the interface, yet as proved in the fluorescence images (**Figure 2.3a, e**). After 15 minutes (**Figure 2.3b**), dark domains start to be observed under crossed polarized images, indicating that phospholipids adsorb into the interface, and the adsorbed ones change the orientation of the interface from planar to homeotropic. In the homoetropic anchoring, mesogens are aligned perpendicular to the interface, and appear dark under crossed polarizers. Fluorescence image (**Figure 2.3f**) proves that dark domains observed in polarized optical micrographs correspond to phospholipid-rich domains. The lipid-rich domains grow and spread along the

interface with time, within 45 minutes (**Figure 2.3c, g**), and eventually the interface is fully covered with lipid domains after 120 minutes (**Figure 2.3d, h**).

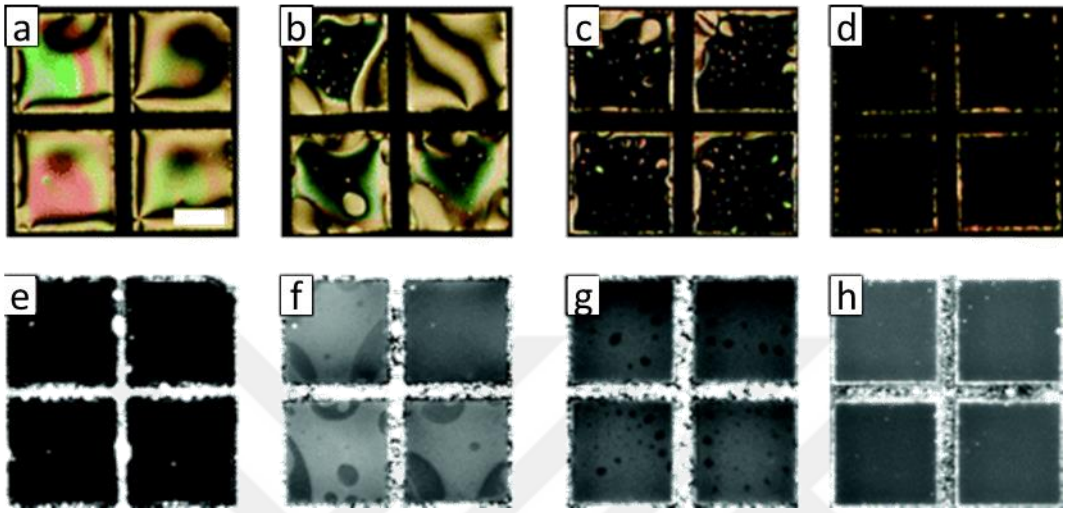

Figure 2.3. Polarized optical micrographs during the fusion of L-DLPC vesicles to the interface. The polarized optical micrographs (a-d) and corresponding epifluorescence micrographs (e-h) of the phospholipids at the aqueous-5CB interfaces. Images were collected at the (a and e) 0 min, (b and f) 15 min, (c and g) 45 min, and (d and h) 120 minutes after the lipid solution was added. Scale bar, 150 μm. Reprinted with permission from Brake, J. M.; Daschner, M. K.; Abbott, N. L. Formation and Characterization of Phospholipid Monolayers Spontaneously Assembled at Interfaces between Aqueous Phases and Thermotropic Liquid Crystals. Langmuir 2005, 21 (6), 2218–2228. Copyright (2005) American Chemical Society.

Another study using similar systems, which is a stagnant system based on a grid supported on a hydrophobic glass (OTS-treated), reported that formation of L-DLPC-rich domains at the interface is driven by the nematic elasticity of LC.[34] As depicted in **Figure 2.4a**, introducing lipids to the aqueous-5CB interface for 10 min from a 10 μM unilamellar vesicle solution of L-DLPC (doped with 0.1% Texas-Red-DPPE) results in a heterogeneous interface of 5CB and aqueous phase due to phase

separation of the lipids. This interface consists of lipid-rich and lipid-lean domains. As shown in **Figure 2.4e**, the dark regions in the optical micrographs, indicating lipid-rich domains, show that mesogens align perpendicular to both the glass and the LC-aqueous interface, whereas the bright regions represent LC that is anchored parallel to the LC-aqueous interface and perpendicular to the glass, as mentioned previously. To prove the presence of the phospholipids, fluorescence imaging was used, and it was found that fluorescence intensity corresponds to lipid domains (**Figure 2.4b**). When 5CB was heated to 34ºC, since 5CB is at the isotropic phase at 34ºC, the birefringent and lipid-lean regions are not seen anymore, as seen in **Figure 2.4c** and **d**. However, when 5CB, whose interface with the lipid deposition was cooled from 34 to 32ºC, turning it to the nematic phase from the isotropic phase, domains are seen to develop. Moreover, they found that these lipid domains lasted for 38 hours at the interface. Although the lipid monolayers at isotropic interfaces exhibit temperature-dependent phase behavior[37], the nematic to isotropic transition temperature and lipid monolayer surface phase transition coincide, indicating a coupling between these mechanisms. These results imply that phase separation of adsorbed amphiphiles at the interface is caused by the nematic order in the LC film. As seen by the free energy computed as a surface fraction of lipids at the interface in **Figure 2.4f**, nematic elasticity in the presence of either strong or weak anchoring may result in a miscibility gap. The tendency to phase separate decreases for weak anchoring, and phase separation is not seen in the absence of nematic elasticity. The key conclusion of the study was that phase separation does not occur in the absence of nematic elasticity under some conditions; however, nematic elasticity of LC can cause the lipid monolayer to phase separate under the same conditions.

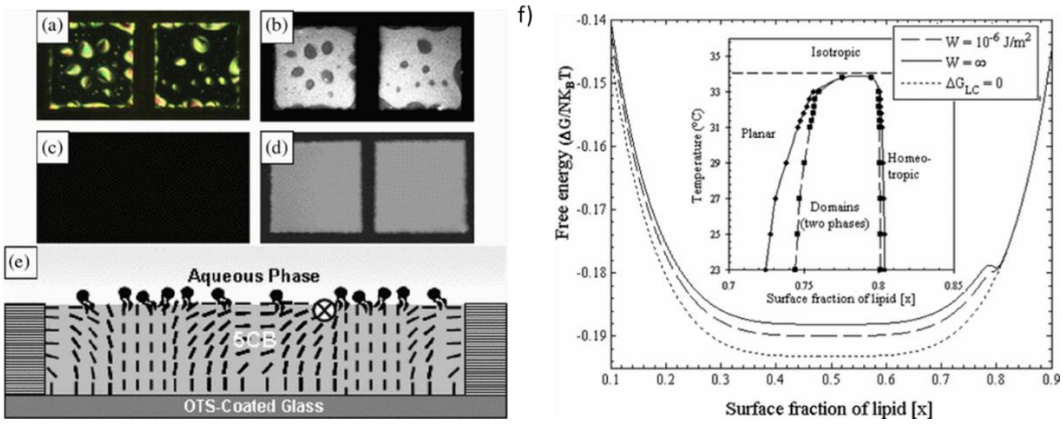

Figure 2.4. Elastic energy-driven phospholipid domain formation at the 5CB-water interface. (a) Polarized optical micrograph under crossed polarizers of 5CB-DLPC aqueous interface. (b) The fluorescent image corresponds to lipid-rich domains. (c), (d) Images of the interface when (a) and (b) were heated to 34 °C and equilibrated for 2 hours. (e) Sketch of the organization of lipids at the interface and 5CB orientation. (f) Plot of dimensionless free energy versus surface fraction of lipids. Reprinted with permission from Ref. 34. Permission conveyed through Scientific Publishing and Remittance Integration Services, Inc.

Another study was done with 5CB in the stagnant systems, which shows that the fusion of assemblies of amphiphilic molecules at the interface results in spatially localized and transient flashes of light.[38] Tsuei et al. performed experiments on films with 20 μm-thick metal grids supported on DMOAP-coated glass slides, which orientation of the system is shown in **Figure 2.5a**. When the system is submerged in an amphiphilic solution containing 25 μM alkyl-triazole oligomers (O1), the interface appears bright with dark brushes initially (**Figure 2.5b**), as mentioned in the previous study. They found retardance values of 1400 ± 70 nm (0 min, **Figure 2.5b**), 650 ± 210 nm (20 min, **Figure 2.5c**), 300 ± 140 nm (40 min, **Figure 2.5d**), and 0 nm (60 min, **Figure 2.5e**), indicating that the LC showed a time-dependent evolution of interference colors. As time increases, the orientation of the interface changes continuously from planar to homeotropic. A dark optical state, which corresponds to homeotropic anchoring of the LC, is the endpoint of the continuous

transition (**Figure 2.5e, f**) since the interface is fully covered. To characterize the transient flashes of light indicated in **Figure 2.5e**, dashed red lines are called "blinking". Spatial and temporal analysis of the collision was completed with both polarized and bright-field images. The first result is that radially symmetrical rotation of LC generates the blink evident in **Figure 2.5g**, and the tilt angle at 0.06 seconds can be estimated as 23 ± 4°. Secondly, the lifetime of a blink was found as less than a second; however, its value changes with every blinking event, as shown in **Figure 2.5g** plots. Another important result is that the mean size of the footprint of blinks is approximately 100 μm. Finally, Tsuei et al. found that the frequency of blinking decreases with the number density of vesicles in the aqueous phase when using vesicles made from 100 μM DLPC. This is consistent with single vesicle events, and the lifetime of each blink depends on the size of the vesicles (800 ± 80 nm to 150 ± 30 nm). Vesicles with a diameter of 940 ± 290 nm produce 47 ± 9 blinks min^{-1} mm^{-2}, showing that the fraction of vesicle collisions that result in fusion with the LC interface is approximately 10^{-3}.

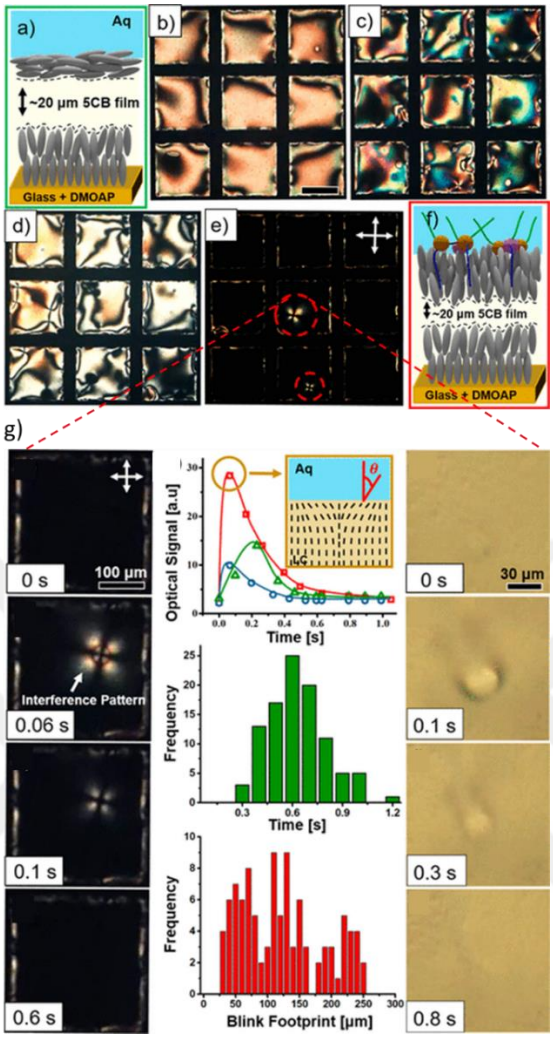

Figure 2.5. Localized blinking triggered by lipid vesicle fusion into the 5CB-aqueous interface. (a,f) Sketch of the interface and bulk of 5CB orientation (side view) and (b,e) corresponding polarized optical micrographs (top view) of aqueous-LC interfaces exhibiting (a,b) planar or (e,f) homeotropic anchoring of mesogens, before or after fusion of O1 into the interface, respectively. (g) Interference patterns shown by polarized optical and bright field micrographs, and frequency plots. Durations were given in the images. Scale bar is 200 µm. Reprinted with permission from Ref. 38. Permission conveyed through Copyright Clearance Center.

Another LC-aqueous interface system, rather than stagnant grid systems, is the LC-droplet emulsion system. These systems are commonly studied since they are

easy to prepare due to the immiscibility of LC in water. Droplets also provide size control, and their configurations depend on the size.[39] Nematic droplets can be utilized to detect the presence of various substances in the aqueous phase, in which they are prepared, since their structure are very sensitive to the anchoring conditions on the droplet surface. For instance, adding small amounts of surfactants caused the anchoring of LC to change from planar to homeotropic.[40] As an alternative, small quantities of biological species can alter the configurations of LC droplets in aqueous phases.[41]

Figure 2.6a shows the orientations of LC-droplet configurations and some distinct optical signatures of these configurations. When the aqueous phase consists of only water, LC droplets adopt a configuration called bipolar, as shown in **Figure 2.6a-*i,*** since the LC-water interface adopts planar orientation. In this configuration, two opposed point defects, which are also known as boojums, are located at the poles of the LC droplets. Another configuration is the radial configuration which the director is oriented perpendicular to the interface, shown in **Figure 2.6a-*ii***. In the core of the droplet, one point defect is located.[42] This configuration is observed dominantly in the droplet system when the aqueous phase consists of amphiphilic molecules such as DLPC.[43] The axial configuration of LC droplets whose director aligns parallel to the central axis of the droplet is shown in **Figure 2.6a-*iii***. This configuration occurs with a line defect along the equator of the interface. Axial configuration is generally observed with elongated droplets.[44] The final configuration generally observed in droplets is a pre-radial configuration that possesses a single point defect similar to the radial configuration (**Figure 2.6a-*iv***). The difference between these two configurations is that the point defect is located at the interface in the pre-radial configuration rather than center, like in the radial configuration, and the interface adapts a tilted orientation.[42]

Amphiphiles such as synthetic surfactants and lipids can cause ordering transitions at LC-aqueous interfaces by means of an adsorbate-induced alteration in the surface anchoring energy.[35,40] Lin et. al showed that when bacterial lipopolysaccharide endotoxin (Lipid A) is present in micrometer-sized droplets of

5CB dispersed in aqueous solution, bipolar to radial ordering transitions are observed at bulk concentrations which five times less than needed to fully cover the surfaces of the droplets for other adsorbates. The comparison between adsorbates is given in **Figure 2.6b**.[41] Lipid A does not trigger order transitions via changing the anchoring energy like lipids and surfactants; instead, transitions are triggered by the interaction between lipid A and localized regions of topological defects in the droplet surfaces. Endotoxin is localized at the point defect, which was located at the center of the LC droplet in the radial configuration. This study provides new principles for to design of LC-sensor systems that respond to targeted biological molecules.

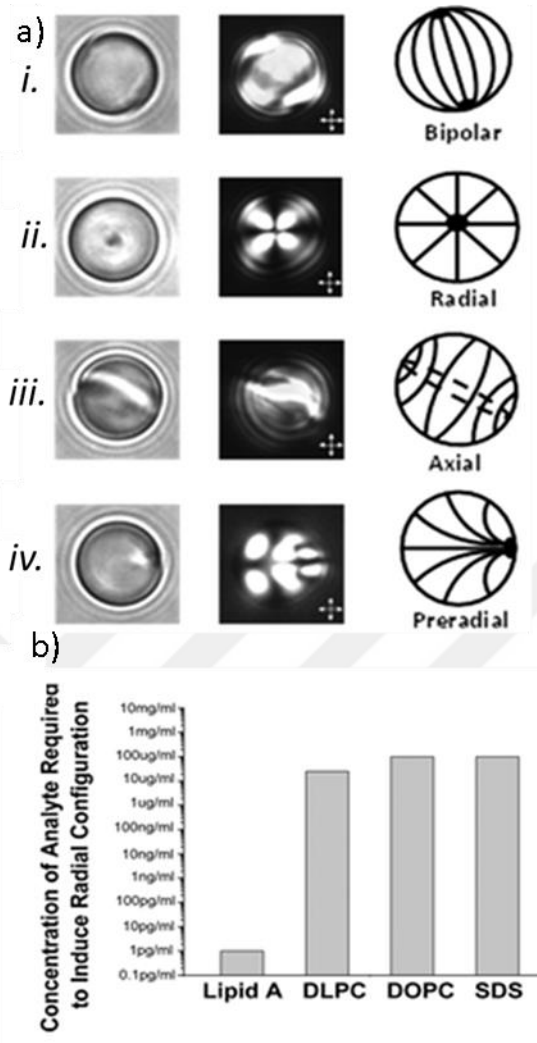

Figure 2.6. LC-in-water emulsions and their configurations. (a) Bright field (left) and polarized optical (middle) microscopy images of 5CB droplets and corresponding illustrations (right) of director configurations (*i*) bipolar, (*ii*) radial, (*iii*) axial, and (*iv*) pre-radial. The size of droplets displayed in the micrographs is 8-μm-diameter droplets. The solid black lines within the droplet boundaries represent the orientation of the LC director, and the black spots represent defects in the droplets. Double-headed arrows in images show the angles of the analyzer and polarizers. (b) Concentration of adsorbate to form radial configuration according to lipid types. Reprinted with permission from Ref. 41. Permission conveyed through Copyright Clearance Center.

2.3 Importance of Extracellular Vesicles in Diagnosis

Cell-derived membrane-enclosed vesicles known as extracellular vesicles (EVs) transport bioactive substances to destination cells. These vesicles are not able to replicate themselves since they do not have a functional nucleus like most cells.[45] In the pathological studies of cancer, extracellular vesicles (EV) have been involved in recent years, and are known as "hallmarks of cancer".[46] Exosomes and shed microvesicles are classes of EVs, indicated as biomarkers and therapeutic tools[47,48] and they can be separated from different body fluids such as blood, urine, and cerebrospinal fluid.[45] These are referred to as biocargos that carry information about inflammatory responses, cell migration, invasion, and metastasis.[49] For example, a study shows that glioblastoma cells release exosomes including mRNA and proteins, reflecting the genetic information of the tumour in body fluids. They found that serum-derived EVs from glioblastoma patients contain mutant mRNA, demonstrating that EVs can be used as liquid biopsy markers.[47] Moreover, another study combined microfluidic technologies showed that EVs containing EphA2, EGFR, CA19-9, indicating pancreatic cancer, GPC-1 for breast cancer, and PD-1/PD-L1 mRNA for lung cancer can be identified as biocargos and biomarkers in potential cancer diagnosis.[50] Also, EVs not only carry information for cancer but also for neurodegenerative disorders, where EVs are isolated from the blood plasma of the brain.[51] Traditional methods for analyzing EVs provide low signal due to averaging and heterogeneous populations, while microfluidic technologies provide higher resolution and more sensitive EV analysis.[50,52]

2.4 Softened and Stiffened Vesicles

To study the effect of guest molecules, synthetic phospholipids and their vesicles are used as mimic systems for cell membranes since phospholipids are the major components of the cell membranes. The surfactants and ceramides impose an autonomous effect on phospholipids; surfactants soften the phospholipids[18], while

ceramides make them stiffen.[19,53] There are various changes caused by surfactants in membranes. One can assume that the bilayer is expanded asymmetrically since surfactants rapidly integrate into only the outer membrane but not into the inner membrane.[18] Also, most of the surfactants shift the melting temperature to lower values. Surfactants are able to enhance the flip-flop behavior due to increased fluidity, and in this way, the selective transport of some solutes through the membrane becomes easier. Flip-flow movement of lipids is the transverse movement of the lipid, different than lateral diffusion of lipids, in which lipids move within the same leaflet of the layer. Flip refers to the movement of a lipid from the outer leaflet to the inner leaflet, while flop refers to the opposite direction.[54] A study that investigated the surfactant-induced flip-flop of an NBD-labeled lipid across erythrocyte membranes found that surfactants such as Triton or $C_{12}EO_8$ are the most active among others since they are able to undergo flip-flop themselves. They found that the flip rate of these lipids in the membranes is 0.002 min^{-1}. They calculated that higher values for weak detergents, such as C_{12}Gluc, $C_{12}EO_3$, and C_{12}TAB, are required to achieve the same results.[53]

A study mentioned in the previous section investigated the use of combinations of water-soluble surfactants and phospholipids to deliver lipid to the LC-aqueous interface faster. Many biologically relevant phospholipids (such as DPPC) exhibit high melting temperatures, and they are in the gel phase at room temperature, which makes them slower to adsorb into the interface.[36] They used TEM grid systems, as mentioned in previous studies. They showed that lipid coverage of the interface can be monitored by adjusting the composition of lipids and surfactants in the mixed-micelle solution. In this study, Brake et al. analyzed lipid coverage after changing the solution of the system with PBS in order to observe the interface covered with only lipids and avoid the desorption of surfactants. As stated in **Table 2**, when a 0.1 mM DLPC and 3 mM DTAB mixture (30:1) is used, the lipid coverage of 51±8% that transferred into the 5CB-water interface is similar to the lipid coverage transferred from only 0.1 mM of DLPC, which was 49±6%. When they used a 100:1 and 300:1 ratio mixed micelle (constant 3 mM DTAB), it is

found that lipid coverage decreased to 32±4 % and 21±5 %, respectively, since the lipid amount in the solution to deliver to the interface decreases. Also, they showed that lipid coverage increases by mixing DTAB with DPPC, which is in the gel state, showing low interfacial lipid coverage due to its state. They concluded that mixed micelles offer a way to transmit phospholipids that are either in the gel or liquid crystalline state to the interfaces of 5CB and water. Furthermore, they showed that it is possible to monitor the coverage of the interface by forming solutions in different ratios of lipid and surfactants.

Table 2. Fluorescence Intensity of Phospholipid-Laden Interfaces. Reprinted with permission from Brake, J. M.; Daschner, M. K.; Abbott, N. L. Formation and Characterization of Phospholipid Monolayers Spontaneously Assembled at Interfaces between Aqueous Phases and Thermotropic Liquid Crystals. Langmuir 2005, 21 (6), 2218–2228. Copyright (2005) American Chemical Society.

Lipid	Aggregate state	Surface	Total surface fluorescence	Relative lipid coverage
L-DLPC	vesicles	SiO_2	17 000 ± 200	1.00 ± 0.01
L-DLPC	vesicles	OTS	8200 ± 1100	0.49 ± 0.06
L-DLPC	vesicles	5CB	8200 ± 1200	0.48 ± 0.07
L-DLPC	micelles (30:1)	5CB	8700 ± 1300	0.51 ± 0.08
L-DLPC	micelles (100:1)	5CB	5400 ± 700	0.32 ± 0.04
L-DLPC	micelles (300:1)	5CB	3600 ± 900	0.21 ± 0.05
D-DPPC	vesicles	5CB	6100 ± 900	0.36 ± 0.05
D-DPPC	micelles (30:1)	5CB	8000 ± 1600	0.47 ± 0.09

Ceramides are a class of sphingolipids composed of sphingosine bonded to a fatty acid via an amide link. When integrated into lipid bilayers, ceramides exhibit unique characteristics not commonly seen in other lipids. They are highly hydrophobic and thus not soluble in aqueous environments, and they enhance the

molecular order and rigidity of membranes.[55] Also, they show a high gel-to-liquid-crystalline phase transition.[56] Ceramides strongly change the mechanical properties of the cell membrane and make the membrane more ordered. [19] A study utilizing the shear rheology showed that ceramide exhibits solid-like behavior with a high shear modulus typically ranging from 300-100 mN/m. Ceramide exhibits a high yield stress much larger than that observed for DPPC.[57]

2.5 Non-Universal Behavior of Cholesterol

A common molecule that regulates the mechanical properties of the cell membrane is cholesterol.[12,13] Cholesterol is essential for controlling the permeability, fluidity, rigidity, and microstructures of the membranes. Although cholesterol is important for the synthesis of bile acids and steroid hormones[58], its excess amount may influence membrane fluidity significantly, change membrane protein functions, and cause cell dysfunctions. Recently, it has been reported that excess cholesterol is related to some common diseases such as chronic kidney disease, Alzheimer's disease, and non-alcoholic fatty liver disease.[14–17] For example, Atherosclerosis is the most well-known and most studied disease caused by excess cholesterol. The condition was characterized by macrophages turning into foam cells as a result of cells scavenging too much cholesterol.[59] Also, cholesterol causes dysfunctions in insulin secretion, and eventually, beta cells die due to its build-up in pancreatic beta cells. A study found that glucose-stimulated insulin secretion (GSIS) is considerably decreased when beta cells are forced to be exposed to high cholesterol medium, such as 10 mmol/L for one hour.[60] Overall, they highlighted that determining the cholesterol amount in media and quantification are critically important in tracking the diseases mentioned above.

The effect of cholesterol (chemical structure and illustration in **Figure 2.7a** and **b,** respectively) on phospholipid bilayers can be characterized by measuring their mechanical properties, such as permeability, fluidity, and bending rigidity.[20,61] The commonly studied property is the bending rigidity (K_c), and according to Helfrich-

Canham theory, the energy required to deform lipid bilayers can be measured by the bending rigidity of lipid bilayers.[62] Cholesterol changes the K_c by perturbing the bilayer and changing its packing[22], as shown in **Figure 2.7c**, **d**. It is required to measure and interpret K_c to understand the alterations of the biomechanics of membranes. Therefore, the scientific community is very interested in the research on bending rigidity.[63] Bending rigidity (K_c) can be experimentally measured by using different methods such as micropipette aspiration, neutron-spin echo spectroscopy, H-NMR spectroscopy, fluctuation spectroscopy, electrodeformation, and vesicle size distribution.[63]

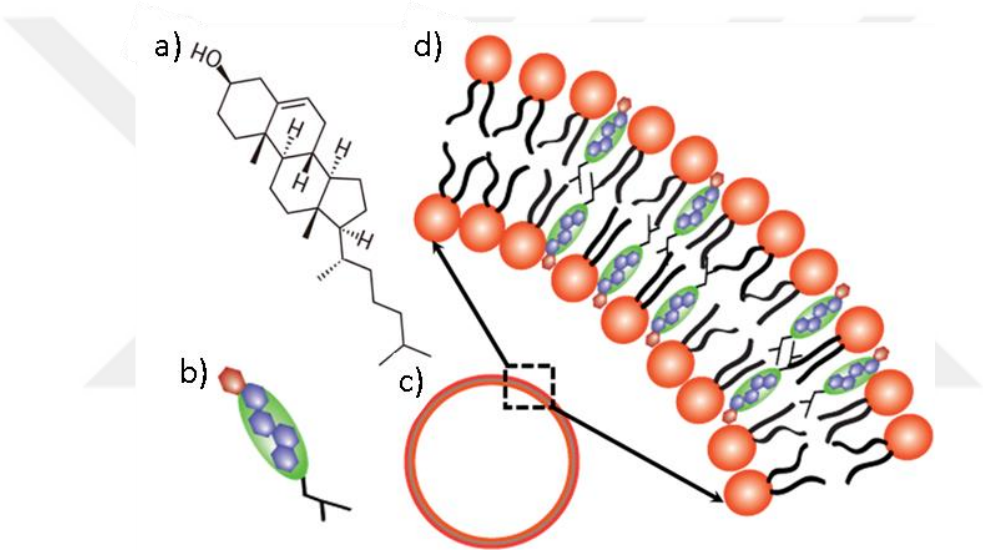

Figure 2.7.**Chemical structure of cholesterol and cholesterol-rich lipid bilayers**. (a) Structure of cholesterol. (b) Illustration of cholesterol. (c) Lipid bilayer schematics. (d) A close view of lipid bilayers, consisting of cholesterol perturbation. Copyright Karal et al (2022).

Cholesterol exhibits a non-monotonous and non-universal effect on bilayers, which depends on the chemical structure of the phospholipids, chain saturation, and phase of the lipid.[13,20–23] For example, one study demonstrated the striking results that cholesterol causes an increment in K_c of the phospholipid that consists of fully saturated chains, but when there are two monounsaturated chains, there is no net trend in K_c.[13] Pan et al. conducted their experiments with 2000 well-oriented bilayers

deposited on silicon wafers, and they analyzed their samples by using NMR. Samples showed thermal fluctuations, which degraded X-ray diffraction peaks. As seen in **Figure 2.8a**, DMPC, which is a saturated lipid, exhibits an increased K_c trend by more than four times when 30% cholesterol was added. In contrast, for 1-stearoyl-2-oleoyl-sn-glycero-3-phosphocholine (SOPC), which consists of one monounsaturated chain, the increase is about twofold when compared to its pure value. Interestingly, for lipids with two monounsaturated chains, such as DOPC and diC22:1, the bending rigidity remains nearly unchanged with cholesterol. Moreover, cholesterol results in increased orientational order, which is analyzed by x-ray diffraction and defined as S_{xray} as indicated in **Figure 2.8b**. Also, it is found that cholesterol thickened the bilayer for all types of lipids (**Figure 2.8c**). The study concluded that the effect of cholesterol on phospholipid bilayers is not obviously universal with different lipids since all lipids include different chain types and different chemical structures.

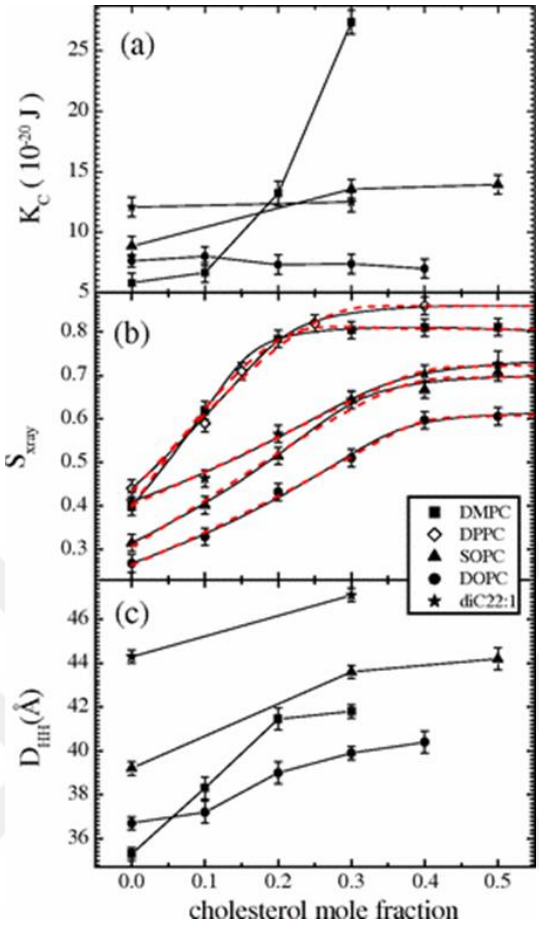

Figure 2.8. **Cholesterol effect on different lipids.** (a) Bending modulus, (b) orientational order parameter, and (c) thickness as a function of cholesterol mole fraction. Reprinted with permission from Pan, J.; Mills, T. T.; Tristram-Nagle, S.; Nagle, J. F. Cholesterol Perturbs Lipid Bilayers Nonuniversally. Phys Rev Lett 2008, 100 (19). Permission conveyed through Scientific Publishing and Remittance Integration services.

A study that combined neutron spin-echo spectroscopy (NSE), NMR, and molecular dynamics simulations in its analysis reported that DOPC exhibits an increase in K_c with increasing cholesterol amount.[23] All three measurement methods not only show that a threefold rise in effective bending rigidity as the cholesterol mole fraction approaches 50% but also they are in good agreement with each other, as seen in **Figure 2.9a**. Cholesterol locally increases the bending rigidity of DOPC

vesicles by increasing the packing density. To test this, Chakraborty et al. plotted bending rigidity against area per lipid, and found that bending rigidity decreases by almost fourfold with increasing area per lipid (**Figure 2.9b**). This result showed that cholesterol increases the stiffness of DOPC by decreasing the area per lipid since it perturbed the bilayer and made the bilayer more ordered. Also, the simulations and NSE analysis gave the same results. This study showed significant biological implications, such that cholesterol causes to bilayer to respond mechanically to changes in the environment.

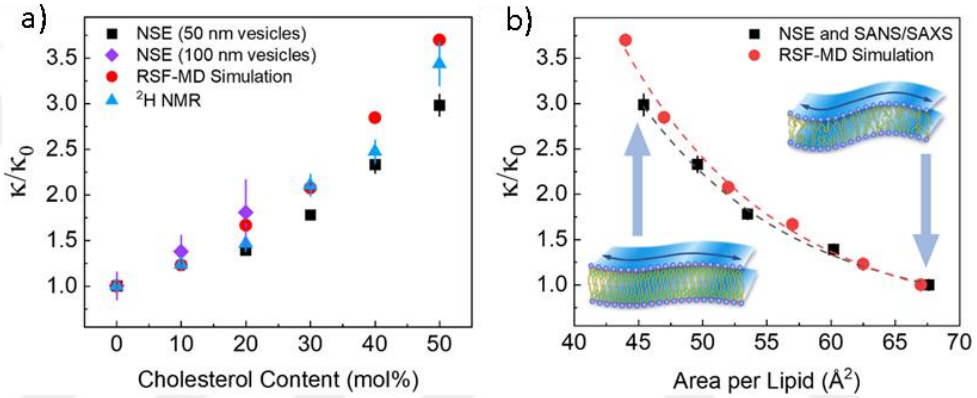

Figure 2.9. **Cholesterol changes the bending rigidity of DOPC vesicles.** (A) Relative bending rigidity with cholesterol amount. (B) Relative bending rigidity against area per lipid. Copyright Chakraborty et al. (2020).

Another study used DOPC, Egg SM, and cholesterol, and analyzed with fluctuation and electrodeformation, showing the effect of cholesterol on the rigidity of saturated and unsaturated vesicles.[20] Gracia et al. analyzed the shape fluctuations of membranes with time on optical microscopy and used a complex mathematical model[64] to obtain K_c. For the electrodeformation, a lipid vesicle was exposed to an AC electrical field, and shape changes were observed and fitted to a model.[65] Gracia et al. showed that the K_c of Egg SM decreases with the cholesterol amount measured by both electrodeformation and fluctuation spectroscopy, as shown in **Figure 2.10**. Pure Egg SM membranes exist in solid phases at room temperature, and therefore, at a very low cholesterol amount, the membrane stays in the solid state, indicating a

higher K_c value. Cholesterol disrupts the solid structure, promoting the liquid-ordered phase, and therefore, fluidity increases with increasing amounts, highlighting a decreasing K_c. The difference values between electrodeformation and fluctuation spectroscopy are not significant in softer membranes such as DOPC, but more obvious for SM: Chol.

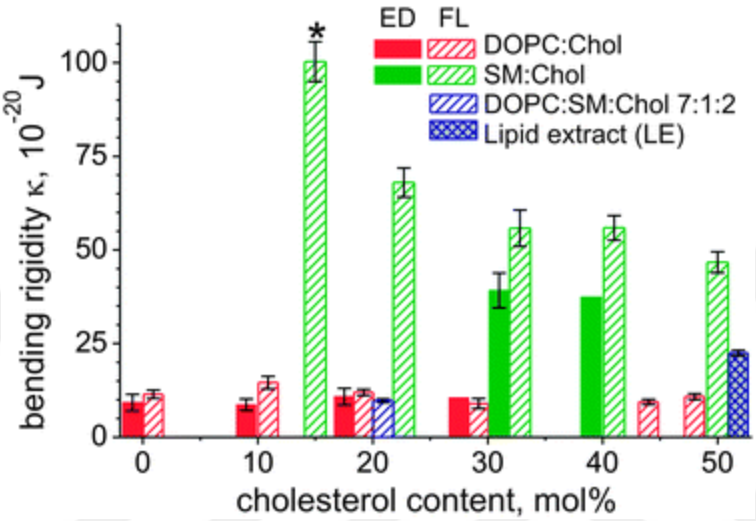

Figure 2.10.Bending rigidity of DOPC and SM against cholesterol content. Plot of bending rigidity (J) vs. cholesterol content (mol%). Values were obtained via electrodeformation and fluctuation spectroscopy**.** Used with permission of Royal Society of Chemistry, from Effect of cholesterol on the rigidity of saturated and unsaturated membranes: fluctuation and electrodeformation analysis of giant vesicles, permission conveyed through Copyright Clearance Center, Inc.

Another study analyzed changes in K_c of different lipids with cholesterol by using coarse-grained modeling at 320 K.[66] As can be seen in **Figure 2.11**, the bending modulus is highest for DPPC with a value of 30.7 k_BT, and increasing levels of acyl chain unsaturation for Egg sphingomyelin (DPSM) (26.7 k_BT), 1-palmitoyl-2-oleoyl-sn-glycero-3-phosphocholine (POPC) (22.1 k_BT), and DOPC (18.8 k_BT) show lower bending moduli than DPPC. At low cholesterol levels, such as up to 20%, the bending modulus remains almost the same for DPPC and DPSM, while it decreases by a small amount up to 5 k_BT for POPC and DOPC. However, at 40 mol%

cholesterol contents, DPPC becomes stiffer, showing 43 k_BT bending modulus, while DOPC becomes softer with a 37% reduction in K_c. The results of this study indicated that the cholesterol effect on membrane rigidity is non-universal and depends on lipid types and the composition of cholesterol. This controversy in the literature, especially considering independent studies that found different K_c trends for the same lipids, shows that cholesterol displays a non-universal behavior on the mechanical properties of the phospholipid membranes. Here, we aim to contribute to this literature by investigating the influence of the rigidity of the phospholipid vesicles on their fusion characteristics at the interface.

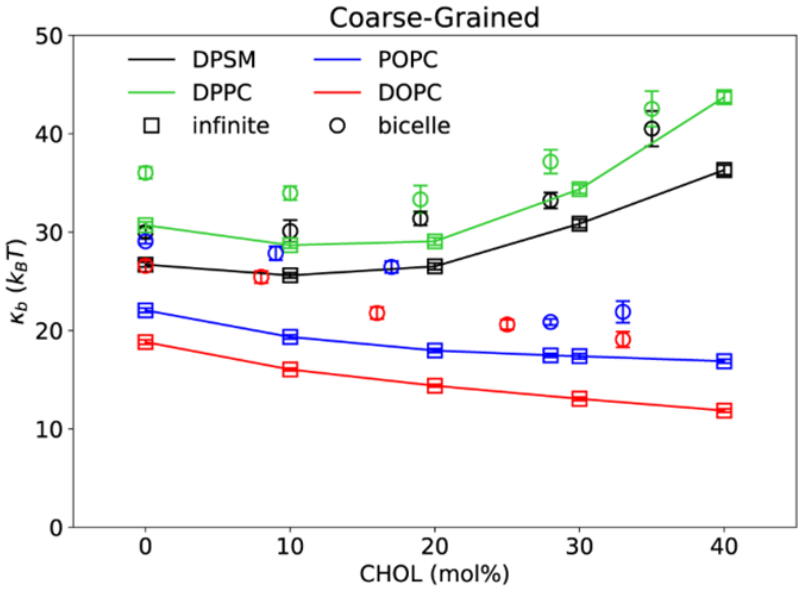

Figure 2.11.Bending modulus of different lipids with cholesterol amount. Bending modulus in terms of k_BT against cholesterol (%) amount. The black line represented DPSM, the blue line POPC, the green line DPPC, and the red line DOPC. Copyright Matthias Pöhnl et al. (2023).

2.6 Liquid Crystal Microfluidics

To date, studies have predominantly been conducted in stagnant LC-water interfaces. However, limitations in continuous and automated applications can be

observed in stagnant systems. Recent studies showed that additional information regarding the mass transfer of the interfacial adsorbates at the elastic LC interfaces can be obtained when mass transfer was coupled with the flow.[67,68] Moreover, these interfaces are important for colloidal interactions due to their ordering profile.[26,27] More recently, studies showed that "flowing" LC-aqueous interfaces can be maintained in the microfluidic systems that are stable up to significant pressure differences and maintain responsive properties against interfacial adsorbates.[26,27] The LC-water soft interface was defined by the preferential wetting of the two phases in those microfluidic channels. The system of interest in these studies can be seen in **Figure 2.12**. **Figure 2.12a** represents the brightfield and polarized optical micrographs of the microfluidic channels with planar and homeotropic interfaces, respectively, while **Figure 2.12b** and **c** represent cross sections of these interfaces. In co-current or counter-current flow configurations, the stability ranges encompass the perpendicular and flow-aligned regimes at low and high flow velocities, respectively.[26] The interfacial and bulk shear alter the nematic director configurations due to anchoring effects at the interface. The direction of applied shear, interfacial anchoring conditions, and initial bulk director alignment cause the change of the mechanical stresses near the interface, which results in different director profiles and eventually defects.[27] This study provides valuable insights for understanding the LC flow and potential for autonomous systems, such as advanced, high-throughput systems using nanoscopic species such as mentioned in this thesis, and the synthesis of functional materials.

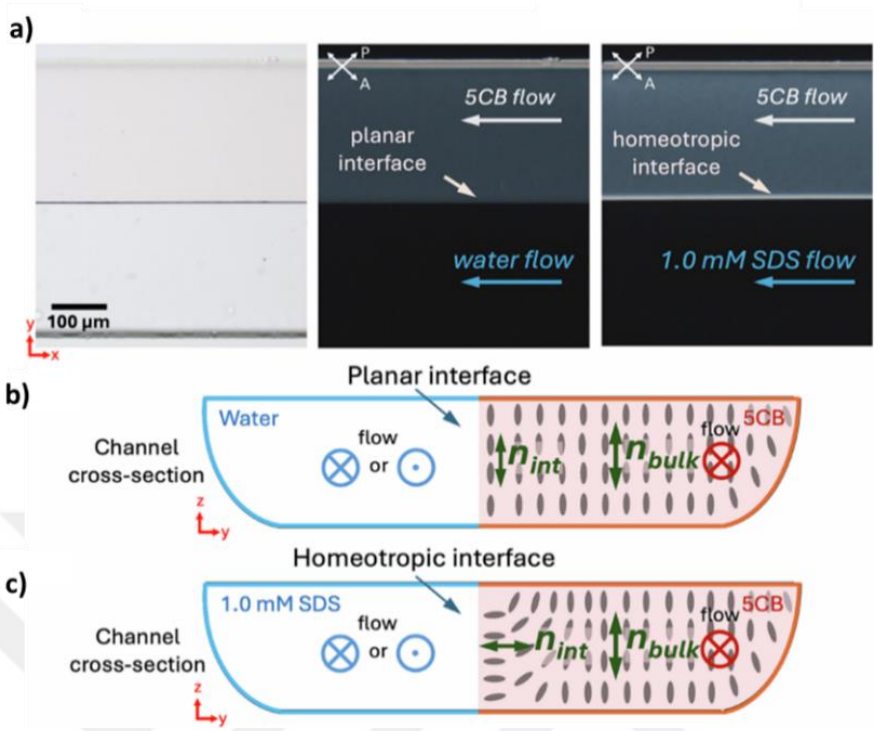

Figure 2.12. The microfluidic soft interface of 5CB-aqueous phase. (a) The brightfield micrograph from top view of 5CB-water simultaneous flow system in a microchannel with 500 µm (left) and polarized optical microscopy images of weak flow with planar (middle) and homeotropic (right) anchoring of the soft interface. The resulting cross-sectional LC director configurations with (b) planar and (c) homeotropic aqueous interfaces. The blue and red circular symbols indicate the flow directions in the cross-sectional illustrations. Copyright 2025, Gülce İlhan et al.

The anionic surfactant SDS is known to produce heterogeneous domains when adsorbed into the interface in the presence of simple salts such as NaBr, since simple salts screen the electrostatic double-layer, causing the formation of domains.[68] In this study, this property was used for both stagnant interfaces and flowing interfaces. **Figure 2.13a-c** shows the stagnant interfaces of planar, heterogeneous, and homeotropic alignments prepared by transporting the mixture of SDS and NaBr into the interface.[26] Moreover, polarized optical micrographs and fluorescence confocal polarized images in **Figure 2.13d-f** demonstrate that NaBr-

induced heterogeneity is established in soft flowing interfaces obtained by the microfluidic channels mentioned above. Bright domains in **Figure 2.13e** match the intensity in the FCPM image. These results confirm that one can track surfactant-driven phase separation and LC orientation directly at soft microfluidic interfaces, as illustrated in the schematic **Figure 2.13**. This continuous system can provide a platform to study both homogeneous and heterogeneous domains of adsorbed surfactants, highlighting the potential for early detection of diseases, tracking advanced release platforms, and high-throughput analytical platforms.

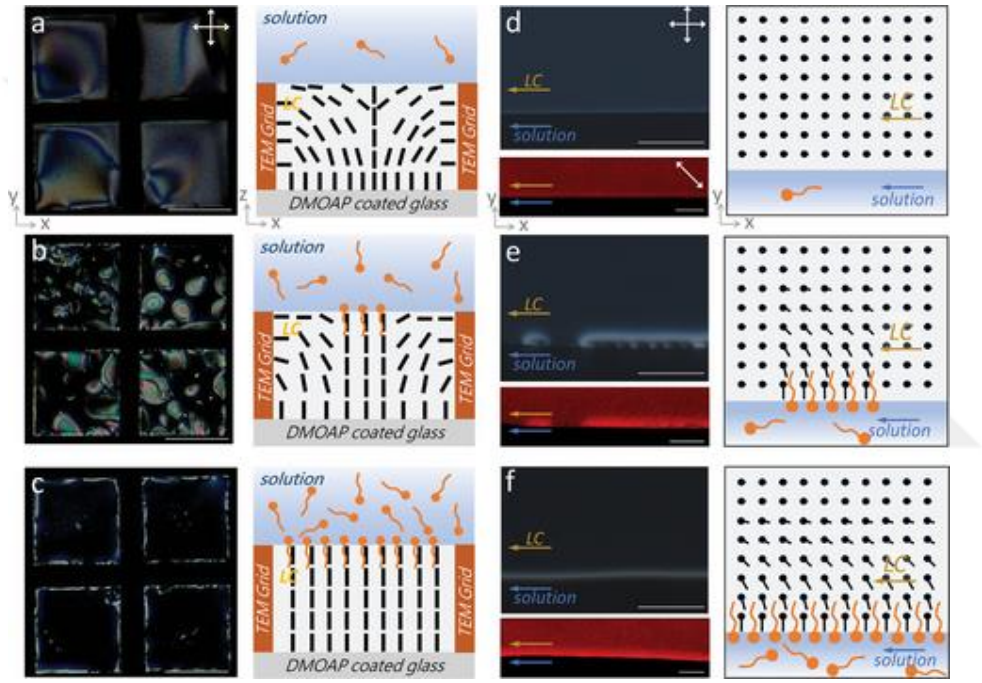

Figure 2.13. Heterogeneous and homogeneous soft interface of 5CB-aqueous phase. Polarized optical microscopy images of a stagnant interface of 5CB obtained with a 25 μm-thick TEM grid with (a) pure water, (b) a solution of 0.023 mM SDS and 1.0 mM NaBr, and (c) 1.0 mM SDS solution, respectively. The representative sketches of the director configuration of 5CB were given next to micrographs. Polarized optical micrographs (top) and fluorescence confocal polarized microcopy images (bottom) of 5CB with aqueous flowing phase as (d) 0.005 mm SDS in 1.0 mm NaBr, (e) 0.015 mm SDS in 1.0 mm NaBr solution, and (f) 1.0 mm SDS solution. The illustrated sketch of the LC configurations is maintained at the middle (h/2) of

the microfluidic channels imaged in (d–f). Scale bars: (a,b,c) 100 μm, (d,e,f) 50 μm for POM images and 20 μm for FCPM images.

In this study, we explored the adsorption of biologically relevant phospholipids and their mixtures with cholesterol, surfactants, and ceramides at the 5CB-aqueous interface. Utilizing a microfluidic system and the responsive nature of LC, we examined the effect of rigidity on vesicle fusion to the soft interface. Our results showed that cholesterol has a variable impact on phospholipid adsorption kinetics and demonstrated the potential of this platform for monitoring membrane-related physicochemical changes relevant to disease mechanisms.

CHAPTER 3

MATERIALS AND EXPERIMENTAL SECTION

3.1 Materials

The room temperature nematic liquid crystal 4-cyano-4'-pentylbiphenyl (5CB) was purchased from HCCH Jiangsu Hecheng Chemical Materials Co., Ltd. (Nanjing, China). Glass slides were taken from Marienfeld GmbH (Lauda-Königshofen, Germany). HPLC-grade acetone, 2-propanol, trichloro(octadecyl)silane (OTS), dimethyloctadecyl[3-(trimethoxysilyl) propyl] ammonium chloride (DMOAP), Nile Red dye, cholesterol (powder), dodecyltrimethylammonium bromide (DTAB), and phosphate buffered saline (PBS) were provided from Sigma-Aldrich (St. Louis, MO, USA). 1,2-dilauroyl-sn-glycero-3-phosphocholine (DLPC), 1,2-dipalmitoyl-sn-glycero-3-phosphocholine (DPPC), 1,2-dioleoyl-sn-glycero-3-phosphocholine (DOPC), egg sphingomyelin (SM, Chicken) and N-(4,4-Difluoro-5,7-Dimethyl-4-Bora-3a,4a-Diaza-s-Indacene-3-Propionyl)-1,2-Dihexadecanoyl-sn-Glycero-3 phosphoethanolamine (BODIPY-DHPE) were purchased from Avanti Polar Lipids. Chemical structures of all lipids were given in **Table 3**. N-((2S,3R,E)-1,3-Dihydroxyoctadec-4-en-2-yl)palmitamide (C16-Ceramide) was purchased from BLDPharma (China). Polydimethylsiloxane (PDMS, Sylgard 184 elastomer kit) was provided by Dow Europe GmbH (Wiesbaden, Germany). The negative photoresist AZ P4620, AZ EBR solvent, AZ 400K developer 1:4, Buffered Oxide Etchant 7:1 (BOE) were purchased from Microchemicals GmbH (Ulm, Germany).

Table 3. Chemical Structures and Melting Temperatures of Phospholipids

Phospholipid	Chemical Structure	T_m (°C)
DLPC	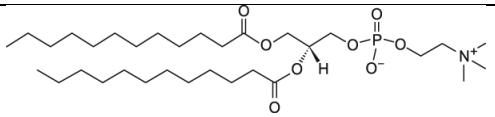	-2
DOPC	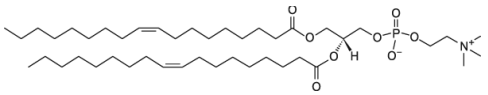	-17
DPPC	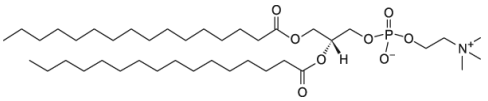	41
Egg SM	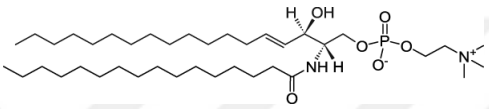	38

3.2 Fabrication of the Microfluidic Channels

The sketch of the mask used in the lithography process is shown in **Figure 3.1**. The microfabrication procedure is as follows. The glass slides were sonicated for 15 minutes in acetone and 2-propanol, respectively, for initial cleaning. Then, glass slides were sonicated in an aqueous DMOAP (1%) solution for 10 min to achieve the hydrophobicity of the glass slides. The photoresist solution was prepared by mixing the photoresist AZ P4620 and EBR solvent in a 1:1 volume ratio. The surface of the DMOAP-coated glasses was coated with a 1:1 photoresist solution by using a POLOS spin coater (SPS-Europe B.V., Putten, The Netherlands). The spin speed was set at 1000 RPM for 50 seconds. Photoresist-coated glass was soft-baked at 110°C for 50 seconds and cooled down to room temperature at ambient conditions for approximately 10 minutes. POLOS Nanowriter (SPS-Europe B.V., Putten, The Netherlands) maskless photolithography was used with an exposure dose of 160 $mJ/cm^{2,}$ laser with a 405 nm wavelength for the channel writing. The glass was treated with AZ 400K developer solution for 80 seconds to dissolve the residue. The developed surfaces were hard-baked for 90 minutes at 110°C. After equilibrating at room temperature, wet etching was done by using a 7:1 BOE solution. Glasses were

located vertically and not touching each other in a PTFE beaker containing the BOE solution and sonicated for 20 minutes. Temperature was controlled by ice for consistency during the process. After etching, patterned glasses were cleaned with fresh distilled ultra-purified water and then rinsed in a jar containing acetone for stripping. The stripping was done in an ultrasonic bath for 10 minutes. Then, glasses are rinsed with copious amounts of acetone, water, and 2-propanol, respectively, and dried with a nitrogen stream. After drying, the channel-etched glasses were ready for the preparation of the microfluidic device. We measured the depth of the resulting channels to be 14 μm by using fluorescence confocal polarized imaging.

The elastomer and curing agent were mixed uniformly in a 10:1 mass ratio to create PDMS. To eliminate the bubbles created during mixing, the mixture was placed in a vacuum chamber for 30 minutes. OTS-coated glass slides were placed in a mold with the prepared mixture (OTS was deposited on glass slides using vacuum deposition for 30 minutes). The PDMS molds were baked for two hours at 60°C to cure them. The PDMS was allowed to cool to ambient temperature following curing. A piece that corresponds to the etched microfluidic channel on the glass slide was cut from the mold. Four ports were punched in the region corresponding to the inlets and the outlets on the glass slide by using a 1.5 mm biopsy punch. The glass-PDMS bonding was performed by oxygen plasma treatment (Diener Electronics, Ebhausen, Germany). After 2 minutes of vacuum and exposure to oxygen gas for 30 seconds under vacuum and 20 seconds of plasma, PDMS and etched glass were bonded.

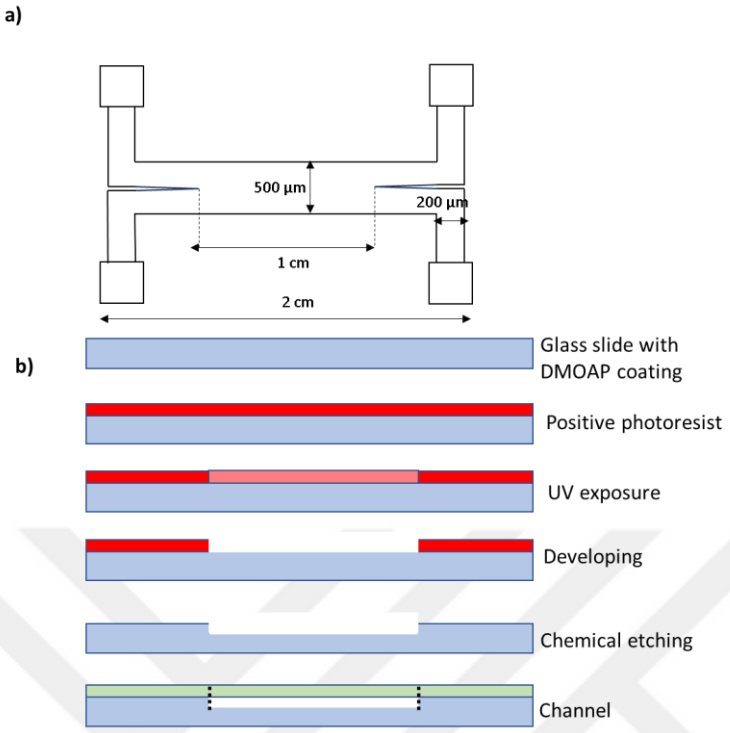

Figure 3.1. Illustration of a mask and fabrication of the microfluidic channel. (a) Dimensions of the mask used in the lithography process of the microfluidic channels, (b) Sketches showing the major fabrication steps of the microfluidic channel.

For the flow experiments, 1.5 mm PTFE tubing was connected to the inlet ports of the channels. Tubing was also connected to an Elveflow OB1 MK3+ (Paris, France) microfluidic flow control system. Using flow focusing in DMOAP solution and a deionized water co-flow system, DMOAP (from a 1% volume solution in water) was coated over roughly half of the channel in its longitudinal direction to create a steady two-phase flow by setting the pressures to 190 mbar for DMOAP and 200 mbar for water. For thirty minutes and three minutes in the ramp, only for the DMOAP flow, the simultaneous flow was guaranteed. The tubing was carefully taken out following DMOAP functionalization. To wash the remaining DMOAP solution, water flow is guaranteed for at least fifteen minutes. 5CB tubing was connected, and the flow was started while the water was running. Throughout the

microfluidic channel, a continuous flow that produced an LC-aqueous interface was maintained. Every flow experiment was carried out in a room setting.

3.3 Preparation of the Stagnant System

Glass slides were covered with DMOAP and then sliced into tiny pieces to produce homeotropic anchoring. On a glass coated with DMOAP, gold-coated TEM grids were positioned and filled with 5CB. A cuvette containing an aqueous PBS solution was submerged in a glass with a TEM grid. To get the required concentration shown in the experiments, a lipid solution was then added to half of the aqueous phase.

3.4 Preparation of Phospholipid Solutions

A glass vial containing 0.5 μL of DLPC (25 mg/mL in chloroform) was filled. The chloroform was evaporated using a nitrogen stream moderate flow. A 5.0 μM DLPC solution was obtained by adding 4 mL of PBS solution. The solution was mixed with a vortex mixer for one minute. To get the required concentration for the studies, this solution was diluted with a PBS solution. Other lipids underwent the same process. Chloroform and powdered cholesterol were combined to create a 25 mg/ml solution. The same process was used to prepare the phospholipid solution after 0.6 μL of this solution was transferred into a glass vial. Solutions of phospholipids and cholesterol were combined in the appropriate proportions. 4.6 mg of powdered DTAB was mixed in 5 mL of PBS to create a 0.3 mM DTAB solution. The DTAB solution was combined with phospholipids in the appropriate ratios after being diluted to the appropriate volume. A batch solution of C16 was made by dissolving 1 mg of powdered C16 in 1 mL of chloroform. The same process was used to prepare the phospholipid solution after 11 μL was transferred from the batch to the glass vial. C16 solutions and phospholipids were combined in the appropriate proportions. A PTFE tubing was used to feed the prepared solutions from the

hydrophilic side of the microfluidic channel into the channels. Size measurements of these solutions were completed by ZetaSizer Ultra (Malvern Instruments Ltd., US).

3.5 Microscopy

A Zeiss LSM 900 Fluorescence Confocal Polarizing Microscope (Jena, Germany) with a linear polarizer and an analyzer for confocal and optical imaging with polarized light was used to image the microfluidic system. In polarized optical microscopy, the orientation of the LC local director was ascertained using crossed polarizers and analyzers at 45° and 135° or 0° and 90° angles. As seen in the pictures, the flow was from right to left, and the microfluidic channels were positioned horizontally from the top perspective for every experiment. To monitor their presence via fluorescence imaging, the lipids were combined with BODIPY (1 v%) labelled DHPE (λ_{ex} = 501 nm and λ_{em} = 512 nm). Nile Red (λ_{ex} = 559 nm and λ_{em} = 635 nm) was mixed with 5CB at a weight percentage of 0.01 for confocal imaging.[69] In fluorescence confocal polarized imaging, the pinhole was 78 μm, and the laser source was excited at a wavelength of 561 nm. Using a 40x objective and a 750 V master gain, images were taken at 4% intensity. An Olympus BX53 (Tokyo, Japan) with crossed polarizers was utilized to image the stagnant systems. Analyzers and crossed polarizers were used at 90° and 0° angles.

CHAPTER 4

RESULTS AND DISCUSSION

4.1 The Three Systems of Interest

We used the nematic LC phase of 5CB in both stagnant films, droplets, and microfluidic flow systems to reveal the response characteristics of the LC phases upon fusion of lipid vesicles to the LC-aqueous interfaces. For all three systems, the 5CB-aqueous interface was obtained by using PBS as a reference, since lipid solutions were prepared in PBS, thereby neglecting charge effects. All images of stagnant system experiments were obtained by polarized optical microscopy by using a 0º and 90º analyzer and polarizer, respectively. 5CB was poured into the wells made by TEM grids held up by a DMOAP-coated glass to construct the stationary film systems as illustrated in **Figure 4.1a**. The TEM grid was located on the DMOAP-coated glass and filled with 5CB, ensuring there was no excess amount of 5CB. The DMOAP coating of glass is known to cause homeotropic anchoring of 5CB on surfaces, and we confirmed this with the dark appearance of the 5CB in air (also homeotropic) under crossed polarizers before starting the experiment. Then, the grid located on the glass was immersed in a cuvette combined with a glass slide that contained 2 mL of PBS. Immersion of the film resulted in a bright optical appearance of 5CB under crossed polarizers, consistent with its planar anchoring at the aqueous interface **Figure 4.1b-*i***, indicating “zero coverage” at the interface. A final concentration of 5.0 μM DLPC was maintained by exchanging half of the aqueous phase with DLPC solution in PBS. The formation of dark areas in the cross-polarized optical images, which are signs of the homeotropic anchoring at aqueous interfaces, occurs after permitting the fusion of the lipid vesicles and the adsorption of the lipids to the 5CB interface with time (DLPC in this experiment). According to earlier research, this optical appearance was linked to the development of the DLPC

monolayer domains at the LC-aqueous interfaces, which resulted in homeotropic anchoring.[36] The interface with these phase-separated lipid-rich and lipid-lean domains was referred to as the "partial coverage" (**Figure 4.1b-*ii***). We designate these dark areas as "lipid-rich" domains. As seen in **Figure 4.1c**, we saw that the dispersed lipid-rich domains at the LC interfaces were random, and the lipid-rich domains interact and merge. Under crossed polarizers, the interface appeared completely dark as more lipids adsorb to it over time, domains expand, and interfacial coverage was achieved (**Figure 4.1b-*iii***). We designated this interfacial coverage as “full coverage” of the interface. As previously reported, we noticed the signs of lipid collision and fusion at the LC interfaces during the adsorption of lipids to the LC-aqueous interfaces.[38] We observed that, at the LC-aqueous interfaces with the other lipids we studied, lipid-rich domains were randomly distributed. However, the timescales of the formation of these domains depended on their type, which is correlated with the melting temperatures (and thus their phases at the experimental conditions), as we also mentioned during this thesis.

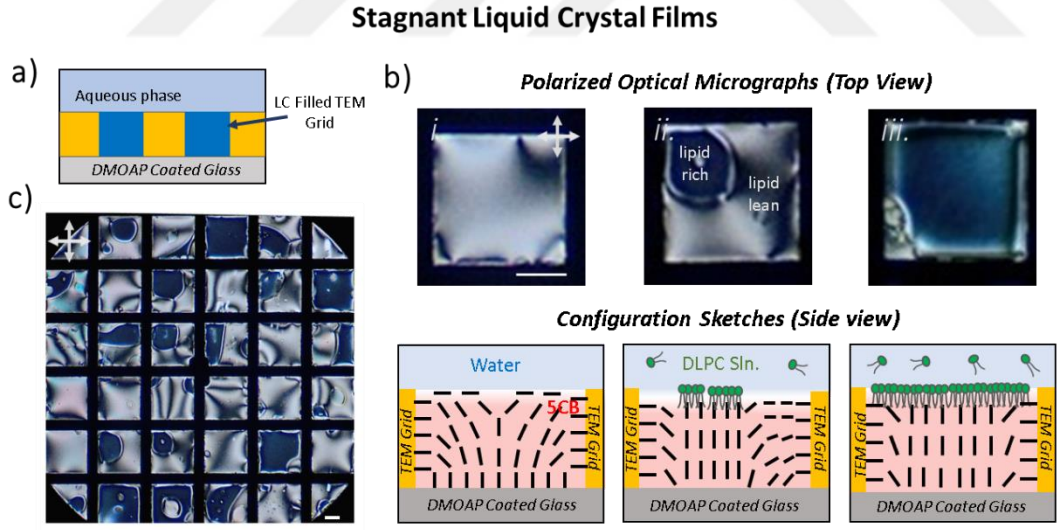

Figure 4.1. Stagnant system of interest. (a) Schematic of the system for stagnant LCs supported in TEM grids, (b) representative polarized optical micrographs (top) and cross-sectional configuration sketches (bottom) of the LC-aqueous interfaces with (i) no lipid adsorption, (ii) partial lipid adsorption, and (iii) monolayer of lipids,

(c) a representative polarized optical micrograph of an LC supported by TEM grid with partial lipid adsorption. For the stagnant systems, a 5.0 μM DLPC solution (in PBS) was used. The stagnant system was equilibrated in 40 minutes. (Scale bars: 100 μm)

For the droplet systems, we created nematic 5CB droplets by mixing 3 μL of 5CB with 1 mL of 0.5 μM DLPC solution. Imaging was conducted by using polarized optical microscopy by using a 0º and 90º analyzer and polarizer, respectively, similar to stagnant systems. LC droplets primarily took on a bipolar configuration in PBS solutions due to the planar interface of 5CB with water, as seen in the brightfield image and POM image under crossed polarizers (**Figure 4.2a**). This configuration indicated “zero coverage” of the interface due to the absence of lipids. Droplets changed to primarily the pre-radial configuration as seen in the brightfield and POM images as a result of the DLPC adsorption to the droplet surfaces, signifying "partial coverage" (**Figure 4.2b**). The droplets primarily adopted radial topologies as DLPC gradually covered their interface, creating a homeotropic interfacial anchoring of 5CB (**Figure 4.2c**), suggesting “full coverage” of the curved interface. The behavior of the coverage of the interface was consistent with the stagnant systems mentioned above. These findings were in line with earlier research, which serves as the foundation for our further studies on how the lipid vesicles' mechanical qualities affect their fusion to the interface and, consequently, the parameters of the LC response.[42]

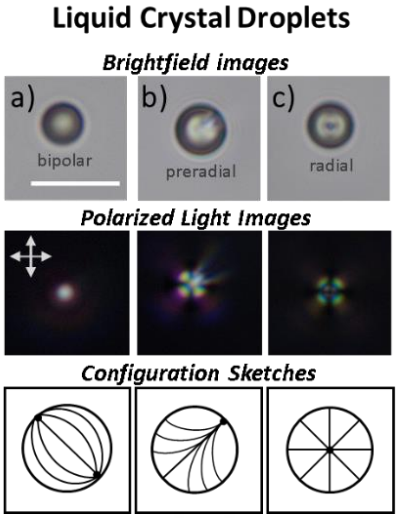

Figure 4.2. Droplet systems. Representative polarized optical micrographs (top), bright field optical micrographs (middle), and configuration sketches (bottom) of (i) bipolar, (ii) pre-radial, and (iii) radial configurations of 5CB droplets dispersed in PBS. For droplet systems, a 0.5 μM DLPC solution (in PBS) was used. The droplet system was equilibrated in 80 minutes. (Scale bars: 100 μm)

In the microfluidic flow systems, a stable flowing 5CB-aqueous interface was formed by the simultaneous flow of 5CB and the aqueous phases in a 14 μm-deep microchannel (**Figure 4.3a**). According to earlier research, the Laplace pressure at the interface stabilizes the interface, which is the result of the preferential wetting of the 5CB and the aqueous phases on the DMOAP-coated (hydrophobic) and bare glass/PDMS (hydrophilic) surfaces of the channels.[26,27] The DMOAP coating was obtained via co-flow of water and DMOAP (1% in volume) in water. The simultaneous flow of water and DMOAP was ensured for 30 minutes and 3 minutes in the ramp for the DMOAP flow. Because 5CB is homeotropically anchored at the DMOAP-coated areas, the 5CB side appeared dark under crossed polarizers in **Figure 4.3b**. However, due to low inlet pressures (15 mbar) being used, which equate to low average velocities (~8 μm/s), there was also little distortion of the LC director with the flow. The black appearance of the 5CB-aqueous interfaces under crossed polarizers, as seen in **Figure 4.3b-*i***, further supported our claim that the 5CB

adopted a planar anchoring at aqueous interfaces, similar to stagnant systems. **Figure 4.3a** (bottom) displays the cross-sectional arrangement of the LC director that corresponds to this state, highlighting LC mesogens aligned parallel to the interface since only water is flowing. Since LC mesogens were oriented parallel to the aqueous interface but perpendicular to the imaging plane, the black appearance of the LC-aqueous interface in channels under crossed polarizers differed from stagnant systems, whose interface appeared bright. When the aqueous phase was introduced as a 0.5 μM DLPC solution, we observed the formation of bright domains at the aqueous interfaces (**Figure 4.3b-*ii***). The DLPC adsorption to the flowing LC-aqueous interface was assisted with P_{aq} = 5 mbar and P_{5CB} = 15 mbar. As illustrated at the bottom of **Figure 4.3b-*ii,*** formed DLPC domains were associated with the adsorption of DLPC into the flowing interface, resulting in homeotropic interfacial anchoring of 5CB. Moreover, we also observed a similar trend in microchannels as in the stagnant systems formed within TEM grids; the interface reached full coverage with lipids (**Figure 4.3b-*iii***) over time since more lipids were adsorbed with time.

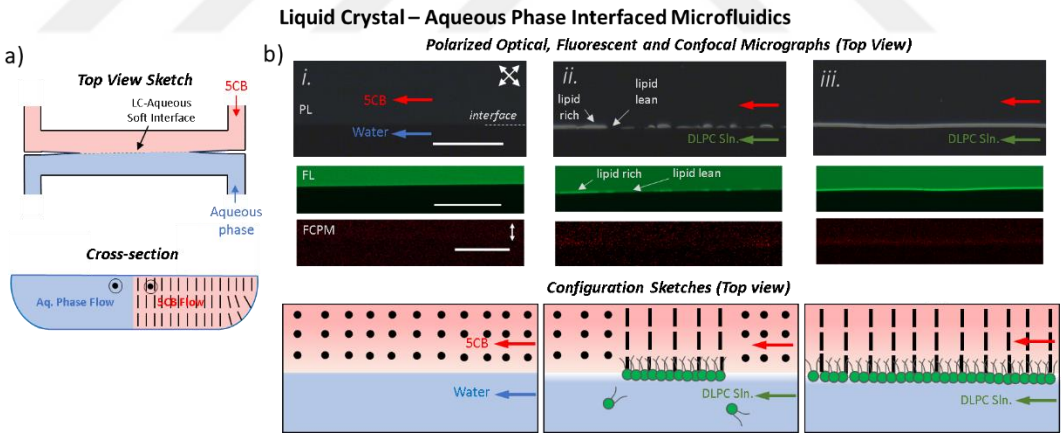

Figure 4.3. Microfluidic system of interest. (a) Schematic of the system for microfluidic LC-aqueous interfaces, (b) representative polarized optical micrographs (top), fluorescent micrographs (second row, BODIPY-DLPE), fluorescent confocal micrographs (third row, Nile Red-doped 5CB), and cross-sectional configuration sketches (bottom) of the microfluidic LC-aqueous interfaces with (i) no lipid adsorption, (ii) partial lipid adsorption, and (iii) monolayer of lipids. For flow

systems, a 0.5 μM DLPC solution (in PBS) was used. The flow system was equilibrated in 40 minutes. (Scale bars: 100 μm)

For the polarized optical imaging when the analyzer and polarizer configurations were 0° and 90°, respectively, a black appearance was observed at the interior of the adsorbed DLPC-rich domains, supporting the homeotropic anchoring of the 5CB at the lipid-rich domains in microchannels (**Figure 4.4-*ii, iii***). The sides of the domains appeared bright due to the strained local directors. For further evidence of the presence of the phospholipids, fluorescence imaging and fluorescence confocal polarized microscopy were used. To maintain BODIPY-labeled DHPE was combined with the DLPC solution, a 1% BODIPY-DHPE was used for fluorescence microscopy imaging. We observed fluorescence intensity at the interface, where we observed a bright appearance in the crossed polarized images, corresponding to lipid domains. To further demonstrate the existence of the DLPC and the alterations of the LC anchoring at the interface with lipid adsorption, we employed fluorescent confocal polarized microscopy (FCPM). We employed a 0.01% composition of Nile Red fluorophore and 5CB. The Nile Red fluorophore aligns parallel with the director of 5CB, having a polarization-dependent absorption spectrum of excitation light. The highest intensity of light is achieved when the polarization and local director orientation are in the same direction.[70] Therefore, the angle of the polarization is critical to interpret the orientation of the LC director. FCPM images taken with and without the presence of adsorbed lipids were indistinguishable at 0° polarization since there was no expected alignment parallel to the direction of excitation polarization. As observed in **Figure 4.4b-*i*, *ii*, *iii***, there is no intensity at 0° polarization for all three cases. However, we observed higher fluorescence signals at the interface at 45°, 90°, and 135° polarization (**Figure 4.3b** for 90°, **Figure 4.4c,d** for 45° and 135°, respectively), supporting the change of the interfacial anchoring of LC from planar to homeotropic with the adsorption of DLPC. The alignment change brought on by the presence of DLPC was supported by the same pictures that showed no discernible intensity variation at the interfaces when DLPC was absent.

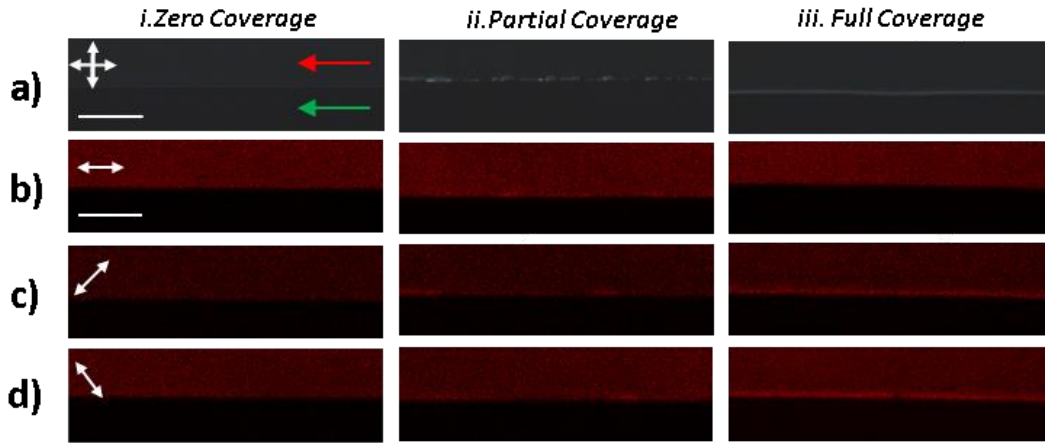

Figure 4.4.Further evidence of the presence of phospholipids at the interface. Images of the channels with and without DLPC adsorption. a) Polarized optical micrographs of the LC-aqueous microfluidic channel under 0° analyzer and 90° polarizer, FCPM images of the same channel at b) 0°, c) 45°, and d) 135° polarization of the excitation source. The dashed line in the images indicates the location of the horizontal soft interfaces. Scale bars: 100 μm.

4.2 Characterization of LC Alignment at the Aqueous Interface Due to the Presence of Lipids

We characterized the DLPC-rich domains at the LC-aqueous interfaces by using polarized optical micrographs and analyzing the intensity distribution from FCPM images at 45° and 135° polarization. Our first observation was that there were commonly two types of DLPC-rich domains. The first type of domains shown in **Figure 4.5a-*i*** appeared bright inside under the 45° analyzer and 135° polarizer, while the second domain, shown in **Figure 4.5a-*ii*** (small domain on the right side) showed dark brush textures inside. When the arrangements of the analyzers and polarizers were 0° and 90°, a dark appearance was obtained inside the first domain (**Figure 4.5-*i***), and the sides of the domain were bright due to the strained local directors. However, the second DLPC-rich domain (second image in **Figure 4.5a-*ii***) appeared mostly bright under a 0° analyzer and 90° polarizer. These domains were further

analyzed by using FCPM images at 45° and 135°. For the first domain, we found that FCPM images at 45° polarization resulted in a higher intensity at the left side of the domain, whereas imaging at 135° polarization resulted in a higher intensity at the right side of the domain, as given in the intensity plots in the FCPM images of **Figure 4.5a-*i***. The trend in the fluorescence intensity was the opposite for the domain in **Figure 4.5a-*i***. Based on the intensity trends, the average configuration of LC mesogens was illustrated in **Figure 4.5b**. The first domain was labeled as "type A", while the other was referred to as "type B". We also observed that, unlike the type A domains (**Figure 4.5a-*i***), the type B domains do not form independently; they consistently move together with type A domains, as shown in **Figure 4.5a-*ii***, suggesting the presence of a defect structure between these domains. Within the samples we investigated, approximately 66% of the identified 80 DLPC-rich domains were "type A" domains, and 22% were "type B" domains, which were always located near the type A domains (**Figure 4.5c**).

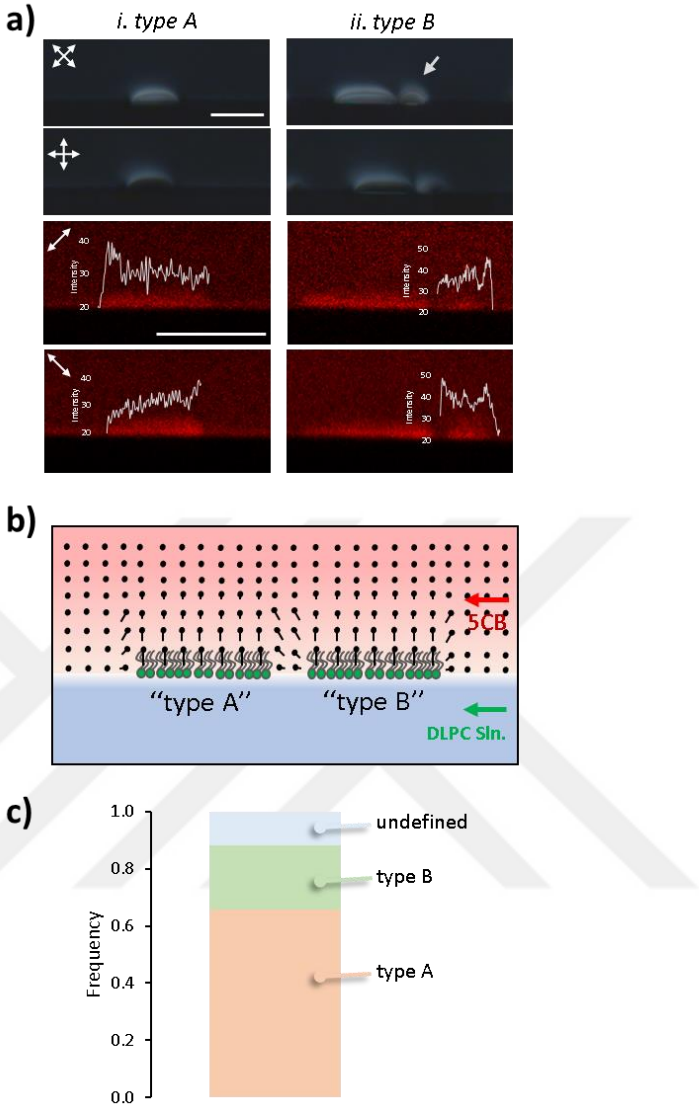

Figure 4.5.Characterization of LC alignment at the interfaces due to the presence of lipids. a) Representative polarized optical micrographs and FCPM images of DLPC-adsorbed interfaces of microfluidic channels. The directions of the analyzers and polarizers of the polarized optical images are shown in the images with double-sided arrows. The polarization direction of the excitation light of the FCPM images is shown with a single double-sided arrow in the images. Scale bars: 20 μm. b) Sketch of representative LC configurations in the vicinity of the adsorbed lipid-rich (DLPC) domains. (c) The frequencies of the types of LC configurations are

defined in the vicinity of the lipid-rich regions. The data was collected from 80 lipid-rich domains.

4.3 Spatiotemporal Characteristics of the Adsorption of Lipids to the LC-Aqueous Interfaces

We utilized polarized optical microscopy to track the spatiotemporal response of the 5CB-aqueous interface when DLPC was adsorbed. We observed that the distribution of the DLPC domains was not random, as observed in the stagnant systems mentioned in previous sections. We monitor the interface in order to understand the non-uniformity by dividing the interface into four distinct regions with the same intervals (1300 μm) as sketched in **Figure 4.6**. The first line of **Figure 4.6** represents the reference images of our interface, which were obtained by the flow of only water. After introducing the 0.5 μM DLPC into the channel initially (at t=0 min), we observed the formation of the initial DLPC-rich domains towards the exit of the channel (n=8), as shown as "location 4" in **Figure 4.6**. With increasing time, at 20 minutes, images showed that fractional coverage increased as the vesicles fused to the LC-aqueous interface. This led to the propagation of the front of the interfacial DLPC-rich region towards the inlet of the channel, as evidenced by the presence of the DLPC-rich region in "location 3" at 40 minutes. Such time scales were significantly different than the anchoring transitions we observed in experiments with singly dispersed surfactants in past experiments, which took less than 1 min.[26,71] Finally, (at t=60 minutes), the interface of location 4 reached full coverage, and location 3 was almost designated as full coverage.

Figure 4.6. Response of the microfluidic, stagnant, and emulsion systems upon adsorption of the DLPC to the interface. The microfluidic channel (14 μm) is divided into four locations named 1, 2, 3, and 4 for polarized imaging, where Δx = 1300 μm. The polarized optical micrographs of the microfluidic system were taken every ten minutes for one hour, where the aqueous phase was introduced as 0.5 μM DLPC (n=8).

We also demonstrated that raising the DLPC concentration of the aqueous phase enhanced the development of the DLPC-rich domains, consistent with the increased rate of the fusion of vesicles to the LC-aqueous interface. As seen in **Figure 4.7a,** when 0.05 μM DLPC was used as the aqueous phase, DLPC-rich did not form at the duration of 40 minutes; however, a flow of 0.5 μM DLPC resulted in partial coverage of the interface (**Figure 4.7b**), as expected. Full coverage was achieved immediately with a flow of 5.0 μM DLPC (**Figure 4.7c**) due to an increased number of molecules flowing in the solution. Although the different concentrations of DLPC resulted in different coverages of the interface, the formation of the first DLPC-rich domains close to the exit of the channel was independent of the DLPC concentration in the aqueous phase.

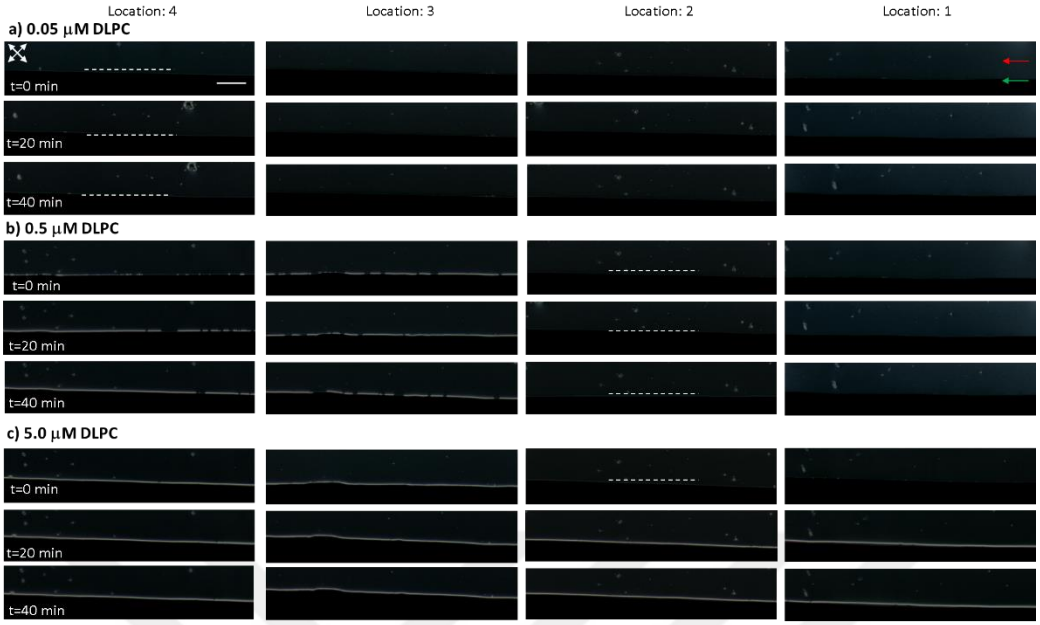

Figure 4.7. Lipid coverage of the interface when lipids are transferred from different concentrations of solutions. Polarized optical micrographs of the microfluidic LC-aqueous interface at locations 1-4 by formed using (a) 0.05 μM, (b) 0.5 μM, and (c) 5.0 μM concentrations of the DLPC feed. Images were collected under a 45° analyzer 135° polarizer. Images were collected at a duration after aqueous phase flow was initiated, as indicated in the images. The white double-sided arrow shows the orientations of the analyzer and polarizers used in all of the images shown in the figure. The dashed lines in the images indicate the location of the horizontal soft interfaces. Scale bar: 100 μm, common for all images. Scale bar: 100 μm.

We also looked into how the DLPC-rich domains formed at the interfaces of stagnant LC systems. In contrast to the microfluidic channels, we found that the DLPC-rich areas formed at the stationary 5CB film surfaces at a slower rate. The pictures in **Figure 4.8a** were taken during an experiment using a 5.0 μM DLPC that was equilibrated with a 5CB film. In contrast to the research carried out with microfluidic systems, it was demonstrated that the development of the partial coverage was maintained in 70 minutes, even with the higher concentrated DLPC vesicle suspensions, while the microfluidic system provided a higher coverage in 40

minutes. This result led to the flow helped to enhance the phospholipid adsorption into the interface due to the increased mobility of the molecules. The formation of a monolayer of DLPC at their interfaces was consistent with the observation that a considerable fraction of 5CB droplets initially maintained a pre-radial and bipolar shape, which gradually transitions into a radial configuration in 0.5 μM DLPC (**Figure 4.8b**). The significance of the flow in promoting the fusing of the lipid vesicles to the LC interfaces was shown by the fact that this rate of configuration change was similar to the microfluidic experiments. Therefore, we deduced that the dynamics of the systems we studied were connected with the formation properties of the DLPC monolayers at the LC interfaces.

We calculated the Peclet number (Pe) in the microfluidic system to be larger than 2500, using the relation Pe = uL/D, where u is the average flow velocity (measured as 135 μm/s experimentally), L is the characteristic length which is 250 μm, and D is the mass diffusion coefficient (measured as 1.13 ± 0.23 $\mu m^2/s$ for DLPC by using dynamic light scattering (DLS)). This high Peclet number value indicated that advective transport dominated over diffusion, which means that lipid vesicle delivery to the LC-aqueous interface was largely confined to the fraction of vesicles already near the interface during flow. As the vesicles flow through the channel, they could fuse into the interface at the end of the channel. As a result, we observed that initial lipid-rich domains preferentially formed near the outlet of the channel, emphasizing the significance of finite fusion rates of vesicles with the LC interface as mentioned above. To further analyze this kinetics, we conducted COMSOL simulations incorporating the experimentally determined channel geometry, flow velocities, and diffusion coefficients (detailed in **Appendix A**). The simulations led us to understand that lipid domain accumulation at the interface initiates near the channel outlet and progressively moves upstream toward the inlet over time. Although these results qualitatively mirrored our experimental observations, they did not fully capture behavior of the system since we neglected the effect of the elastic properties of the LC ("oil") phase (Appendix A.1). Importantly, we found that the rate at which the lipid layer forms at the interface was strongly governed by the

vesicle fusion kinetics which was described by a reaction rate constant, "k" to characterize lipid vesicle fusion to the interface. Building on this insight, we extended our experiments by varying the lipid type, since different lipids exhibit different elasticities of the vesicles and thereby influence their interfacial fusion behavior.[72]

Figure 4.8. Comparison of the responses of the different systems. (a) The polarized optical micrographs of stagnant films and microfluidic systems at the indicated time points and concentrations, 5.0 μM and 0.5 μM DLPC, respectively, collected from location 4. (d) Droplet configuration distributions for emulsions equilibrated with 0.5 μM DLPC solution. Scale bars: 100 μm.

4.4 Adsorption of Different Types of Lipids to the Microfluidic Soft Interfaces

We conducted microfluidic, stagnant, and droplet system experiments to question how different lipids with different melting temperatures, as stated in **Table 3**, would react to fusion to interface in terms of kinetics. At room temperature, DPPC and Egg SM vesicles exhibit gel-like behavior with varying elasticities, while DLPC and DOPC display fluid-like characteristics.[72–75] We prepared 0.5 μM different lipids in PBS and characterized the temporal behavior on the LC-aqueous interface upon adsorption for each system.

For DOPC vesicles, partial coverage of the interface was reached in the stagnant systems within ~70 minutes (5.0 μM lipids), and a similar partial coverage was reached within 40 minutes (0.5 μM lipids) in the flow systems, as shown in

Figure 4.9a. LC droplet emulsion prepared in 0.5 μM DOPC exhibited radial configuration with time, starting from 41.7% ± 8.8% resulting in 51.9% ± 4.7% (n=3), indicating that fusion of the vesicles to the interface continued with time, as consistent with experiments of DLPC mentioned until this section (**Figure 4.9d**).

For the Egg SM vesicles, we did not observe a measurable adsorption for both flow and stagnant systems. It was evidenced by that there was no change in the anchoring transition of the 5CB at both stagnant and flowing interfaces, as can be interpreted in **Figure 4.9b**. This lack of adsorption was thought to be the gel phase of the room-temperature Egg SM vesicles because of their ceramide backbone.[75] Also, droplet experiments provided further evidence that Egg SM vesicles were not able to fuse into the interface. As seen in **Figure 4.9d**, droplets adopted mostly a bipolar configuration, ~84% (n=3), with negligible change with time, indicating no fusion to the interface. We note that we confirmed the adsorbed Egg SM was able to cause homeotropic anchoring when they adsorb to the interface and form a monolayer. We checked this by softening the vesicles with surfactants (by mixing with DTAB) to aid the delivery of the vesicles to the interface, as done in the literature with DPPC (**Figure 4.10a**).[36]

For the DPPC vesicles, which also exhibit solid-like behavior at room temperature, we expected no adsorption due to their phase. In the stagnant systems, we observed a lack of adsorption consistent with our expectations as understood from the lack no orientational change of the interface within 70 minutes (**Figure 4.9c**). However, after 40 minutes, we saw a noticeable shift in interfacial anchoring of 5CB in the microfluidic systems as a result of their fusion and adsorption (**Figure 4.9c**). This finding showed that shear was able to break through the gel phase barrier of the DPPC and cause it to fuse, which led to DPPC domain formation at the 5CB-aqueous interface. To test this hypothesis, we performed LC droplet tests utilizing both a gentle handshake (minimum shear) and a vortex (~2000 s^{-1} of shear rate, calculations in **Appendix B**). We observed that 5CB droplets in the solution adopt a majority of bipolar configuration (61.4% ± 9.0%, n = 3) when gently mixed, suggesting a limited

adsorption (**Figure 4.9d**). However, for the vigorous shaking case with a vortex, 80.7% ± 4.4% (n = 3) of droplets adopted radial configurations, suggesting that DPPC was able to adsorb and change the anchoring of the interface. This striking result showed that the rigidity of the DPPC vesicles caused by the gel-phase was able to be overcome by shear. Past studies also showed a finite rigidity[76] of the DPPC monolayers (G" ≈ 5G').[57] DPPC gels undergo a structural softening above a critical yield stress, which is 0.2 mN/m, then undergo flow as studied with shear rheology.[57] However, because lipid bilayers are naturally three-dimensional structures different than their one-dimensional structures as monolayers, they are usually identified by their bending rigidity rather than their shear surface modulus or viscosity. Therefore, it is more appropriate to correlate the behavior of our system with lipid bilayer bending rigidity, since the process involves the fusion of bilayer vesicles onto a monolayer at the LC–aqueous interface, and we monitor this vesicle fusion through kinetics. Previous studies showed that DPPC bilayers show greater bending rigidity compared to DOPC bilayers but are less rigid than Egg SM bilayers[77] which provided further evidence to our observation that the DPPC bilayers are able to undergo a shear-induced transition out of the gel phase in experiments with microfluidic channels as understand the anchoring transition of the interface (~200 s^{-1} of shear rate, calculations in **Appendix C**). In contrast, the same shear rate was not sufficient to provide a shear-induced transition out of the gel phase for Egg SM vesicles. These results showed that our microfluidic system can probe the rigidities of the lipid vesicles both through the trackable temporal changes in the interface and controllable shear exerted on lipid vesicles in the vicinity of the LC-aqueous interfaces.

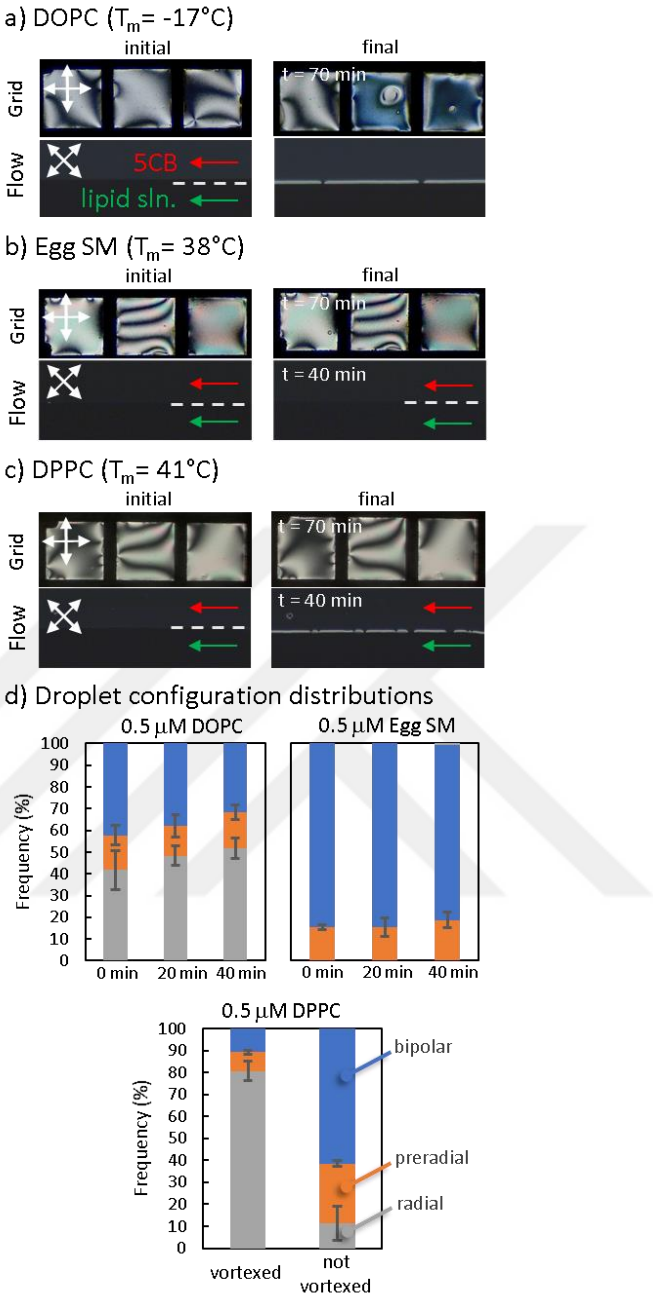

Figure 4.9.Adsorption of different types of lipids into both stagnant and microfluidic LC-aqueous interface. Polarized optical micrographs were collected under crossed polarizer and analyzer 0°- 90° for stagnant systems, and 45°- 135° for flow systems. Experiments were conducted by equilibrating 5CB with suspensions of (a) DOPC, (b) Egg SM, and (c) DPPC vesicles. The lipid concentrations were 5.0 μM for stagnant and 0.5 μM for microfluidic systems. Final images are collected at

40 min for microfluidic systems and 70 min for stagnant films. Flow was assisted with inlet pressures of P_{LC} = 15 mbar, $P_{Aq.}$ = 5 mbar. (d) Droplet configuration distributions for emulsions equilibrated with 0.5 μM DLPC, Egg SM, and DPPC suspensions. Scale bars: 100 μm

Figure 4.10. Coverage of the interface when lipids are transferred from a mixed solution of surfactants. The polarized optical micrographs are shown that were taken from the 14 μm-deep microfluidic channels where the aqueous phases were composed of vesicles formed by (a) 0.5 μM Egg SM: 300 μM DTAB, and (b) 0.5 μM DPPC: 15 μM DTAB. Each line of images was collected from locations 4 and 3 as indicated in the top title. Images collected from experiments with 300 μM DTAB

in the first line. Images collected from experiments 0.5 μM Egg SM: 300 μM DTAB and 0.5 μM DPPC: 15 μM DTAB were collected at the duration after aqueous phase flow was initiated, as indicated in the images. The white double-sided arrow shows the orientations of the analyzer and polarizers used in all of the images shown in the figure. The dashed lines in the images indicate the location of the horizontal soft interfaces. Scale bar: 100 μm, common for all images.

4.5 Influence of the Guest Molecules on the Fusion Characteristics of Lipid Vesicles to the Microfluidic Soft Interfaces

We investigated the role of guest molecules in the lipid vesicles by observing the response of the microfluidic LC-aqueous interfaces. Dodecyltrimethylammonium bromide (DTAB) is a surfactant known to lower the melting temperatures and increase the fluidity of the lipid bilayers.[18] Past studies showed that DTAB can be used to control the areal density of the interface covered by DLPC by changing the composition of their mixture.[36] We investigated the adsorption behavior of DLPC at the flowing 5CB–aqueous interface in the presence of 15 μM DTAB, as shown in **Figure 4.11a** (n = 3). We did control experiments to understand whether 15 μM DTAB causes a change in the orientation of the interface. Control experiments confirmed that 15 μM DTAB alone did not alter the planar anchoring of the 5CB interface upon contact (**Figure 4.11a-*i***) as observed in all locations of the channel and at 40 minutes. However, when 0.5 μM DLPC was mixed with 15 μM DTAB, and this mixture flowed through the channel, we observed accelerated lipid adsorption. Initially, there were no lipid domains at the interface. Then, lipid domains started to be observed not only at locations 4 and 3, but also at location 2 within 20 minutes. Interestingly, we observed the lipid domains at location 1, which was near the inlet of the channel, within 40 minutes. This fusion rate was significantly faster than the rate observed for DLPC vesicles in the absence of DTAB (**Figure 4.11a-*ii,*** n=3; compared with **Figure 4.6**). This result indicated a pronounced effect of DTAB on vesicle softening and fusion dynamics.

For a more detailed investigation, we increased the DTAB concentration to 150 μM, expecting a more pronounced effect of DTAB on vesicle softening. However, first, we checked the effect of only 150 μM at the interface. As seen in **Figure 4.12a**, 150 μM was not sufficient to change the orientation of the interface itself. Mixing 150 μM DTAB with 0.5 μM DLPC resulted in a nearly full coverage of the interface. As seen in **Figure 4.12b**, softened vesicles were able to adsorb into the interface even at time zero. Interface reached full coverage immediately. We extended these experiments to Egg SM and DPPC vesicles, which are in the gel phase at room temperature and exhibited significantly slower adsorption kinetics than DLPC. Upon mixing 300 μM DTAB and 15 μM DTAB with Egg SM and DPPC, respectively, we observed strongly enhanced adsorption as evidenced by increased lipid coverage and transition to homeotropic anchoring at the interface (**Figure 4.10**). This behavior was similar to the softening effect on DLPC.

Figure 4.11.Adsorption of the lipids from softened and stiffened phospholipid vesicles to the flowing LC-aqueous interface. The polarized optical micrographs are shown that were taken from the 14 μm-deep microfluidic channels where the aqueous phases were composed of vesicles formed by (a) 0.5 μM DLPC and 15 μM DTAB, and (b) 0.5 μM DLPC and 0.5 μM C16-ceramide. Each line of images was collected from locations 1 to 4 as indicated in the top title. Images collected from experiments with (i) 15 μM DTAB and (ii) 0.5 μM C16-ceramide only vesicles are shown in the first row. Images collected from experiments with 0.5 μM DLPC:15 μM DTAB and 0.5 μM DLPC: 0.5 μM C16-ceramide were collected at the duration after aqueous phase flow was initiated, as indicated in the images. The white double-sided arrows show the orientations of the analyzer and polarizers used in all of the images shown in the figure. The dashed lines in the images indicate the location of the horizontal soft interfaces. Scale bar: 100 μm, common for all images.

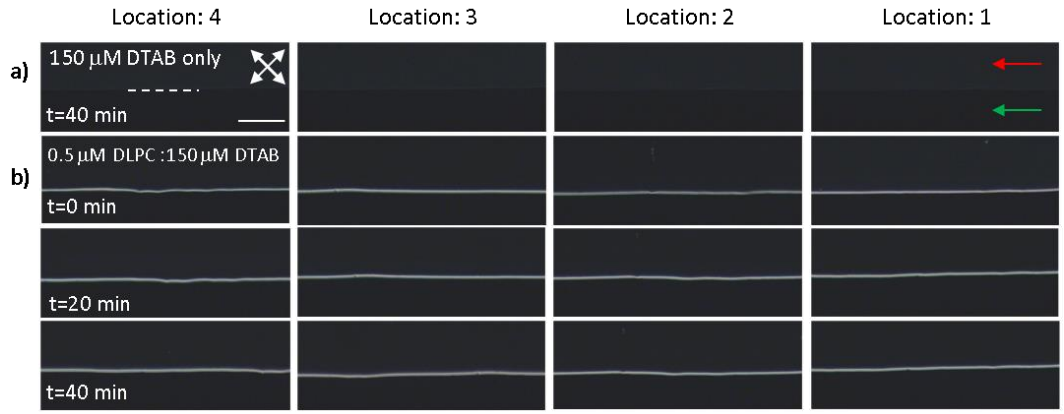

Figure 4.12.Adsorption of DLPC: DTAB mixture into the 5CB-aqueous interface. The polarized optical micrographs are shown that were taken from the 14 μm-deep microfluidic channels where the aqueous phases were composed of (a) 150 μM DTAB, and (b) 0.5 μM DLPC: 150 μM DTAB. Each line of images was collected from locations 1-4 as indicated in the top title. Images were collected at a duration after aqueous phase flow was initiated, as indicated in the images. The white double-sided arrow shows the orientations of the analyzer and polarizers used in all of the images shown in the figure. The dashed lines in the images indicate the location of the horizontal soft interfaces. Scale bar: 100 μm, common for all images.

Ceramides are characterized by high melting temperatures ($T_m \approx 90$ °C) and form bilayers with solid-like mechanical behavior. Their monolayers exhibit viscoelastic behavior with a high shear modulus ranging from 30-100 mN/m and a high yield stress (100 mN/m).[57] Moreover, ceramides impose a condensing effect on bilayers such that they cause an increase in compression modulus of Egg SM monolayers.[57] To understand the rigidifying effect of ceramide[55] on DLPC, we mixed 0.5 μM DLPC with 0.5 μM C16-ceramide. We first confirmed that 0.5 μM C16-ceramide did not cause any anchoring transition at the interface **Figure 4.11b-*i***. We observed that fusion of vesicles to the interface did not occur with the mixtures of 0.5 μM DLPC with 0.5 μM C16-ceramide, even at the end of 40 min, as shown in **Figure 4.11b-*ii***. (n=3). This showed that ceramide made the DLPC bilayers stiffer and made the adsorption unfavorable. To further analyze, we decreased the C16-

ceramide amount to 0.16 μM. As seen in polarized optical micrographs in **Figure 4.13a** (n=3), 0.16 μM was not able to fuse into the interface, similar to 0.5 μM, as understood from no change in the orientation of LC mesogens at the interface. The mixture of DLPC with 0.16 μM C16-ceramide caused an increase in the fractional coverage **Figure 4.13b,** when compared with **Figure 4.11b-*ii***. The fractional coverage was observed at locations 4 and 3 within 40 minutes, as evident in polarized optical micrographs. DLPC vesicles with 0.16 μM C16-ceramide exhibited slower adsorption kinetics compared to vesicles of only DLPC **Figure 4.6**, by intercepting from both the temporal profile and the difference in interfacial lipid coverage. We can conclude that the elastic properties of the bilayers strongly affect the fusion rates of the bilayers, which also changes the response of the interface.

Figure 4.13. Adsorption of DLPC: C16-ceramide mixture into the 5CB-aqueous interface. The polarized optical micrographs are shown that were taken from the 14 μm-deep microfluidic channels where the aqueous phases were composed of (a) 0.16 μM C16-ceramide, and (b) 0.5 μM DLPC:0.16 μM C16-ceramide. Each line of images was collected from locations 1-4 as indicated in the top title. Images were collected at a duration after aqueous phase flow was initiated, as indicated in the images. The white double-sided arrow shows the orientations of the analyzer and polarizers used in all of the images shown in the figure. The dashed lines in the images indicate the location of the horizontal soft interfaces. Scale bar: 100 μm.

4.6 Influence of Cholesterol on the Fusion Characteristics of Lipid Vesicles to the Microfluidic Soft Interfaces

Cholesterol is a common guest molecule in the cell membranes. Its excess amount may cause some disruptions of the cell membranes, and therefore, it is important to track and determine the cholesterol in membranes in order to diagnose the diseases. When cholesterol is mixed with phospholipids, it changes the mechanical properties of the cell. Using the flowing LC-aqueous interfaced microfluidic platform, we sought to investigate the fusion characteristics of the cholesterol-hosted lipid vesicles, as the literature shows its non-universal effect on the elasticity of the host lipid vesicles and its importance in maintaining the structure and function of mammalian cell membranes.[13] We first made observations using vesicles of DLPC doped with cholesterol. We note that the cholesterol did not cause an ordering transition at the interfaces of the LCs, confirmed by the experiments with the microfluidic channels by using 1.5 μM cholesterol as the aqueous phase (**Figure 4.14**). As observed in the polarized optical micrographs, cholesterol did not change the orientation of the interface within 40 minutes. Also, cholesterol did not change the orientation of the curved interfaces in droplet systems, as evident by the bipolar configuration (**Figure 4.15c**).

Figure 4.14.5CB-aqueous phase interface when cholesterol flows as aqueous phase. The polarized optical micrographs are shown that were taken from the 14 μm-deep microfluidic channels, where the aqueous phases were composed of 1.5

μM cholesterol. Each line of images was collected from locations 1-4 as indicated in the top title. Images were collected at a duration after aqueous phase flow was initiated, as indicated in the images. The white double-sided arrow shows the orientations of the analyzer and polarizers used in all of the images shown in the figure. The dashed lines in the images indicate the location of the horizontal soft interfaces. Scale bar: 100 μm.

Figure 4.15a shows the polarized optical micrographs collected after 40 minutes of contact of the interface with the 0.5 μM DLPC vesicle suspensions with and without cholesterol (see **Appendix D.1** for more detailed data). To compare the fusion rates, we quantified the fractional coverage of the microfluidic 5CB-aqueous interfaces with these mixtures at t = 40 min, where we observed a 94% ± 8% (n = 7) coverage with DLPC vesicles with no doped cholesterol. With the introduction of cholesterol to the DLPC vesicles, we observed a decreasing fractional coverage at the LC-aqueous interface, such that 74%±4.5% coverage for 25% cholesterol, as quantified in **Figure 4.15b**. When the cholesterol content was increased to 50%, we observed no evidence of the adsorbed DLPC at the LC-aqueous interfaces (n=9). Above this concentration of cholesterol, addition of cholesterol to the solution resulted in an increasing fractional coverage, reaching 73% ± 28%, 98% ± 3% and 99% ± 0.9% for 60%, 66% and 75% cholesterol content in 0.5 μM DLPC vesicle suspensions, respectively (**Figure 4.15b** and **Appendix D.3a** for temporal data). A similar trend was also observed in the droplets (**Figure 4.15c**). For the droplet systems, 1 μL of 5CB was emulsified in 0.5 μM DLPC and the desired amount of cholesterol. In the case of only 0.5 μM DLPC, radial configuration was observed in 77% ± 3% of the droplets. This percentage decreased to 32% ± 4% upon the addition of 25% cholesterol. The lowest occurrence of radial configuration, 22% ± 2%, was observed with 50% cholesterol, which then increased to 51% ± 8% at 75% cholesterol. These configurations of droplets were consistent with a microfluidic channel in a manner that coverage decreased with cholesterol introduction and then increased beyond a threshold.

The results presented in **Figure 4.15a, b** indicated two major outcomes. First, the mixtures of cholesterol and DLPC caused planar to homeotropic transitions in LCs at aqueous interfaces. Second, combining our observations of the non-monotonous change of the interfacial coverage with the cholesterol concentrations and the influence of the vesicle elasticity on the adsorption characteristics of lipids to the LC-aqueous interfaces explained above, we reasoned that the cholesterol concentration-dependent fusion characteristics of the DLPC vesicles occurred due to the changes in the elastic properties of the DLPC vesicles as a function of the cholesterol concentration. Introduction of cholesterol is known to perturb the lipid bilayer, resulting in changes in the packing of lipids in the bilayer.[78] These changes are highly controversial, as discussed with a range of techniques used in the measurements of the vesicle rigidity.[63,79] The effect of the cholesterol was found to be dependent significantly on the chemical structure of the phospholipids, and in most of the studies was explained by the saturation of the alkyl chain groups.[13,20,21] Considering the presence of the saturated acyl chains of DLPC, it can be expected to undergo an increase in bending rigidity with the cholesterol content.[13] To understand the effect of cholesterol on DLPC molecules, we measured the diffusion coefficients of DLPC vesicles with increasing cholesterol amount in the solution by using dynamic light scattering (**Appendix D.2**). We found that there is a negligible change in the diffusion coefficient with increasing cholesterol amount, which suggests the difference in the fusion kinetics of DLPC vesicles with cholesterol is only related to the changing rigidity of the vesicles. Also, we calculated Peclet numbers for all cholesterol ratios as higher than 2500, providing further evidence that kinetics is related to rigidity. Thus, we concluded that the rigidity of DLPC vesicles increased as the cholesterol content was increased up to 50% based on the adsorption rate we observed. Above this cholesterol loading, vesicles softened that resulting in an enhanced fusion rate. These results were consistent with the literature data[13] obtained via NMR measurements, which indicates rigidity increases with cholesterol for saturated lipids, but contradicted data using micropipette aspiration.[80]

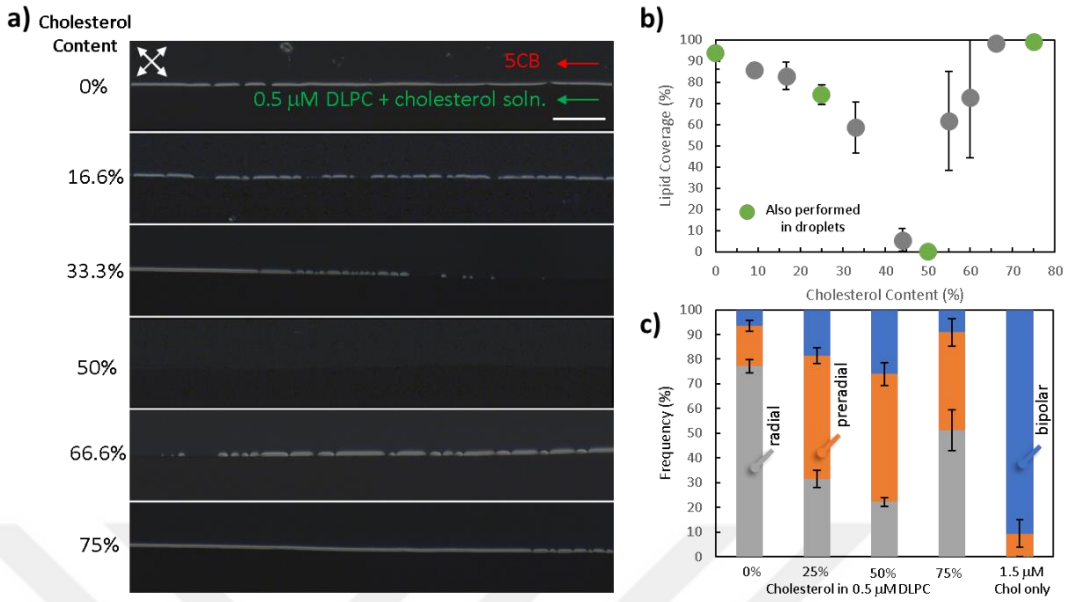

Figure 4.15.Adsorption of lipids from DLPC-Cholesterol mixtures to microfluidic LC-aqueous interface. (a) Polarized optical micrographs collected from experiments with contacting 5CB with a constant 0.5 µM DLPC concentration and varying concentrations of cholesterol from 0 to 1.5 µM. Images are shown at t 40 min and at location 4 of the channel. Flow was assisted with inlet pressures of P_{LC} = 15 mbar, $P_{Aq.}$ = 5 mbar. The images were collected under crossed polarizer and analyzer at 45°- 135° as indicated by the two double-sided arrows. Scale bar: 100µm. (b) Plot of lipid coverage (%) vs cholesterol content (%) determined from the polarized optical micrographs (n=9). (c) Droplet configuration frequencies with the aqueous phase consisting of a constant 0.5 µM DLPC concentration and varying concentrations of cholesterol from 0 to 1.5 µM (n=3).

Our observations support the non-universal impact of cholesterol on phospholipid bilayers, given the literature, showing that the LC-aqueous interfaced microfluidics system is sensitive to the changes in chain saturation. However, the lack of literature data is that measurements were completed until 50% cholesterol content, which avoids the effect of the cholesterol-rich phase of lipid vesicles. Our results can be related to the umbrella model and the condensing effect of

cholesterol[81,82] on phospholipids, especially after 50% cholesterol is added to the vesicles. In this model, cholesterol perturbs the bilayer[78], and since it has a small hydrophilic head group when compared with the phospholipid molecules, the phospholipid head groups protect cholesterol from the water outside of the bilayer. With increasing cholesterol amounts in the bilayer, cholesterol-cholesterol interactions become unfavorable. After a critical point, cholesterol is not able to interact with phospholipids. In our results, this critical point was 50 mol% cholesterol amounts, which was observed to be the most rigid composition. Since vesicles are highly rigid in this state, they were not able to fuse into monolayers, as indicated by no visible alignment change of LC mesogens at the interface. After exceeding this point, cholesterol molecules would not be able to interact with phospholipids. Since vesicles were not rigidified with cholesterol anymore, vesicles were softer than in this state. In our experiments, we observed this effect via a sudden increase in the fractional coverage of the interface with lipids, 61.6% ± 23% from 0%, after 50% cholesterol.

The fusion kinetics of the vesicles formed by cholesterol and lipid mixtures were further investigated by using vesicle suspensions of DOPC, DPPC, and Egg SM in our systems (**Figure 4.16** and **Appendix D.3b-d** for more details). The same procedures applied to these lipids as in DLPC and similar to the previously explained experimental results, the evidence of the initial adsorption of lipid-cholesterol mixtures to the interface was first observed towards the end of the channels (location 4) as shown in (**Figure 4.17,18** and **20)**.

As shown in **Figure 4.16a**, we observed a monotonously decreasing fractional coverage trend with the increase in the cholesterol content in DPPC vesicles (n=4). We collected the images at location 4 and after 40 minutes of contacting the lipid and cholesterol mixture (**Figure 4.16a and Appendix D.3c** for spatiotemporal data). Interfacial lipid coverage of the interface decreased from 92.4% ± 11.7% to 53.1% ± 19.9%, 34.4% ± 11.1%, and 2.5% for 25%,50%, and 75% cholesterol in 0.5 μM of DPPC, respectively. As given in **Figure 4.17**, pure DPPC exhibited high fractional coverage for all locations of the interface when they

fused within 40 minutes. Upon introduction of the cholesterol in the solution, fractional coverage decreased, and even zero coverage was observed in locations 1 and 2. For the highest cholesterol amount, fractional coverage was only observed at location 4. All these spatial data were consistent with the fusion kinetics of DLPC, as mentioned earlier in this thesis. When the droplet response experiments were performed with 5CB droplets (vortexed), we also observed a significant decrease from 80.7% ± 4.4% for 0% cholesterol to 1.4% ± 1.4% for 75% cholesterol in the radial configuration, monotonously. When compared with the results presented in **Figure 4.9**, which indicated a finite rigidity of the DPPC vesicles as the adsorption was enhanced significantly with the application of shear, the experiments performed in flowing interfaces indicated a significant increase in the rigidity of the DPPC vesicles with the addition of cholesterol. As shown in **Appendix D.2**, the diffusion coefficients of the DPPC vesicles were not influenced significantly or monotonously with the addition of cholesterol. Also, we calculated the Peclet numbers by using measured diffusion coefficients, and we found that for each cholesterol ratio, it is higher than 2500. Thus, we reasoned that the reduction in the interfacial cholesterol content led to an increase in the rigidity of the vesicles with the addition of cholesterol. This rigidifying effect has been discussed in the literature for DPPC by analyzing interfacial behavior using Langmuir balance techniques, and it is found that DPPC shifts to a lower value of area/molecule monotonously within a range of 0.1 to 0.75 cholesterol fraction due to the condensing effect of cholesterol.[83] Due to its nature, DPPC was hypothesized to act as an "umbrella" strongly with increasing cholesterol perturbation, and thus, we observed a decreasing fractional coverage with increasing cholesterol content in the solution. In the literature, it is shown that cholesterol forms condensed complexes with DPPC and increases the area per lipid of DPPC bilayers when even used in 10-20% mol of cholesterol, indicating higher rigidity and orientational order.[84]

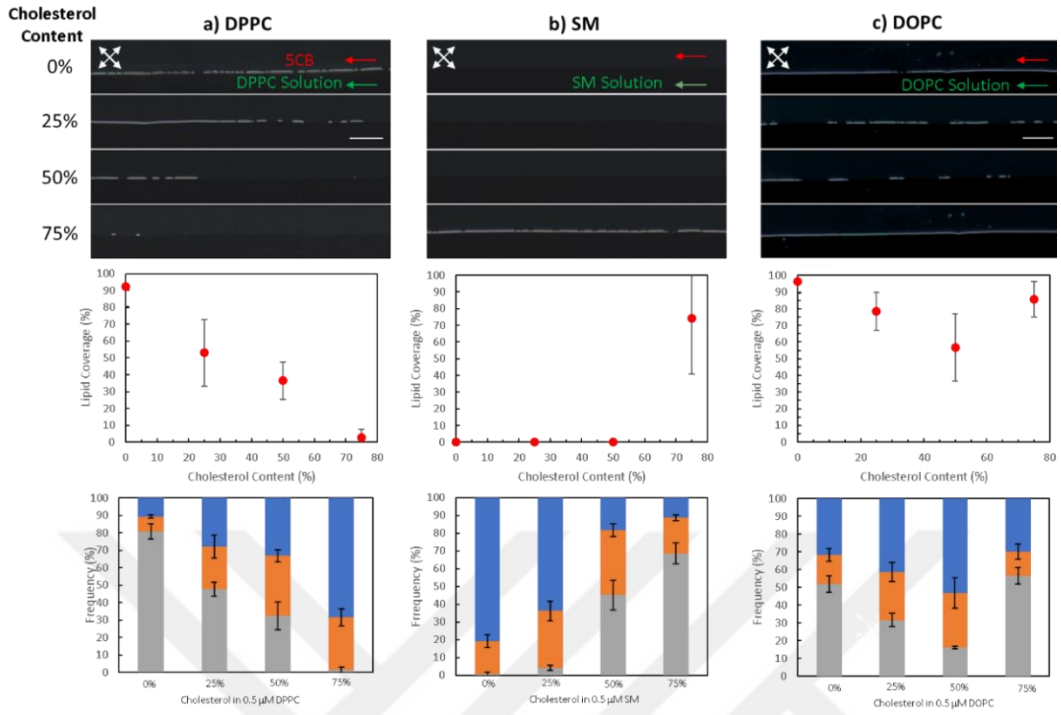

Figure 4.16.Response of the LC-aqueous interfaces upon adsorption of DOPC, DPPC, and Egg SM from their vesicles with cholesterol as the guest molecule. The polarized optical micrographs collected at t= 40 min and at location 4 are shown in the top panel for the cases where the aqueous phase consists of constant concentrations (0.5 μM) of (a) DOPC, (b) Egg SM, and (c) DPPC, and varying concentrations of cholesterol from 0 to 1.5 μM as indicated. Polarized images were collected under crossed polarizer and analyzer at 45°- 135°, respectively. Flow was assisted with inlet pressures of P_{LC}= 15 mbar and $P_{Aq.}$ = 5 mbar. Middle panels in figure show the plot of lipid coverage density vs cholesterol content and the bottom panel shows the configuration frequency (%) of the experiments performed with the droplets incubated in the same concentrations of the lipids and cholesterol. Flow systems: n=4 for DOPC and DPPC; n=5 for Egg SM. For droplet systems: n=3 for each plot. Scale bars are 100 μm, common for all images.

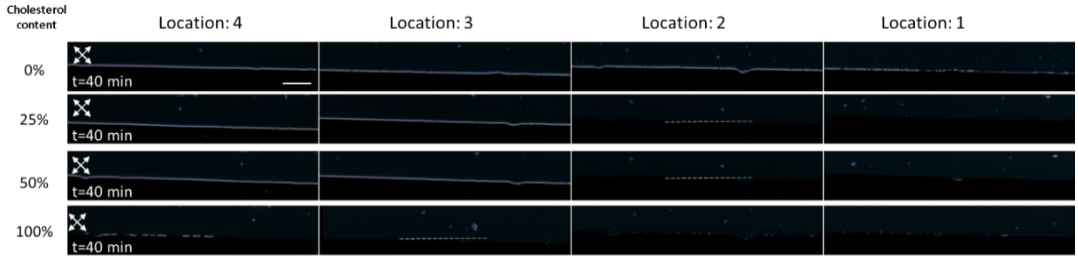

Figure 4.17. **Interfacial coverages of cholesterol dissolved DPPC complexes.** The polarized optical micrographs shown were taken from the 14 μm-deep microfluidic channels, where the aqueous phases were composed of 0.5 μM DPPC and varying cholesterol content from 0% to 75%. Every image was collected at t=40 min. The white double-sided arrow shows the orientations of the analyzer and polarizers used in all of the images shown in the figure. The dashed lines in the images indicate the location of the horizontal soft interfaces. Scale bar: 100 μm.

Egg SM was the most rigid lipid used in our study and showed no evidence of adsorption to the LC-aqueous interface, either in droplets of microchannels (**Figure 4.9**). When doped with cholesterol, we did not observe any increase in fractional coverage with the cholesterol amount until 75% cholesterol in microchannels, as shown in (n=4), (**Figure 4.16b**). At 75% cholesterol, fractional coverage was increased to 74.4% ± 34.4% fractional coverage of the interface, suddenly. For the Egg SM, we obtained a negligible change in diffusion coefficients with cholesterol (**Appendix D.2**), and Peclet numbers calculated higher than 2500 for all ratios. These observations and measurements supported the softening of the Egg SM vesicles with the addition of cholesterol content, which is consistent with past studies that reported a decrease in the rigidity of the bilayers of Egg SM with the addition of cholesterol using techniques including flicker spectroscopy and electrodeformation.[20] **Figure 4.18** shows the fractional coverages of four different locations for all cholesterol amounts. For the 75% cholesterol, fractional coverage of the interface was observed at locations 2, 3, and 4, while for 0%, 25%, and 50% cholesterol, there were no lipid domains at all locations. In droplet systems, the trend was the same with 4% ± 1.4%, 45.2% ± 8.3%, and 68.6% ± 6% for 25%, 50%, and

75% cholesterol, respectively, indicating the decreasing rigidity of Egg SM vesicles with cholesterol. However, radial configuration was observed at 25% and 50% cholesterol in 0.5 μM Egg SM, indicating the adsorption, unlike in microchannels as shown in **Figure 4.16b** (n=4). This result led us to hypothesize that the observed adsorption of Egg SM in the droplet system was due to enhanced shear caused by vortex mixing. To check this effect, we conducted droplet experiments of 50% cholesterol in 0.5 μM Egg SM by gentle handshake and did not observe any significant radial configuration (**Figure 4.19a**). When compared with the vortexed experiments, a significant reduction of radial configuration was observed from 54% ± 8.3% to 1.6%, indicating a similar effect of shear with DPPC. Also, by increasing aqueous phase inlet pressure, and thus velocity, these vesicles were able to fuse into the LC-aqueous interface in microchannels (**Figure 4.19b**). Fractional coverage was observed when the inlet pressure increased to 25 mbar at location 4, while it was still not possible to observe lipid domains at location 3. This showed that 50% cholesterol exhibited a softening effect on vesicles enough to fuse with shear but not enough to observe them at location 3. It is also important to emphasize that the responses measured in the microchannels were more evident than in the droplet experiments, evidencing the influence of the finite rigidity of the cholesterol-doped Egg SM vesicles.

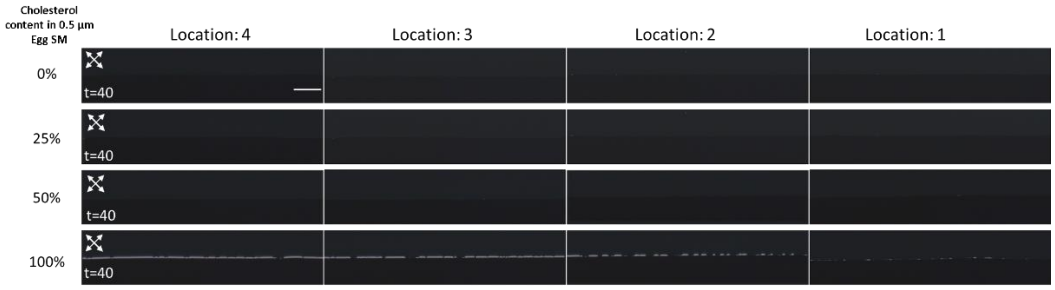

Figure 4.18.**Interfacial coverages of cholesterol dissolved Egg SM complexes.** The polarized optical micrographs shown were taken from the 14 μm-deep microfluidic channels, where the aqueous phases were composed of 0.5 μM Egg SM and varying cholesterol content from 0% to 75%. Every image was collected at t=40 min. The white double-sided arrow shows the orientations of the analyzer and

polarizers used in all of the images shown in the figure. The dashed lines in the images indicate the location of the horizontal soft interfaces. Scale bar: 100 μm.

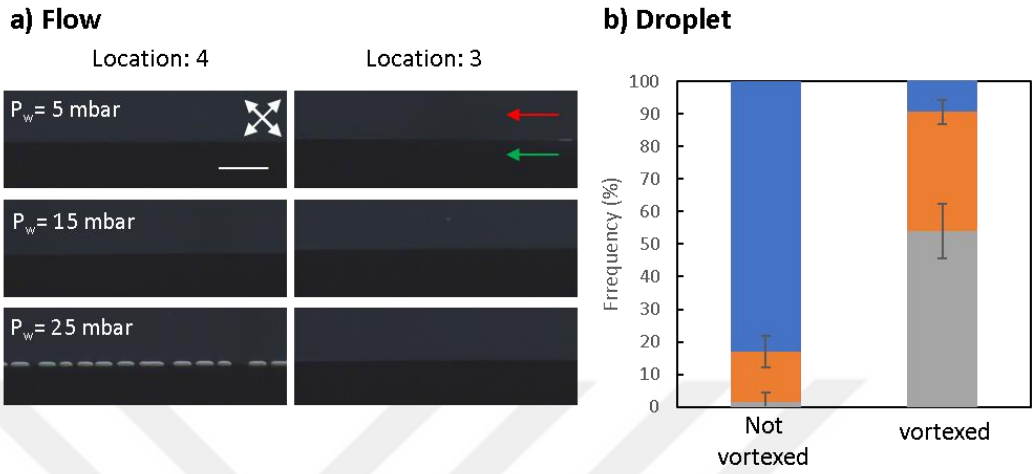

Figure 4.19. Effect of 50% cholesterol on Egg SM vesicles. (a) Droplet configuration distributions for emulsions equilibrated with 50% cholesterol in 0.5 μM SM, as not vortexed and vortexed. (b) The polarized optical micrographs shown were taken from the 14 μm-deep microfluidic channels, where the aqueous phases were composed of 50% cholesterol in 0.5 μM SM. Images were collected at t=40 minutes, and at locations 4 and 3, as indicated in the top title. Images collected from the experiments flow were assisted by P_{LC} = 15 mbar: $P_{Aq.}$ = 5 mbar, $P_{Aq.}$ = 15 mbar, $P_{Aq.}$ = 25 mbar, as indicated in the images. The white double-sided arrow shows the orientations of the analyzer and polarizers used in all of the images shown in the figure. The dashed lines in the images indicate the location of the horizontal soft interfaces. Scale bar: 100 μm.

The same experiments were conducted for the same ratios of cholesterol in both microfluidic and droplet systems for DOPC. DOPC is a synthetic lipid that exhibits liquid-like behavior and consists of two unsaturated chains. DOPC showed a similar non-monotonous fractional coverage trend with DLPC, but with higher fractional coverage in both microchannels and droplet systems (**Figure 4.16c**). As seen in both polarized optical micrographs collected from location 4 and 40 minutes

and the interfacial lipid coverage plot, pure DOPC covered the flowing interface in 96.3% ± 7.1%. However, upon introduction of cholesterol, fractional coverage decreased to 78.5% ± 11.4%, 56.7% ± 20.1% for 25% and 50%, respectively. Similar to DLPC, fractional coverage was the lowest at 50% cholesterol; fractional coverage was increased to 85.8% ± 10.6% within 75% cholesterol. This result showed that the rigidity of DOPC increases with cholesterol up to a critical value, then an excess amount of it displays a softening effect similar to DLPC.

This higher fractional coverage can be explained by the higher fluidity of the DOPC (n=4) when compared with DLPC.[72] **Figure 4.20** shows the spatial data of DOPC adsorption. Consistent with previous experiments, softer vesicles were able to fuse through the inlet of the channel, while more rigid vesicles only fused to the end of the channel. For the DOPC, we also obtained a negligible change in diffusion coefficients with cholesterol (**Appendix D.2**), and Peclet numbers calculated higher than 2500 within the range of cholesterol amounts studied. This showed that cholesterol did not change the diffusivity; it only imposed an effect on the fusion kinetics of vesicles to the 5CB-aqueous interface.

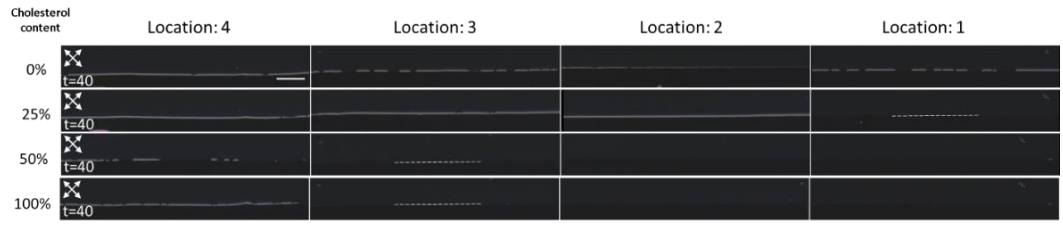

Figure 4.20. Interfacial coverages of cholesterol dissolved DOPC complexes. The polarized optical micrographs shown were taken from the 14 μm-deep microfluidic channels, where the aqueous phases were composed of 0.5 μM DOPC and varying cholesterol content from 0% to 75%. Every image was collected at t=40 min. The white double-sided arrow shows the orientations of the analyzer and polarizers used in all of the images shown in the figure. The dashed lines in the images indicate the location of the horizontal soft interfaces. Scale bar: 100 μm.

Fusion kinetics of complex lipids and cholesterol were also analyzed in stagnant systems, using TEM grids supported on DMOAP-coated glass. The trend of the adsorption of lipid vesicles and their mixtures with cholesterol was the same for all types of lipids in the stagnant systems, but significantly longer than in flow and droplet systems (**Figure 4.21**). For instance, the response time of the stagnant systems for the fusion of Egg SM vesicles to the interface was 24 hours for 0%, 25%, and 50% cholesterol amount, consistent with the trend of microfluidics and droplet systems. This increase in the response time for stagnant systems was expected due to a lack of shear.

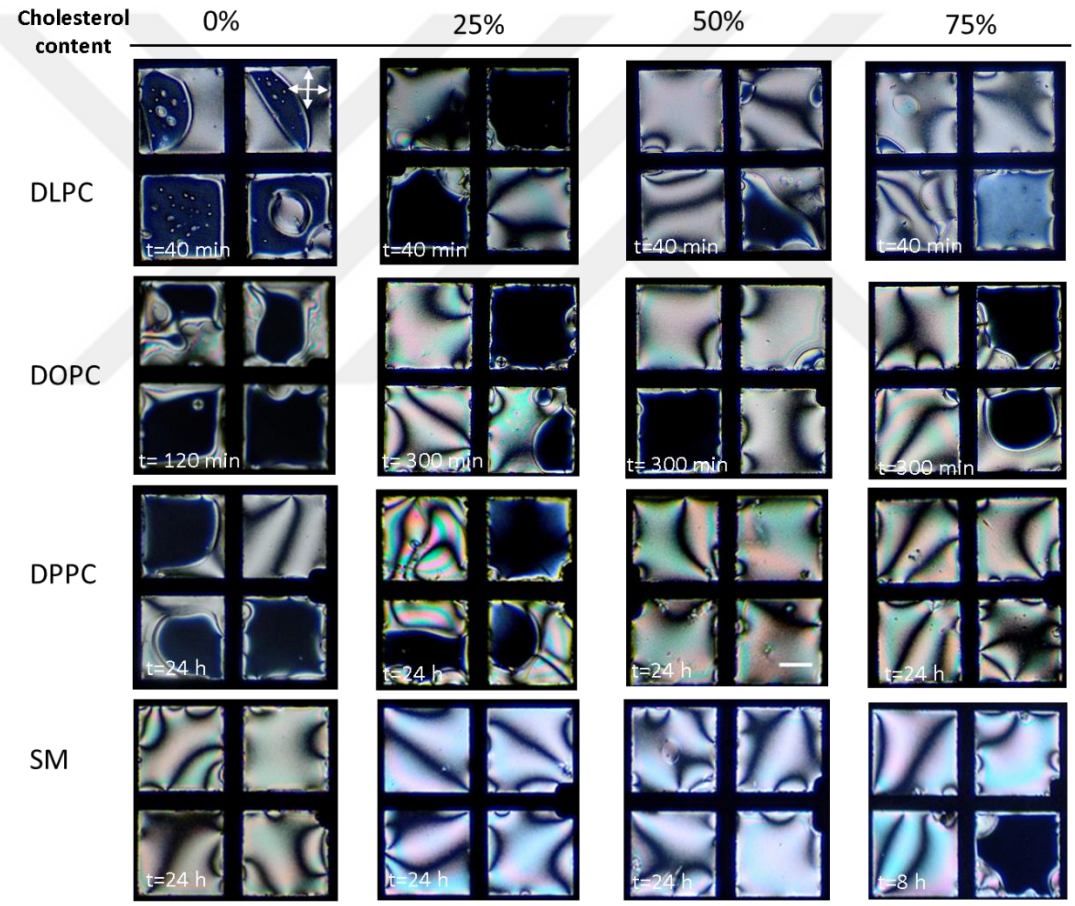

Figure 4.21. **Stagnant systems consisting of cholesterol-dissolved lipid complexes as aqueous phases**. Polarized optical micrographs are collected under crossed polarizers and analyzer 0°- 90° for stagnant systems composed of an aqueous phase of 5.0 μM DLPC, DOPC, DPPC, and Egg SM, and varying cholesterol content

from 0% to 75%. The white double-sided arrow shows the orientations of the analyzer and polarizers used in all of the images shown in the figure. Images collected during the duration after the aqueous phase was exchanged, as indicated in the images. Scale bar: 100 μm.

CHAPTER 5

CONCLUSION

We conducted a comprehensive investigation of the fusion characteristics of various biologically relevant synthetic lipids (DLPC, DPPC, DOPC) and biologically-driven lipids (Egg SM) at liquid crystal (LC)–aqueous interfaces, with a focus on how changes in lipid mechanical properties influence their fusion kinetics. We successfully established a continuous and responsive platform to provide complementary insights into lipid organization using microfluidic channels with stagnant and LC-in-water emulsion systems. In the microfluidic system, we fabricated 14 μm depth channels, providing a stable co-flow of 5CB and an aqueous phase and creating a continuous LC-aqueous interface. Due to the unique properties of 5CB and the dynamic interface with the aqueous phase, this system enabled real-time observation of lipid adsorption. The findings of this study revealed that flow conditions enhance the adsorption of the phospholipids from the dispersion into the interface with a preferential distribution along the interface. We also revealed that different phospholipids exhibited different fusion kinetics, such that DLPC and DOPC demonstrated similar fusion kinetics, while Egg SM vesicles were not able to fuse into the interface due to their rigid nature. Interestingly, DPPC, which is a rigid lipid due to its gel phase, was able to adsorb into the interface since its fusion to interface was shear-induced, as shown by vortexed and non-vortexed droplet experiments.

We found that monitoring the rigidity of the lipid vesicles by using surfactants and ceramides resulted in significant changes in their fusion kinetics at the interface. By forming a mixed micelle solution by mixing the lipids (DLPC, DPPC, and Egg SM) with DTAB, we showed that interfacial coverage of the interface was increased, as evidenced by the polarized optical micrographs, when compared to those of the pure lipids in microfluidic channels, indicating a softening

effect even for Egg SM. Moreover, we analyzed the adsorption kinetics of lipids doped with ceramide, which is known for making lipids more rigid.[19] We showed that when DLPC was mixed with C16-ceramide, vesicles did not fuse into the interface, indicating the formation of highly rigid vesicles with C16-ceramide. We also found that the influence of cholesterol was found to be non-universal and lipid-specific. For DLPC and DOPC, cholesterol increased membrane rigidity up to ~50 mol% while DPPC, a lipid in the gel phase at room temperature, exhibited a more gradual, monotonic increase in rigidity with cholesterol content. In contrast, Egg SM showed an opposite trend, where cholesterol resulted in a decreased rigidity beyond a threshold which is 75% cholesterol. However, for the 50% cholesterol in Egg SM, vesicles exhibited shear-induced fusion kinetics, indicating a softening effect with shear similar to DPPC itself. The observed adsorption trend aligned with the umbrella model and condensing effect on cholesterol in the lipid bilayers.[82]

The findings of this study provide new insights into changing membrane mechanics with changing compositions of guest molecules in the cell membranes. By combining the recent advances in the literature.[26,27] we demonstrated that flowing LC-aqueous interfaces provide highly sensitive platforms for detecting changes in the properties of the lipid vesicles. In the platform we developed in this study, we show that it is possible to interpret the changes in the mechanical properties of the lipid vesicles via monitoring the interfacial coverage of the interface caused by the lipid vesicle fusion to the interface, continuously. This microfluidic approach highlights the potential of LC-based systems as label-free and real-time tools for characterizing biologically relevant and biologically driven lipid bilayers, particularly in dynamic environments and mimicking the physiological conditions of membranes. Due to the responsiveness and sensitivity of our system, it can be designated as a promising analytical platform for probing membrane rigidity changes related to diseases, where they are critical indicators of diseases such as cancer and neurodegenerative disorders.

The results of this study are also encouraging in light of future applications. Considering the biological relevance of the used lipid vesicles and their complexes

formed with the guest molecules, and even combinations with proteins (mimicking lipid rafts), integrating this platform with advanced techniques may enhance the study of membrane mechanisms and their role in disease progression. The quantification of mechanical properties of membranes, especially bending rigidity, can be recognized as experimentally challenging due to the sensitivity of lipids and methodological limitations[79], our system provides the potential to overcome these challenges by offering insights about the fusion characteristics of vesicles into a soft flowing interface combined with interfacial analysis. Potential technologies derived based on the demonstrations we show in this study may act as a transformative path towards point-of-care or marker-based diagnostic systems for critical or rare diseases. Another potential direction of future applications can be the design of responsive drug delivery systems. Vesicle fusions to the interface could provide mechanical insights for target tissues[85], and understanding the shear-induced lipid vesicle fusion to the interface could provide the tuning of the release of drugs in mechanically changing environments such as cancer cells and inflamed tissues.[86] In particular, extracellular vesicles have already been used in cancer-related clinical studies as biocargos and biomarkers[45], and their integration with microfluidic technologies enabled the high-throughput and minimally invasive diagnostics.[52] Our system contributes to a platform that can be translated to extracellular research and further enhances detection sensitivity.

REFERENCES

(1) Iwasa, Janet.; Marshall, W. F.; Karp, Gerald. *Karp's Cell and Molecular Biology : Concepts and Experiments*; Wiley, 2020.

(2) Dias, C.; Nylandsted, J. Plasma Membrane Integrity in Health and Disease: Significance and Therapeutic Potential. *Cell Discov* **2021**, *7* (1), 1–18. https://doi.org/10.1038/s41421-020-00233-2.

(3) Faizi, H. A.; Frey, S. L.; Steinkühler, J.; Dimova, R.; Vlahovska, P. M. Bending Rigidity of Charged Lipid Bilayer Membranes. *Soft Matter* **2019**, *15* (29), 6006–6013. https://doi.org/10.1039/c9sm00772e.

(4) Tsuchiya, H.; Nagayama, M.; Tanaka, T.; Furusawa, M.; Kashimata, M.; Takeuchi, H. Membrane-Rigidifying Effects of Anti-Cancer Dietary Factors. *BioFactors* **2002**, *16* (3–4), 45–56. https://doi.org/10.1002/biof.5520160301.

(5) D'auria, L.; Reiter, C.; Ward, E.; Moyano, A. L.; Marshall, M. S.; Nguyen, D.; Scesa, G.; Hauck, Z.; Van Breemen, R.; Givogri, M. I.; Bongarzone, E. R. Psychosine Enhances the Shedding of Membrane Microvesicles: Implications in Demyelination in Krabbe's Disease. *PLoS One* **2017**, *12* (5), 1–19. https://doi.org/10.1371/journal.pone.0178103.

(6) Kwon, S.; Yang, W.; Moon, D.; Kim, K. S. Comparison of Cancer Cell Elasticity by Cell Type. *J Cancer* **2020**, *11* (18), 5403–5412. https://doi.org/10.7150/jca.45897.

(7) Kashani, A. S.; Packirisamy, M. Cancer Cells Optimize Elasticity for Efficient Migration: Migratory Index. *Royal Society* **2020**, *7* (10), 1–16. https://doi.org/10.1098/rsos.200747.

(8) Hayashi, K.; Iwata, M. Stiffness of Cancer Cells Measured with an AFM Indentation Method. *J Mech Behav Biomed Mater* **2015**, *49*, 105–111. https://doi.org/10.1016/j.jmbbm.2015.04.030.

(9) Crane, J. M.; Tamm, L. K. Role of Cholesterol in the Formation and Nature of Lipid Rafts in Planar and Spherical Model Membranes. *Biophys J* **2004**, *86* (5), 2965–2979.

(10) Goñi, F. M.; Alonso, A. Effects of Ceramide and Other Simple Sphingolipids on Membrane Lateral Structure. *Biochim Biophys Acta Biomembr* **2009**, *1788* (1), 169–177. https://doi.org/10.1016/j.bbamem.2008.09.002.

(11) Jones, M. N. Surfactant Interactions with Biomembranes and Proteins. *Chem Soc Rev* **1992**, *21* (2), 127–136. https://doi.org/10.1039/CS9922100127.

(12) Song, Y.; Liu, J.; Zhao, K.; Gao, L.; Zhao, J. Cholesterol-Induced Toxicity: An Integrated View of the Role of Cholesterol in Multiple Diseases. *Cell Metab* **2021**, *33* (10), 1911–1925. https://doi.org/10.1016/j.cmet.2021.09.001.

(13) Pan, J.; Mills, T. T.; Tristram-Nagle, S.; Nagle, J. F. Cholesterol Perturbs Lipid Bilayers Nonuniversally. *Phys Rev Lett* **2008**, *100* (19), 1–4. https://doi.org/10.1103/PhysRevLett.100.198103.

(14) Emanuelsson, F.; Nordestgaard, B. G.; Benn, M. Familial Hypercholesterolemia and Risk of Peripheral Arterial Disease and Chronic Kidney Disease. *Journal of Clinical Endocrinology and Metabolism* **2018**, *103* (12), 4491–4500. https://doi.org/10.1210/jc.2018-01058.

(15) Zambón, D.; Quintana, M.; Mata, P.; Alonso, R.; Benavent, J.; Cruz-Sánchez, F.; Gich, J.; Pocoví, M.; Civeira, F.; Capurro, S.; Bachman, D.; Sambamurti, K.; Nicholas, J.; Pappolla, M. A. Higher Incidence of

Mild Cognitive Impairment in Familial Hypercholesterolemia. *American Journal of Medicine* **2010**, *123* (3), 267–274. https://doi.org/10.1016/j.amjmed.2009.08.015.

(16) Gamerdinger, M.; Clement, A. B.; Behl, C. Cholesterol-like Effects of Selective Cyclooxygenase Inhibitors and Fibrates on Cellular Membranes and Amyloid-β Production. *Mol Pharmacol* **2007**, *72* (1), 141–151. https://doi.org/10.1124/mol.107.034009.

(17) Gan, L. T.; Van Rooyen, D. M.; Koina, M. E.; McCuskey, R. S.; Teoh, N. C.; Farrell, G. C. Hepatocyte Free Cholesterol Lipotoxicity Results from JNK1-Mediated Mitochondrial Injury and Is HMGB1 and TLR4-Dependent. *J Hepatol* **2014**, *61* (6), 1376–1384. https://doi.org/10.1016/j.jhep.2014.07.024.

(18) Heerklotz, H. Interactions of Surfactants with Lipid Membranes. *Q Rev Biophys* **2008**, *41* (3–4), 205–264. https://doi.org/10.1017/S0033583508004721.

(19) Silva, L.; De Almeida, R. F. M.; Fedorov, A.; Matos, A. P. A.; Prieto, M. Ceramide-Platform Formation and -Induced Biophysical Changes in a Fluid Phospholipid Membrane. *Mol Membr Biol* **2006**, *23* (2), 137–148. https://doi.org/10.1080/09687860500439474.

(20) Gracià, R. S.; Bezlyepkina, N.; Knorr, R. L.; Lipowsky, R.; Dimova, R. Effect of Cholesterol on the Rigidity of Saturated and Unsaturated Membranes: Fluctuation and Electrodeformation Analysis of Giant Vesicles. *Soft Matter* **2010**, *6* (7), 1472–1482. https://doi.org/10.1039/b920629a.

(21) Pan, J.; Tristram-Nagle, S.; Nagle, J. F. Effect of Cholesterol on Structural and Mechanical Properties of Membranes Depends on Lipid Chain Saturation. *Phys Rev E Stat Nonlin Soft Matter Phys* **2009**, *80* (2), 1–2. https://doi.org/10.1103/PhysRevE.80.021931.

(22) Karal, M. A. S.; Mokta, N. A.; Levadny, V.; Belaya, M.; Ahmed, M.; Ahamed, M. K.; Ahammed, S. Effects of Cholesterol on the Size Distribution and Bending Modulus of Lipid Vesicles. *PLoS One* **2022**, *17* (1), 1–24. https://doi.org/10.1371/journal.pone.0263119.

(23) Chakraborty, S.; Doktorova, M.; Molugu, T. R.; Heberle, F. A.; Scott, H. L.; Dzikovski, B.; Nagao, M.; Stingaciu, L.-R.; Standaert, R. F.; Barrera, F. N.; Katsaras, J.; Khelashvili, G.; Brown, M. F.; Ashkar, R. How Cholesterol Stiffens Unsaturated Lipid Membranes. *Proc. Natl. Acad. Sci. U.S.A.* **2020**, *117* (36), 21896–21905. https://doi.org/10.1073/pnas.2004807117/-/DCSupplemental.

(24) Bai, Y.; Abbott, N. L. Recent Advances in Colloidal and Interfacial Phenomena Involving Liquid Crystals. *Langmuir* **2011**, *27* (10), 5719–5738. https://doi.org/10.1021/la103301d.

(25) Bukusoglu, E.; Pantoja, M. B.; Mushenheim, P. C.; Wang, X.; Abbott, N. L. Design of Responsive and Active (Soft) Materials Using Liquid Crystals. *Annu Rev Chem Biomol Eng* **2016**, *7*, 163–196. https://doi.org/10.1146/annurev-chembioeng-061114-123323.

(26) Özşahin, A. N.; Bukusoglu, E. Responsive Soft Interface Liquid Crystal Microfluidics. *Adv Mater Interfaces* **2024**, *11* (2400334), 1–13. https://doi.org/10.1002/admi.202400334.

(27) İlhan, G.; Carenza, L. N.; Bukusoglu, E. Shear-Induced Structural Transitions in Confined Nematic Soft Interfaces. *Commun Phys* **2025**, *8* (1), 1–15. https://doi.org/10.1038/s42005-025-02058-5.

(28) Lee, G. Y. H.; Lim, C. T. Biomechanics Approaches to Studying Human Diseases. *Trends Biotechnol* **2007**, *25* (3), 111–118. https://doi.org/10.1016/J.TIBTECH.2007.01.005.

(29) Nematbakhsh, Y.; Lim, C. T. Cell Biomechanics and Its Applications in Human Disease Diagnosis. *Acta Mechanica Sinica/Lixue Xuebao* **2015**, *31* (2), 268–273. https://doi.org/10.1007/s10409-015-0412-y.

(30) Schillers, H.; Wälte, M.; Urbanova, K.; Oberleithner, H. Real-Time Monitoring of Cell Elasticity Reveals Oscillating Myosin Activity. *Biophys J* **2010**, *99* (11), 3639–3646. https://doi.org/10.1016/j.bpj.2010.09.048.

(31) Quan, F. S.; Kim, K. S. Medical Applications of the Intrinsic Mechanical Properties of Single Cells. *Acta Biochimica et Biophysica Sinica*. Oxford University Press October 1, 2016, pp 865–871. https://doi.org/10.1093/abbs/gmw081.

(32) Sarna, M.; Zadlo, A.; Hermanowicz, P.; Madeja, Z.; Burda, K.; Sarna, T. Cell Elasticity Is an Important Indicator of the Metastatic Phenotype of Melanoma Cells. *Exp Dermatol* **2014**, *23*, 813–818. https://doi.org/10.1111/exd.12535.

(33) Jerome, B. Surface Effects and Anchoring in Liquid Crystals. *Rep. Prog. Phys* **1991**, *54*, 391–451. https://doi.org/10.1088/0034-4885/54/3/002.

(34) Gupta, J. K.; Meli, M. V.; Teren, S.; Abbott, N. L. Elastic Energy-Driven Phase Separation of Phospholipid Monolayers at the Nematic Liquid-Crystal-Aqueous Interface. *Phys Rev Lett* **2008**, *100* (4), 1–4. https://doi.org/10.1103/PhysRevLett.100.048301.

(35) Brake, J. M.; Daschner, M. K.; Luk, Y. Y.; Abbott, N. L. Biomolecular Interactions at Phospholipid-Decorated Surfaces of Liquid Crystals. *Science (1979)* **2003**, *302* (5653), 2094–2097. https://doi.org/10.1126/science.1091749.

(36) Brake, J. M.; Daschner, M. K.; Abbott, N. L. Formation and Characterization of Phospholipid Monolayers Spontaneously

Assembled at Interfaces between Aqueous Phases and Thermotropic Liquid Crystals. *Langmuir* **2005**, *21* (6), 2218–2228. https://doi.org/10.1021/la0482397.

(37) Kaganer, V. M.; Mö, H.; Dutta, P. Structure and Phase Transitions in Langmuir Monolayers. *Rev Mod Phys* **1999**, *71* (3), 779–819.

(38) Tsuei, M.; Shivrayan, M.; Kim, Y. K.; Thayumanavan, S.; Abbott, N. L. Optical "Blinking" Triggered by Collisions of Single Supramolecular Assemblies of Amphiphilic Molecules with Interfaces of Liquid Crystals. *J Am Chem Soc* **2020**, *142* (13), 6139–6148. https://doi.org/10.1021/jacs.9b13360.

(39) Posnjak, G. Topological Formations in Chiral Nematic Droplets, University of Ljubljana, 2018. https://doi.org/10.1007/978-3-319-98261-8.

(40) Sivakumar, S.; Wark, K. L.; Gupta, J. K.; Abbott, N. L.; Caruso, F. Liquid Crystal Emulsions as the Basis of Biological Sensors for the Optical Detection of Bacteria and Viruses. *Adv Funct Mater* **2009**, *19* (14), 2260–2265. https://doi.org/10.1002/adfm.200900399.

(41) Lin, I. H.; Miller, D. S.; Bertics, P. J.; Murphy, C. J.; De Pablo, J. J.; Abbott, N. L. Endotoxin-Induced Structural Transformations in Liquid Crystalline Droplets. *Science (1979)* **2011**, *332* (6035), 1297–1300. https://doi.org/10.1126/science.1195639.

(42) Miller, D. S.; Wang, X.; Abbott, N. L. Design of Functional Materials Based on Liquid Crystalline Droplets. *Chemistry of Materials* **2014**, *26* (1), 496–506. https://doi.org/10.1021/cm4025028.

(43) Gupta, J. K.; Zimmerman, J. S.; De Pablo, J. J.; Caruso, F.; Abbott, N. L. Characterization of Adsorbate-Induced Ordering Transitions of Liquid Crystals within Monodisperse Droplets. *Langmuir* **2009**, *25* (16), 9016–9024. https://doi.org/10.1021/la900786b.

(44) Carlton, R. J.; Hunter, J. T.; Miller, D. S.; Abbasi, R.; Mushenheim, P. C.; Tan, L. N.; Abbott, N. L. Chemical and Biological Sensing Using Liquid Crystals. *Liq Cryst Rev* **2013**, *1* (1), 29–51. https://doi.org/10.1080/21680396.2013.769310.

(45) Stawarska, A.; Bamburowicz-Klimkowska, M.; Runden-Pran, E.; Dusinska, M.; Cimpan, M. R.; Rios-Mondragon, I.; Grudzinski, I. P. Extracellular Vesicles as Next-Generation Diagnostics and Advanced Therapy Medicinal Products. *International Journal of Molecular Sciences*. Multidisciplinary Digital Publishing Institute (MDPI) June 1, 2024. https://doi.org/10.3390/ijms25126533.

(46) Hanahan, D.; Weinberg, R. A. Hallmarks of Cancer: The Next Generation. *Cell* **2011**, *144* (5), 646–674. https://doi.org/10.1016/J.CELL.2011.02.013.

(47) Skog, J.; Würdinger, T.; van Rijn, S.; Meijer, D. H.; Gainche, L.; Curry, W. T.; Carter, B. S.; Krichevsky, A. M.; Breakefield, X. O. Glioblastoma Microvesicles Transport RNA and Proteins That Promote Tumour Growth and Provide Diagnostic Biomarkers. *Nat Cell Biol* **2008**, *10* (12), 1470–1476. https://doi.org/10.1038/ncb1800.

(48) Peinado, H.; Alečković, M.; Lavotshkin, S.; Matei, I.; Costa-Silva, B.; Moreno-Bueno, G.; Hergueta-Redondo, M.; Williams, C.; García-Santos, G.; Ghajar, C. M.; Nitadori-Hoshino, A.; Hoffman, C.; Badal, K.; Garcia, B. A.; Callahan, M. K.; Yuan, J.; Martins, V. R.; Skog, J.; Kaplan, R. N.; Brady, M. S.; Wolchok, J. D.; Chapman, P. B.; Kang, Y.; Bromberg, J.; Lyden, D. Melanoma Exosomes Educate Bone Marrow Progenitor Cells toward a Pro-Metastatic Phenotype through MET. *Nat Med* **2012**, *18* (6), 883–891. https://doi.org/10.1038/nm.2753.

(49) Xu, R.; Rai, A.; Chen, M.; Suwakulsiri, W.; Greening, D. W.; Simpson, R. J. Extracellular Vesicles in Cancer — Implications for Future Improvements in Cancer Care. *Nat Rev Clin Oncol* **2018**, *15* (10), 617–638. https://doi.org/10.1038/s41571-018-0036-9.

(50) Zhou, S.; Hu, T.; Han, G.; Wu, Y.; Hua, X.; Su, J.; Jin, W.; Mou, Y.; Mou, X.; Li, Q.; Liu, S. Accurate Cancer Diagnosis and Stage Monitoring Enabled by Comprehensive Profiling of Different Types of Exosomal Biomarkers: Surface Proteins and MiRNAs. *Small* **2020**, *16* (48). https://doi.org/10.1002/smll.202004492.

(51) Ali Moussa, H. Y.; Manaph, N.; Ali, G.; Maacha, S.; Shin, K. C.; Ltaief, S. M.; Gupta, V.; Tong, Y.; Ponraj, J.; Salloum-Asfar, S.; Mansour, S.; Al-Shaban, F. A.; Kim, H. G.; Stanton, L. W.; Grivel, J. C.; Abdulla, S. A.; Al-Shammari, A. R.; Park, Y. Single Extracellular Vesicle Analysis Using Flow Cytometry for Neurological Disorder Biomarkers. *Front Integr Neurosci* **2022**, *16*. https://doi.org/10.3389/fnint.2022.879832.

(52) Ortega-Sanchez, F. G.; Teresa, V.; Widmann, T.; Regiart, M.; Jerez-Salcedo, M. T.; Fernández-Baldo, M. A.; de Miguel-Perez, D. Microfluidic Systems in Extracellular Vesicles Single Analysis. A Systematic Review. *TrAC Trends in Analytical Chemistry* **2023**, *159*, 116920. https://doi.org/10.1016/J.TRAC.2023.116920.

(53) Pantaler, E.; Kamp, D.; Haest, C. W. M. Acceleration of Phospholipid Flip-Flop in the Erythrocyte Membrane by Detergents Differing in Polar Head Group and Alkyl Chain Length. *Biochim Biophys Acta Biomembr* **2000**, *1509* (1–2), 397–408. https://doi.org/10.1016/S0005-2736(00)00322-9.

(54) Jing, H.; Wang, Y.; Desai, P. R.; Ramamurthi, K. S.; Das, S. Lipid Flip-Flop and Desorption from Supported Lipid Bilayers Is Independent of

Curvature. *PLoS One* **2020**, *15* (12). https://doi.org/10.1371/journal.pone.0244460.

(55) Alonso, A.; Gõ Ni, F. M. The Physical Properties of Ceramides in Membranes. *Annu Rev Biophys* **2024**, *176*, 633–654. https://doi.org/10.1146/annurev-biophys.

(56) Castro, B. M.; Prieto, M.; Silva, L. C. Ceramide: A Simple Sphingolipid with Unique Biophysical Properties. *Progress in Lipid Research*. April 2014, pp 53–67. https://doi.org/10.1016/j.plipres.2014.01.004.

(57) Espinosa, G.; López-Montero, I.; Monroy, F.; Langevin, D. Shear Rheology of Lipid Monolayers and Insights on Membrane Fluidity. *Proc. Natl. Acad. Sci. U.S.A.* **2011**, *108* (15), 6008–6013. https://doi.org/https://doi.org/10.1073/pnas.1018572108.

(58) Luo, J.; Yang, H.; Song, B. L. Mechanisms and Regulation of Cholesterol Homeostasis. *Nat Rev Mol Cell Biol* **2020**, *21* (4), 225–245. https://doi.org/10.1038/s41580-019-0190-7.

(59) Volobueva, A.; Zhang, D.; Grechko, A. V.; Orekhov, A. N. Foam Cell Formation and Cholesterol Trafficking and Metabolism Disturbances in Atherosclerosis. *Cor Vasa* **2019**, *61* (1), 48–54. https://doi.org/10.1016/j.crvasa.2018.06.006.

(60) Hao, M.; Head, W. S.; Gunawardana, S. C.; Hasty, A. H.; Piston, D. W. Direct Effect of Cholesterol on Insulin Secretion: A Novel Mechanism for Pancreatic β-Cell Dysfunction. *Diabetes* **2007**, *56* (9), 2328–2338. https://doi.org/10.2337/db07-0056.

(61) Kaddah, S.; Khreich, N.; Kaddah, F.; Charcosset, C.; Greige-Gerges, H. Cholesterol Modulates the Liposome Membrane Fluidity and Permeability for a Hydrophilic Molecule. *Food and Chemical*

Toxicology **2018**, *113*, 40–48. https://doi.org/10.1016/j.fct.2018.01.017.

(62) Canham, P. B. The Minimum Energy of Bending as a Possible Explanation of the Biconcave Shape of the Human Red Blood Cell. *J Theor Biol* **1970**, *26* (1), 61–81. https://doi.org/10.1016/S0022-5193(70)80032-7.

(63) Karal, M. A. S.; Billah, M. M.; Ahmed, M.; Ahamed, M. K. A Review on the Measurement of the Bending Rigidity of Lipid Membranes. *Soft Matter* **2023**, *19* (43), 8285–8304. https://doi.org/10.1039/d3sm00882g.

(64) Milner, S. T.; Safran, S. A. Dynamical Fluctuations of Droplet Microemulsions and Vesicles. *Phys Rev A (Coll Park)* **1987**, *36* (9). https://doi.org/10.1103/PhysRevA.36.4371.

(65) Evans, E.; Rawicz, W. Entropy-Driven Tension and Bending Elasticity in Condensed-Fluid Membranes. *Phys Rev Lett* **1990**, *64* (17), 2094–2099. https://doi.org/10.1103/PhysRevLett.64.2094.

(66) Pöhnl, M.; Trollmann, M. F. W.; Böckmann, R. A. Nonuniversal Impact of Cholesterol on Membranes Mobility, Curvature Sensing and Elasticity. *Nat Commun* **2023**, *14* (1), 1–12. https://doi.org/10.1038/s41467-023-43892-x.

(67) Beyazkilic, P.; Akcimen, S.; Elbuken, C.; Ortaç, B.; Cai, S.; Bukusoglu, E. Contactless Pulsed and Continuous Microdroplet Release Using Photothermal Liquid Crystals. *Adv Funct Mater* **2022**, *32* (44), 1–29. https://doi.org/10.1002/adfm.202205385.

(68) Maiti, S.; Roh, S.; Cohen, I.; Abbott, N. L. Non-Equilibrium Ordering of Liquid Crystalline (LC) Films Driven by External Gradients in Surfactant Concentration. *J Colloid Interface Sci* **2023**, *637*, 134–146. https://doi.org/10.1016/j.jcis.2022.12.124.

(69) Lavrentovich, O. D.; Zola, E. Fluorescence Confocal Polarizing Microscopy: Three-Dimensional Imaging of the Director. *PRAMANA Indian Academy of Sciences* **2003**, *61* (2), 373–384.

(70) Smalyukh, I. I.; Shiyanovskii, S. V.; Lavrentovich, O. D. Three-Dimensional Imaging of Orientational Order by Fluorescence Confocal Polarizing Microscopy. *Chem Phys Lett* **2001**, *336* (1–2), 88–96. https://doi.org/10.1016/S0009-2614(00)01471-8.

(71) Bernard, A. L.; Guedeau-Boudeville, M. A.; Marchi-Artzner, V.; Gulik-Krzywicki, T.; Di Meglio, J. M.; Jullien, L. Shear-Induced Permeation and Fusion of Lipid Vesicles. *J Colloid Interface Sci* **2005**, *287* (1), 298–306. https://doi.org/10.1016/j.jcis.2004.12.019.

(72) Doktorova, M.; Harries, D.; Khelashvili, G. Determination of Bending Rigidity and Tilt Modulus of Lipid Membranes from Real-Space Fluctuation Analysis of Molecular Dynamics Simulations. *Physical Chemistry Chemical Physics* **2017**, *19* (25), 16806–16818. https://doi.org/10.1039/c7cp01921a.

(73) Arunachalam, B.; Jaganathan, M.; Palanisamy, T.; Dhathathreyan, A. Physico-Chemical Studies of Elastic Compliance and Adsorption of DOPC Vesicles and Its Mixture with Charged Lipids at Fluid/Solid Interface. *Colloids Surf B Biointerfaces* **2021**, *199*, 1–9. https://doi.org/10.1016/j.colsurfb.2020.111544.

(74) Pinazo, A.; Wen, X.; Liao, Y. C.; Prosser, A. J.; Franses, E. I. Comparison of DLPC and DPPC in Controlling the Dynamic Adsorption and Surface Tension of Their Aqueous Dispersions. *Langmuir* **2002**, *18* (23), 8888–8896. https://doi.org/10.1021/la020476r.

(75) Jiménez-Rojo, N.; García-Arribas, A. B.; Sot, J.; Alonso, A.; Goñi, F. M. Lipid Bilayers Containing Sphingomyelins and Ceramides of

Varying N-Acyl Lengths: A Glimpse into Sphingolipid Complexity. *Biochim Biophys Acta Biomembr* **2014**, *1838* (1 PARTB), 456–464. https://doi.org/10.1016/j.bbamem.2013.10.010.

(76) Choi, S. Q.; Steltenkamp, S.; Zasadzinski, J. A.; Squires, T. M. Active Microrheology and Simultaneous Visualization of Sheared Phospholipid Monolayers. *Nat Commun* **2011**, *2* (1), 1–6. https://doi.org/10.1038/ncomms1321.

(77) Et-Thakafy, O.; Delorme, N.; Guyomarc'h, F.; Lopez, C. Mechanical Properties of Milk Sphingomyelin Bilayer Membranes in the Gel Phase: Effects of Naturally Complex Heterogeneity, Saturation and Acyl Chain Length Investigated on Liposomes Using AFM. *Chem Phys Lipids* **2018**, *210*, 47–59. https://doi.org/10.1016/J.CHEMPHYSLIP.2017.11.014.

(78) Kessel, A.; Ben-Tal, N.; May, S. Interactions of Cholesterol with Lipid Bilayers: The Preferred Configuration and Fluctuations. *Biophys J* **2001**, *81* (2), 643–658. https://doi.org/10.1016/S0006-3495(01)75729-3.

(79) Dimova, R. Recent Developments in the Field of Bending Rigidity Measurements on Membranes. *Adv Colloid Interface Sci* **2014**, *208*, 225–234. https://doi.org/10.1016/j.cis.2014.03.003.

(80) Henriksen, J.; Rowat, A. C.; Brief, E.; Hsueh, Y. W.; Thewalt, J. L.; Zuckermann, M. J.; Ipsen, J. H. Universal Behavior of Membranes with Sterols. *Biophys J* **2006**, *90* (5), 1639–1649. https://doi.org/10.1529/biophysj.105.067652.

(81) Huang, J.; Feigenson, G. W. A Microscopic Interaction Model of Maximum Solubility of Cholesterol in Lipid Bilayers. *Biophys J* **1999**, *76* (4), 2142–2157. https://doi.org/10.1016/S0006-3495(99)77369-8.

(82) Dai, J.; Alwarawrah, M.; Huang, J. Instability of Cholesterol Clusters in Lipid Bilayers and the Cholesterol's Umbrella Effect. *Journal of Physical Chemistry B* **2010**, *114* (2), 840–848. https://doi.org/10.1021/jp909061h.

(83) Sabatini, K.; Mattila, J. P.; Kinnunen, P. K. J. Interfacial Behavior of Cholesterol, Ergosterol, and Lanosterol in Mixtures with DPPC and DMPC. *Biophys J* **2008**, *95* (5), 2340–2355. https://doi.org/10.1529/biophysj.108.132076.

(84) Stottrup, B. L.; Keller, S. L. Phase Behavior of Lipid Monolayers Containing DPPC and Cholesterol Analogs. *Biophys J* **2006**, *90* (9), 3176–3183. https://doi.org/10.1529/biophysj.105.072959.

(85) Discher, B. M.; Won, Y. Y.; Ege, D. S.; Lee, J. C. M.; Bates, F. S.; Discher, D. E.; Hammer, D. A. Polymersomes: Tough Vesicles Made from Diblock Copolymers. *Science (1979)* **1999**, *284* (5417), 1143–1146. https://doi.org/10.1126/science.284.5417.1143.

(86) Stylianopoulos, T.; Jain, R. K. Combining Two Strategies to Improve Perfusion and Drug Delivery in Solid Tumors. *Proc Natl Acad Sci U S A* **2013**, *110* (46), 18632–18637. https://doi.org/10.1073/pnas.1318415110.

(87) Liu, Y.; Shen, L. From Langmuir Kinetics to First- and Second-Order Rate Equations for Adsorption. *Langmuir* **2008**, *24* (20), 11625–11630. https://doi.org/10.1021/la801839b.

(88) Okiishi, M.; Rothmayer, H.; Huebsch, W.; Rothmsyer, A. P. *Fluid Mechanics*, 7th ed.; John Wiley & Son, 2013.

(89) Bruus, H. *Theoretical Microfluidics*, 3rd ed.; New York: Oxford University Press, 2006.

APPENDICES

A. COMSOL Simulation

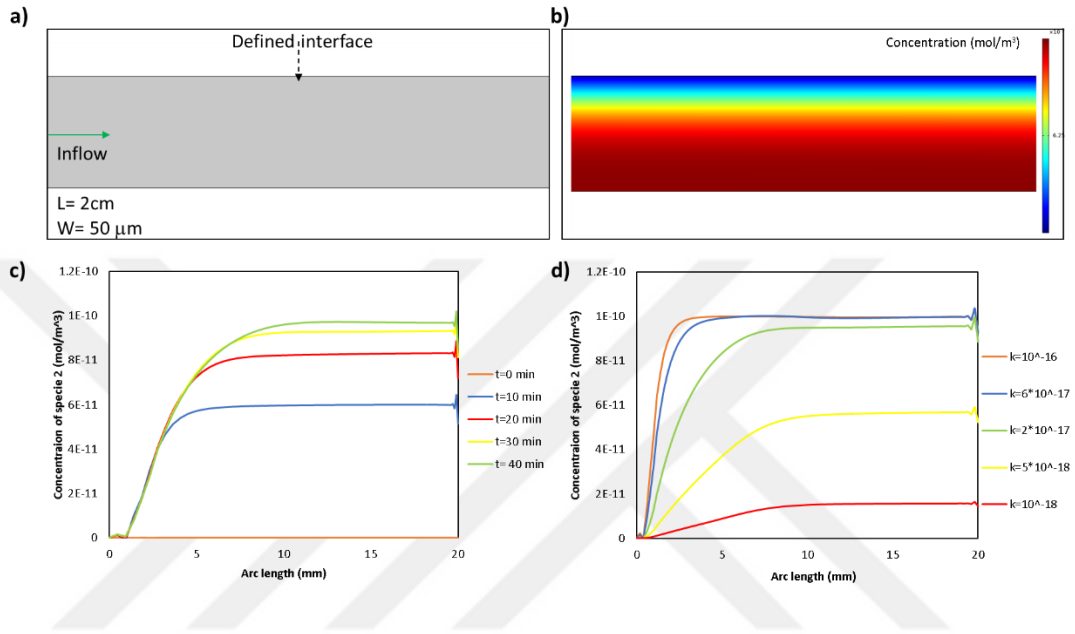

Figure A.1.COMSOL simulation. (a) Geometry defined in COMSOL represents the water side of the experimental microfluidic design, (b) the concentration profile of species 1, which defines the lipid vesicles in the bulk, (c) concentration distribution of species 2, which defines the single lipid molecules along the interface length with respect to time, (d) concentration distribution of species 2, which defines the single lipid molecules along the interface length with respect to different surface reaction constants.

By using COMSOL Multiphysics, we defined a rectangular geometry with dimensions of 50 µm width and 2 cm length to represent the aqueous side of our microfluidic channels (**Fig.A.1a**). We defined the creeping flow module with a no-slip wall for the hard interface and a slip wall with 0.8 µm/s velocity for the interface. Also, for the inlet velocity, we defined 135 µm/s from our experiments. By using the transport of diluted species module of COMSOL and defining the adsorption, we

used a surface reaction model with two species, where the first species is consumed and represents lipid vesicles in the bulk, and the second species forms in the reaction model, representing the single lipids at the interface. Also, we limited the surface reaction with the Langmuir model.[87]

$$J_{c1} = (-k * c_1 * \left(1 - \frac{c_2}{c_{2,max}}\right)) \qquad (5)$$

$$J_{c2} = \left(80000 * k * c_1 * \left(1 - \frac{c_2}{c_{2,max}}\right)\right) - k_2 * c_2 \qquad (6)$$

Where J_{c1} and J_{c2} represent the mol flux of the first species and the second species, respectively. k and k_2 define the surface reaction rate constants. c_1 and c_2 represent the concentration of lipids in the bulk and at the interface, respectively, while $c_{2,max}$ was defined as the maximum concentration at the interface to correlate the monolayer coverage. In equation 2, the right-hand side terms define the desorption of the lipids from the interface, and desorption is represented by k_2. However, phospholipid adsorption into the interface is irreversible. Therefore, we defined k_2 as very small to avoid the desorption. Moreover, multiplying equation 2 by 80000 represents the single lipid number in a vesicle, since lipids are in vesicles at the bulk; however, after adsorption, they are located at the interface as single molecules, and it was calculated by considering the area per lipid is 0.5 $\frac{nm^2}{molecule}$ and radius of a vesicle is approximately 40 nm and assuming the bilayer thickness is negligible.

$$2 * (4 * \pi * (40\ nm)^2) = 40212.4\ nm^2$$

$$40.212.4\ nm^2 * \frac{1}{\frac{0.5\ nm^2}{lipid}} \simeq 80000\ lipid$$

The concentration profile of the first species through the channel (**Fig.A.1b**) shows that c_1 decreases through the y direction or interface since surface reaction occurs at the interface, and c1 was defined as being consumed in this reaction. Also, c_1 concentration decreases gradually through the end of the channel, a region where c_2 increases. Concentration profile of the second species, lipids at the interface,

analyzed with respect to time and arc length, which is a cut line at the interface (**Fig.A.1c**). The Profile showed that c_2 increases with increasing arc length; this trend was consistent with the phospholipid domain accumulation at the end of the channel in our experiments. To relate change in the rigidity of the vesicles, we changed the surface reaction constants in the simulation. We found that monolayer coverage cannot be reached with small k's, meaning vesicles were not able to adsorb into the interface. With increasing k values, monolayer coverage was reached faster, and single lipids located at the small arc lengths, representing adsorption, occurred at the longer region of the interface with increasing k values (**Fig.A.1d**). This trend can be correlated with the soft vesicles, such as mixed micelles with DTAB or egg SM with cholesterol, and stiff vesicles, such as DLPC with C16-ceramide or pure Egg SM, as kinetic in our experiments. High k values adsorption kinetics represent the soft vesicles, while small k's represent the stiff vesicles' adsorption kinetics. Although the concentration profile of c_2 with time and arc length was not exactly the same as our experiments since we did not define 5CB, and therefore nematic elasticity, the simulation gave insights about the adsorption kinetics and monitoring the rigidity effect.

B. Shear Rate Calculations for Droplet Systems

To find the angular velocity of the vortex[88]

$$\omega = \frac{2\pi * \mathrm{RPM}}{60}$$

where ω is the angular velocity

$$\omega = \frac{2\pi * 3000}{60} = 314.2\, rad/s$$

To find the shear that applied the solution in 4 mL (d=1.2 cm),

$$\dot{\gamma} = \frac{\omega * R}{d}$$

$$\dot{\gamma} = \frac{314.2\ * 0.006}{0.001} \approx 1900\ s^{-1}$$

C. Shear Stress and Shear Rate Calculations for Microfluidic Channels

Experimental values of water velocity were obtained via particle tracking in the channel, and data were averaged.

We calculated the volumetric flow rate using,

$$\dot{Q} = v * A \qquad (1)$$

where $\dot{Q}$ is volumetric flow rate (m^3/s), v is average experimental velocity (m/s), and A is the cross-sectional area of the water flow side of the channel. The channel dimensions were such that h is the depth of the channel, 14 μm, and w is the width of the aqueous phase, 250 μm.

Maximum shear stress at the wall (parallel-plate approximation)[89];

$$\tau_w \simeq \frac{h}{2} * \frac{\Delta P_{flow}}{L} \qquad (2)$$

$$\tau_w = \frac{14 * 10^{-6} m}{2} * \frac{500\ Pa}{0.025\ m} = 0.14\ Pa$$

where τ_w is the maximum shear stress at the wall, ΔP_{flow} is the pressure drop through the channel, and L is the length of the channel. ΔP_{flow} assumed as a set pressure since the end of the channel is open to the atmosphere.

Using Newton's law of viscosity,

$$\tau_w = \mu * \dot{\gamma} \qquad (3)$$

where μ is the viscosity of the PBS at room temperature and $\dot{\gamma}$ is shear rate, we calculate the shear rate in the microfluidic channels. The calculation results are shown in Table 4 for four different flow rates measured.

Table 4. The calculated values for shear stress and shear rate of the aqueous phase at given inlet pressures to the channels.

	5 mbar	7.5 mbar	25 mbar	30 mbar
Water velocity (m/s)	$1.35*10^{-4}$	$2.62*10^{-4}$	$6.72*10^{-4}$	$7.89*10^{-4}$
Flowrate (m^3/s)	$4.73*10^{-13}$	$9.17*10^{-13}$	$2.35*10^{-13}$	$2.72*10^{-13}$
Shear stress (Pa)	0.14	0.21	0.70	0.84
Shear rate (s^{-1})	158	237	787	948

D. Supporting Figures

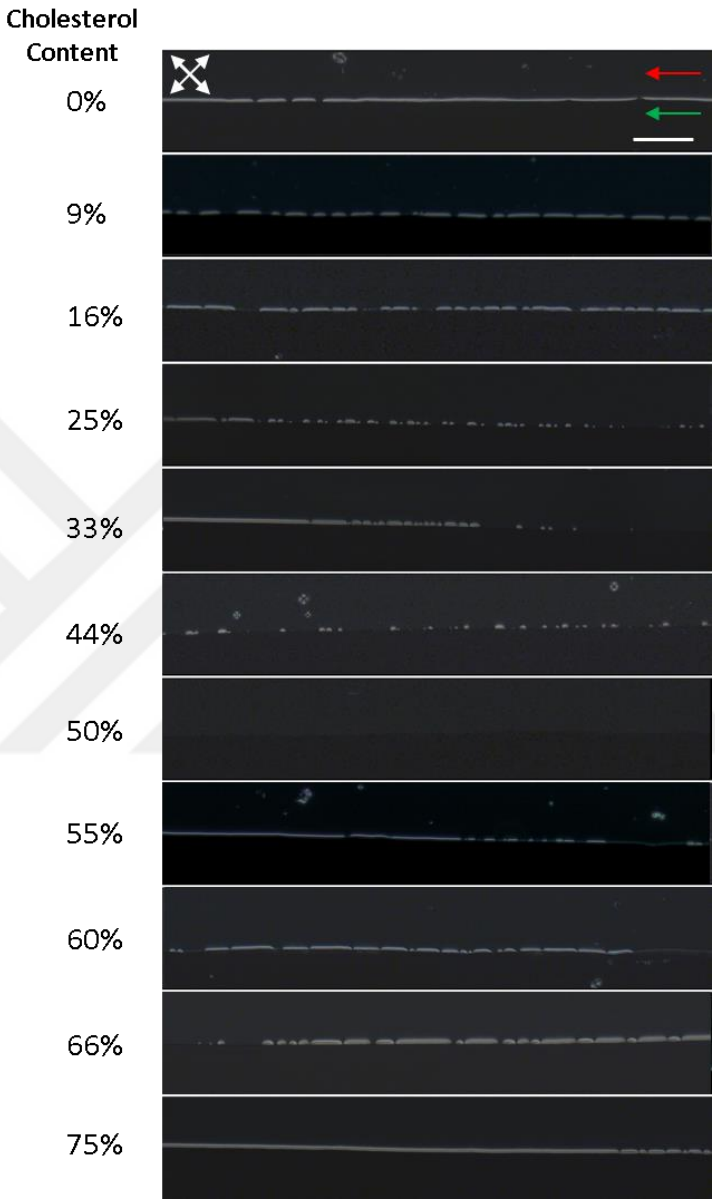

Figure D.1. Representative images of fractional coverage of DLPC-cholesterol complex. Polarized optical micrographs collected from experiments with contacting 5CB with a constant 0.5 μM DLPC concentration and varying content of cholesterol from 0% to 75%, as indicated in the near of images. Images were collected at location

4 and t=40 min. The white double-sided arrow shows the orientations of the analyzer and polarizers used in all of the images shown in the figure. Scale bar: 100 μm.

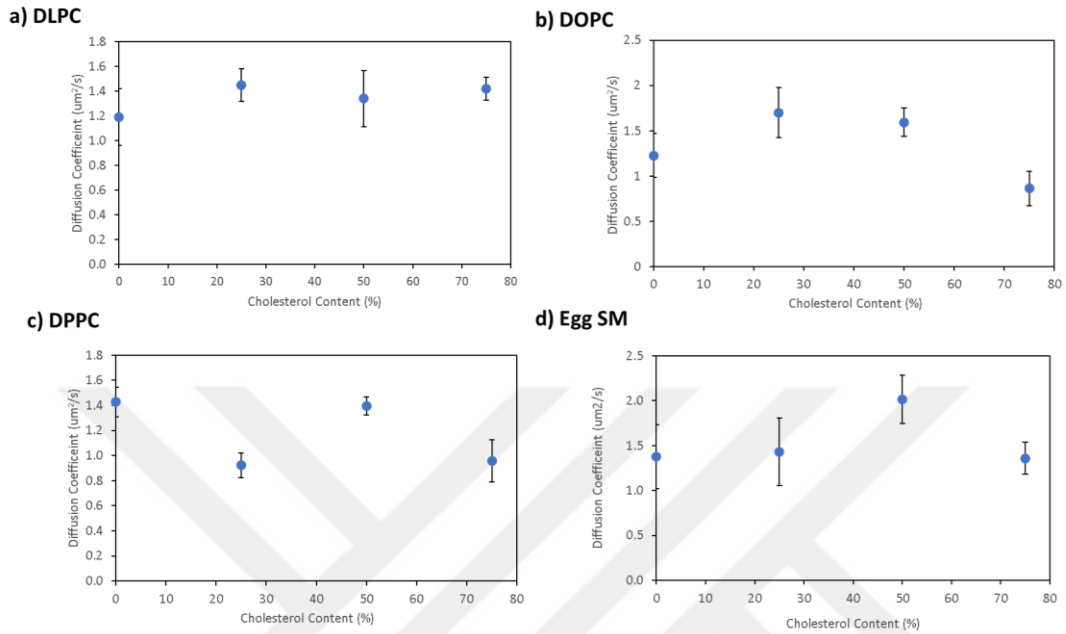

Figure D.2.Diffusion coefficients of lipids. The plots of diffusion coefficients of the vesicles formed by (a) DLPC, (b) DOPC, (c) DPPC, (d) Egg SM with cholesterol sketched vs. cholesterol content (%).

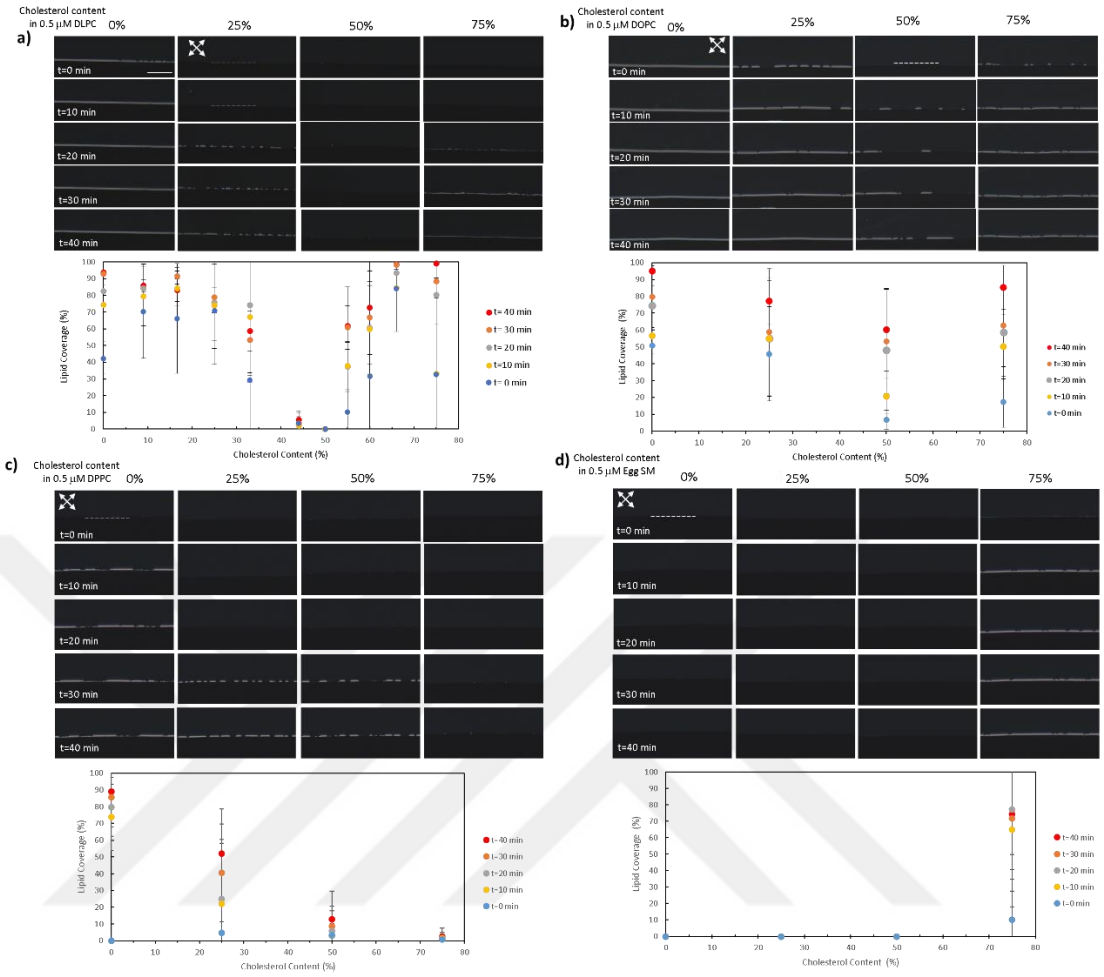

Figure D.3.Polarized optical micrographs and lipid coverage plots for all lipids. Polarized optical micrographs collected from experiments with contacting 5CB with a constant 0.5 µM (a) DLPC, (b) DOPC, (c) DPPC, (d) Egg SM, and varying content of cholesterol from 0% to 75%, as indicated in the top titles. Each line of images was collected at the duration after aqueous phase flow was initiated, as indicated in the images. All images were collected at t = 40 min. The white double-sided arrow shows the orientations of the analyzer and polarizers used in all of the images shown in the figure. The dashed lines in the images indicate the location of the horizontal soft interfaces. The plots of lipid coverage (%) vs cholesterol content (%) for each lipid were given under the micrographs.